Novel Materials, Computational Spectroscopy, and Multiscale Simulation in Nanoscale Photovoltaics

by

Marco Bernardi

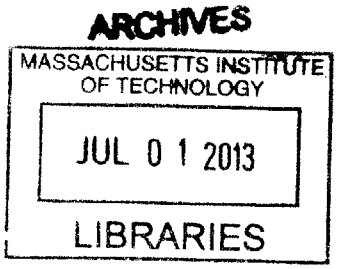

Submitted to the Department of Materials Science and Engineering
in partial fulfillment of the requirements for the degree of

DOCTOR OF PHILOSOPHY IN MATERIALS SCIENCE AND ENGINEERING

AT THE

MASSACHUSETTS INSTITUTE OF TECHNOLOGY

June 2013

Signature of Author: _____

Department of Materials Science and Engineering
May 1, 2012

Certified by: _____

Jeffrey C. Grossman
Carl Richard Soderberg Associate Professor of Power Engineering
Thesis Supervisor

Accepted by: _____

Gerbrand Ceder
R. P. Simmons Professor of Materials Science and Engineering
Chair, Departmental Committee on Graduate Students

Novel Materials, Computational Spectroscopy, and Multiscale Simulation in Nanoscale Photovoltaics

by

Marco Bernardi

Submitted to the Department of Materials Science and Engineering
on May 1, 2013 in partial fulfillment of the requirements for the degree of
Doctor of Philosophy in Materials Science and Engineering

Abstract

Photovoltaic (PV) solar cells convert solar energy to electricity using combinations of semiconducting sunlight absorbers and metallic materials as electrical contacts. Novel nanoscale materials introduce new paradigms for ultrathin, lightweight, solution processable PV as an alternative to conventional Si technology. For example, the ability to use deposition methods not viable in conventional inorganic PV is particularly exciting as products like paper, textiles, automobiles, and building materials could be coated with PV devices, thus making solar cells ubiquitous. In addition, the optical absorption, band gap, and charge carrier mobility of nanoscale materials can be tuned by tailoring their chemistry or using quantum confinement effects, thus creating novel opportunities for efficient and inexpensive solar cells. From the viewpoint of the fundamental processes involved in PV operation, nanoscale PV poses additional challenges due to the formation of strongly bound electron-hole pairs (excitons) upon photoabsorption requiring the presence of semiconductor heterointerfaces within the active layer to dissociate excitons and generate charge carriers. Such interfaces are known as donor-acceptor (D-A) interfaces, and their presence leads to correlated exciton and charge dynamics in nanoscale PV. Material combinations suitable for nanoscale PV can be predicted using atomistic quantum mechanical calculations, which further enable the computation of a small number of spectroscopic quantities necessary to estimate the power conversion efficiency.

Our work shows the computational design of two novel classes of materials for nanoscale PV displaying optical absorption, stability, tunability, and carrier mobility superior to materials employed so far in nanoscale PV. To this end, we employed simulation techniques generally falling under the umbrella of *ab initio* atomistic electronic structure methods, including density functional theory (DFT) and the GW-Bethe-Salpeter approach. Proof-of-concept PV devices were fabricated and tested within our group and in collaboration with other experimental research groups. The two material families studied in this thesis include carbon based materials (both in nanoscale and bulk form) and two-dimensional monolayers such as graphene, reduced graphene oxide, boron nitride, and transition metal dichalcogenides. Our work demonstrates

the feasibility of novel PV devices with a range of benefits employing such materials. It further develops a framework to accurately predict exciton dissociation at D-A interfaces and estimate efficiencies in nanoscale PV.

Beyond our work on nanoscale materials, we introduce a combination of methods to enable simulation of nanoscale PV across time and length scales. We discuss modeling of subpicosecond dynamics at D-A interfaces, device-scale transport of excitons, charge carriers, and photons, and macroscopic sunlight management by arranging solar panels to best couple with the Sun's trajectory. We elaborate on the latter point and discuss our work on simulation and fabrication of macroscopic three-dimensional PV structures with promise to deliver a range of benefits for solar energy conversion, including reduced seasonal and latitude sensitivity and a doubling of peak power generation hours. Taken together, this thesis advances the computational design of nanoscale PV systems and introduces novel families of materials and PV structures with technological promise for next-generation PV.

This thesis document is organized as follows: Chapter 1 and Chapter 2 introduce, respectively, nanoscale PV and *ab initio* atomistic simulation methods employed in this work. Chapter 3 is the core of our work on novel families of materials for nanoscale PV, and Chapter 4 illustrates multi-scale simulation methods in nanoscale PV as well as our work on three-dimensional PV. The key results are briefly summarized in Chapter 5.

Acknowledgements

I am highly indebted to a large number of people for making my adventure as a graduate student at MIT a most exhilarating one. The five years spent on classwork and focused research have been a time of unmatched personal and professional growth. The world-class environment at MIT imposes the highest standards of dedication, while the diversity fosters mutual understanding and the development of unique interpersonal skills. I was lucky enough to be born in Italy, a land where friendship is profound and long-lasting; the unconditional love of my family and friends has helped me during the toughest days in the last five years: yes, a Ph.D. from MIT does not come without hurdles! First and foremost, I'm thankful to my wife Rosa for blessing me with her presence and support throughout my Ph.D., and for joining me in this adventure to the U.S.A.

On a sunny day in August of 2009, I met my Ph.D. advisor Prof. Jeffrey C. Grossman, in the form of a young and bright man coming from California to pursue excellence at all levels at MIT. Our common goal to excel at the cost of personal sacrifice, and our shared view of honesty and ethics in life and research, has allowed us to skillfully navigate the perilous seas of scientific research. Along the journey we shared fun and frustration, success and criticism, excitement and boredom. I am highly indebted to him for always behaving with friendship and transparency, which has led to establish mutual trust and a unique collaborative spirit. I am thankful to him for guiding me in my research and patiently listening to my ideas, no matter how unfeasible they were, and for selecting the most reasonable ones (as well as suggesting his own) to implement our research. Our work has been accompanied by many moments of genuine fun, facilitated by the possibility to role-play my character of the humble Ph.D. student and his character of the acclaimed scientific world leader... :−) I wish Jeff all the best in his personal and professional life, and that his every wish may come true. And I'm also looking forward to do much more science with him!

Through large efforts, my advisor has managed to put together a group of over 20 highly dedicated researchers, each with a diverse background and expertise. Many faces have changed since I started my work in the Grossman Group (G^2), and I have hugely benefitted from interacting with all of my lab mates. Out of the "founders " of the G^2 − those arrived on September 1 of 2009 on a yellow truck from California − I want to thank Elif Ertekin, Alex Greaney, Lucas Wagner, Rajamani Ragunathan, and Joo-Hyoung Lee for teaching me so much about computer simulations in such a short time. I further wish to thank my Italian colleagues and friends Giuseppe Romano and Nicola Ferralis for endless discussions where science always got mixed with topics such as politics, life, women, Italy, America, etc... I also thank my former housemates and colleagues Stefano Passerini and Rodolfo Camacho-Aguilera for sharing discussions on similar topics. I enjoyed interacting with many other G^2 members, including (in no particular order) Engin Durgun, Priyank Kumar, Brent Keller, Eric Johlin, David Cohen-Tanugi, David Strubbe, Can Ataca, Francesca Risplendi, Michelle Tomasik, Alexie Kolpak, Donghun

Kim, Sophia R. Sklan, and Jin H. Wan, and in fact all of the G^2 members.

Many collaborators have contributed to my professional growth, including Maurizia Palummo, Shenqiang Ren, Michele Giulianini, and Silvija Gradecak; I am thankful to all of them for working with me at some point of my Ph.D. My knowledge of materials science, energy science, and condensed matter physics has been shaped by many classes taken at MIT, taught by some of the most brilliant teachers one could ever wish to meet. While they are too many to list, I greatly value their contribution to my knowledge and their patience in answering my questions. Finally, I am indebted to the Department of Materials Science at MIT for admitting me into their fantastic Ph.D. program, thus giving me the chance of my life to make a dent (however small) in science, as well as my thesis committee composed by Prof. Gerbrand Ceder, Prof. Alfredo Alexander-Katz, and Prof. Silvija Gradecak for considering my work and spending some of their valuable time to read this thesis. I feel blessed for having been part of MIT, indeed one of the most active scientific communities in the world combining scientific thinking with technological innovation.

Table of Contents

1 Nanoscale Photovoltaics

1.1 Introduction

Motivated by the availability of a large amount of incident solar energy and pressed by the need to meet the ever-rising global energy demand while facing rapid worldwide population growth, technologies capable of converting solar energy to heat and electricity remain at the center of technological innovation and scientific research. Among these, solar cells have reached a great level of sophistication and aim at providing a significant fraction of the total renewable energy in the immediate future (Figure 1.1). Photovoltaic (PV) solar cells convert solar energy to electricity using combinations of semiconducting sunlight absorbers and metallic materials as electrical contacts. Monocrystalline and poly-crystalline Si are the mainstream materials and technologies in the current PV market, largely due to 1) well-established manufacturing cycles borrowed from the microelectronic industry, 2) appealing power conversion efficiencies of up to 25 % in the lab and 20 % in the module, and 3) Silicon's availability and Earth abundance. It is thought that if silver contacts can be replaced with more Earth-abundant materials[1], Si based PV has the potential to reach Terawatt scale installed capacity (Figure 1.1), *versus* a current global installed PV capacity of ~100 GW at the end of 2012[2,3,4].

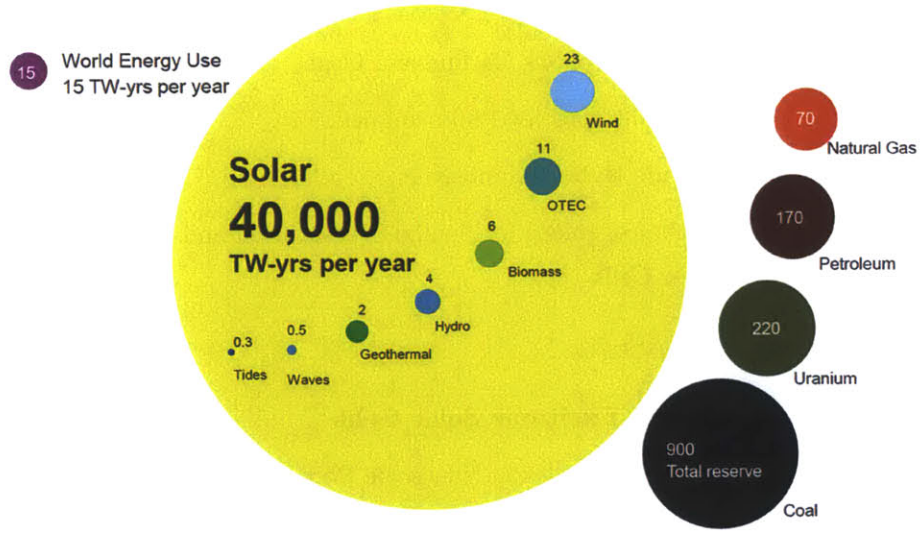

Figure 1.1: **Solar energy.** Comparison of the potential for yearly energy generation of solar against other renewable and fossil resources. Also shown is the world energy use of 15 TW-yrs/yr. It is clear that the magnitude of the solar resource dwarfs any other fossil and renewable resources. (Source: Richard Perez, MIT).

While PV may seem to be a solved problem due to the presence of a key working technology like Si, this scenario is far from true. Due to its indirect band gap of 1.1 eV, Si is a poor absorber at visible photon energies, and solar cells thicker than 100 μm are necessary to ensure effective sunlight harvesting. For comparison, direct gap materials with near-ideal gaps for sunlight absorption of 1.3−1.5 eV can effectively capture a large fraction of sunlight with active layers as thin as 300 nm−1 μm and hence afford considerable material savings. In addition, fabricating and doping Si wafers requires high temperatures, specialized plants and labor, and is a highly energy intensive process. This combination leads to significant material costs for high-purity (electronic-grade) Si necessary for use in solar cells, and energy payback times of 2−3 years. Current costs of installed residential Si panels are around 2−2.5 \$, of which ∼1 \$ is due to material cost, and the remaining fraction (usually over 50 % of the total) to balance-of-system (BOS) installation costs[4] including labor employed to install the panels as well as the inverter and other electrical components. BOS costs have followed a much slower learning curve than material costs, thus contributing to increasing fractions of the total PV system outlay.

In the last decade, several PV technologies alternative to crystalline Si have been developed using inorganic materials with high optical absorption and thin film (∼1 μm thick) active layers, such as amorphous Si, GaAs, CdTe, and CIGS. Each of these technologies involves different challenges toward cost reduction and large scale deployment (see ref.[2] for further details). In this thesis, we shall be mostly concerned with another broad class of solid state solar cells alternative to Si, which we refer to as *nanoscale solar cells* due to the presence of functional materials with nanometer size in the active layer. The first class of nanoscale solar cells appeared in the literature are the so-called organic solar cells, a device family with a current record efficiency slightly above 10 %[5,6]. Organic solar cells are based on conjugated polymers and small molecules, and require a nanoscale component (*e.g.* a C_{60} fullerene) to accomplish PV operation effectively, as well as nm to μm sized domains in the materials composing the active layer[7,8]. More recently, colloidal nanocrystals such as PbS and CdTe – commonly referred to as quantum dots (QD) – have emerged as an important family of PV materials, achieving record efficiencies of 7 % in ∼100 nm thick active layers[9]. Beyond the excitement and scientific curiosity of applying nanoscale materials to solar energy conversion, the practical motivation behind researching and developing solar cells containing nanomaterials is at least two-fold:

1. Nanoscale materials can be processed from solution or chemical vapor deposition in thin film form on a large range of substrates. As such, they entail the possibility of using lightweight flexible substrates combined with printable or sprayable inks for low temperature and ambient pressure continuous active layer fabrication, with the potential to dramatically reduce material and BOS costs. The ability to use alternative deposition methods not viable in conventional inorganic PV materials is particularly exciting since products like paper, textiles, automobiles, and building materials could be coated with PV devices, thus making solar cells ultrathin, lightweight, and ubiquitous[10].

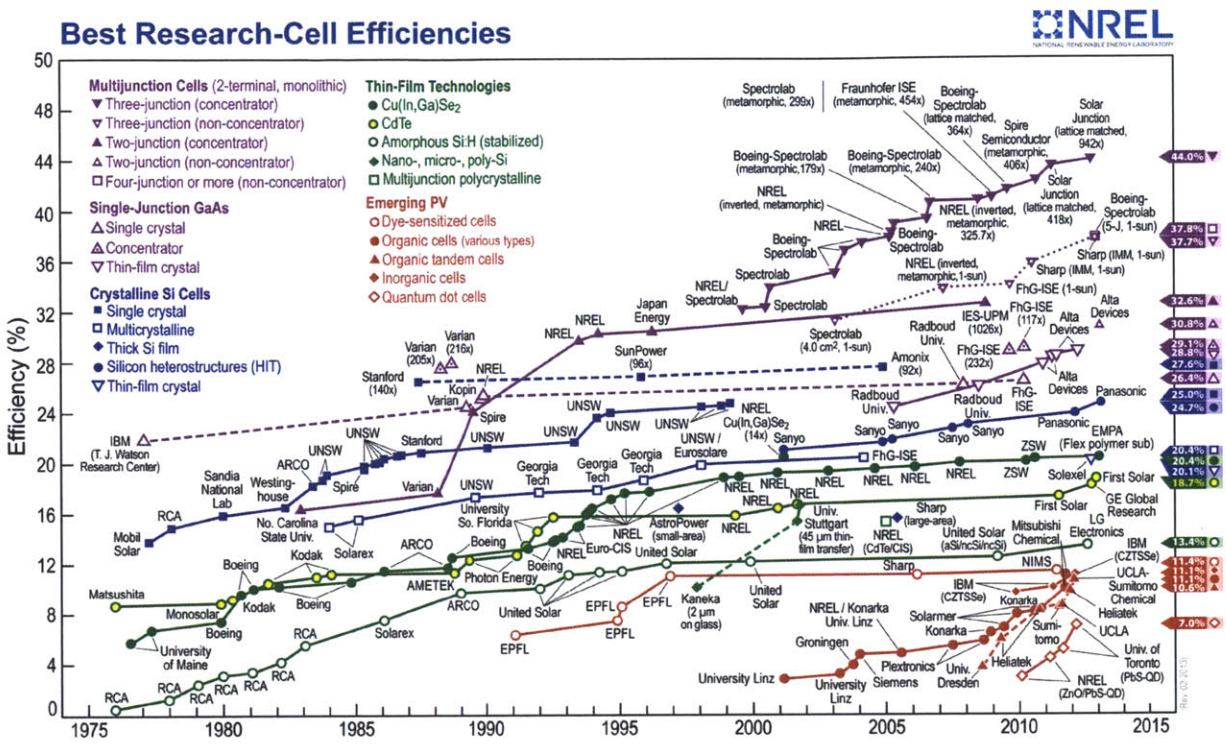

Figure 1.2: **NREL efficiency plot.** Nanoscale organic and QD solar cells are shown in the lower right of the chart.

2. The optical absorption, band gap, charge carrier mobility, ionization potential, and electron affinity of nanoscale materials can be tuned by tailoring their chemistry or using quantum confinement effects. This implies that within a same family of materials – for example, polythiophene polymers – optical absorption can be altered by chemical functionalization to better match the incident solar spectrum. As discussed below, materials for efficient nanoscale PV active layers achieve a delicate balance of certain optical and electronic properties. Hence the tunability of nanoscale materials serves as a great advantage for incremental efficiency improvements once the physical processes regulating energy conversion in the specific device are understood.

As discussed so far, PV includes several families of materials and technologies. The evolution of their power conversion efficiency (PCE) is captured by the ever-changing efficiency plot from the National Renewable Energy Laboratory (NREL)[11], shown in Figure 1.2. We note how the two key nanoscale PV families, namely organic and QD, occupy the lower right part of the plot due to their recent development and still relatively low efficiency compared to more established technologies. Importantly, steep efficiency *versus* time curves characterize nanoscale solar cells (Figure 1.2), illustrating their potential for rapid development toward higher efficiencies. In spite of efficiency growth trends, it is hard to predict the extent of future market penetration of

nanoscale solar cells in the big picture of the Terawatt-scale and grid-parity challenges facing PV technology. There are enormous challenges of practical and economic nature involved in taking a new solar cell technology from the lab to successful industrial commercialization, as proven by recent bankruptcy cases of start-up companies (*e.g.* Solyndra and Konarka) pushing novel and promising PV technologies. Although we warn the reader of this aspect, we will not elaborate further on this point.

The core of the work described in this thesis deals with the theoretical design of two novel families of nanoscale solar cells alternative to those based on conjugated molecules and QD. To this end, we employ techniques generally falling under the umbrella of computational electronic structure calculation methods. Our research efforts are supported by experimental work from our group as well as collaborators to develop proof-of-concept devices based on our predictions. Another component of this thesis is the discussion of a methodology to simulate the relevant aspects of nanoscale PV systems across different length and time scales, with the goal of predicting and optimizing solar energy absorption and conversion in a nanoscale PV device in a comprehensive way. Consideration of the multiple length scales involved in PV has led us to develop simulations of macroscopic assemblies of solar cells optimizing sunlight absorption and displaying a range of benefits.

1.2 Working Principles

Conventional solar cells such as those based on flat p-n Si junctions are minority carrier devices in which the crucial processes of photogeneration and recombination of charge carriers occur primarily in the bulk of the material. Charge separation is driven by an electrical potential gradient and occurs in a planar layer of a few μm thickness surrounding the depletion region at the p-n interface[12]. Due to the delocalized nature of electron and hole states in Si and other inorganic semiconducting crystals, sunlight absorption generates carriers with little spatial correlation. Since the dielectric constant ϵ is usually large (for example, $\epsilon \approx 12$ in Si), the Coulomb interaction between photogenerated electrons and holes is minimal, hence leading to small electron-hole binding energies much lower than kT ($\sim$26 meV at room temperature). The current generated in conventional solar cells is thus largely determined by the number of absorbed photons and the ability of photogenerated minority carriers (say, electrons in a p-type material) to escape from the device region where they are generated before recombining with majority carriers.

The working principle of nanoscale solar cells differs profoundly from the picture outlined above for conventional p-n junctions[13]. Conjugated small molecules and polymers possess significantly lower dielectric constants than Si and other bulk semiconductors, thus providing limited screening to the Coulomb interaction between charge carriers. Similarly, nanomaterials such as semiconducting carbon nanotubes, quantum dots, nanowires, and two-dimensional monolayers present low values of charge screening due to their high surface-to-volume ratio combined

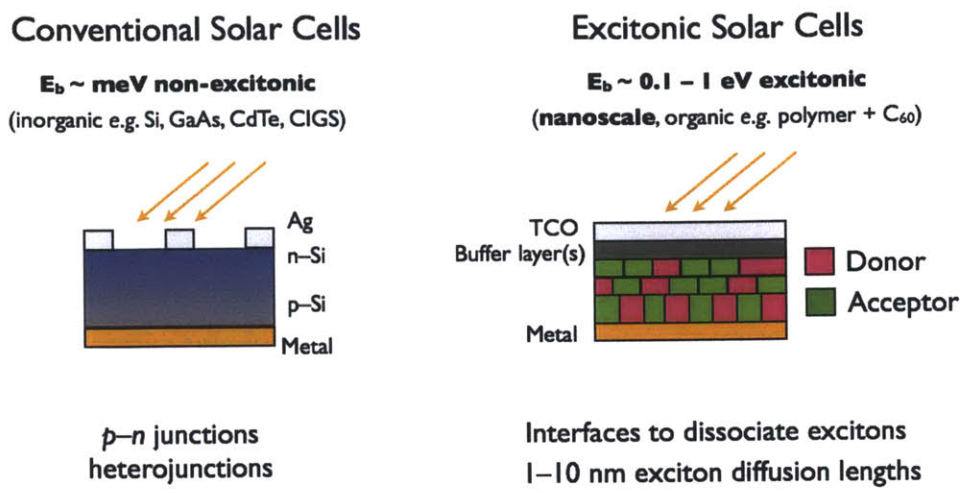

Figure 1.3: Conventional vs. excitonic solar cells. Conventional solar cells (left) are based on *p-n* junctions or heterojunctions in crystalline inorganic materials such as Si and GaAs. Excitonic solar cells (right) employ interfaces between two materials, called the donor and the acceptor, to dissociate strongly bound excitons in the active layer. A transparent conductive electrode (TCO) coated with buffer layers for additional charge and exciton management are commonly employed. E_b is the exciton binding energy..

with the low screening in the region surrounding the surface. For all these materials, photoabsorption results in an excited state constituted by an electron-hole complex with a binding energy of 0.1−1 eV in large excess of kT, deriving from Coulomb as well as exchange-correlation interactions. Such an excited state is called an *exciton*, and can be visualized as a mobile, charge-neutral species unaffected (to a first approximation) by electric fields; excitons formed by photoabsorption conserve the spin of the ground state, and are thus singlet states with zero spin. The smallest energy for exciton formation marks the photoabsorption onset and is called the optical gap (E_{opt}). It is smaller than the electronic energy gap (E_g) needed for the formation of a free electron-hole pair, the difference of the two being equal to the exciton binding energy $E_b = E_g - E_{opt}$. Due to the presence of strongly bound excitons, nanoscale solar cells are equivalently referred to as excitonic solar cells (XSC)[13] in the literature, a useful terminology to remind the reader that they are a class of PV devices distinct from their conventional counterpart. A comparison between conventional and excitonic solar cells is shown in Figure 1.3, summarizing the differences between these two types of PV devices. The primary function of an XSC is to dissociate excitons and transport the generated charge carriers with minimal energy losses to separate electrodes where they are selectively extracted. Exciton dissociation is commonly performed in XSC using heterojunctions between two semiconducting materials – called, respectively, the donor and the acceptor – with different valence band maximum (VBM) and conduction band minimum (CBM) energies. The VBM and CBM energy levels are equivalently called, respectively, the highest occupied molecular orbital (HOMO) and lowest

unoccupied molecular orbital (LUMO).

Figure 1.4 shows the relevant energy levels needed to establish energetic criteria for exciton

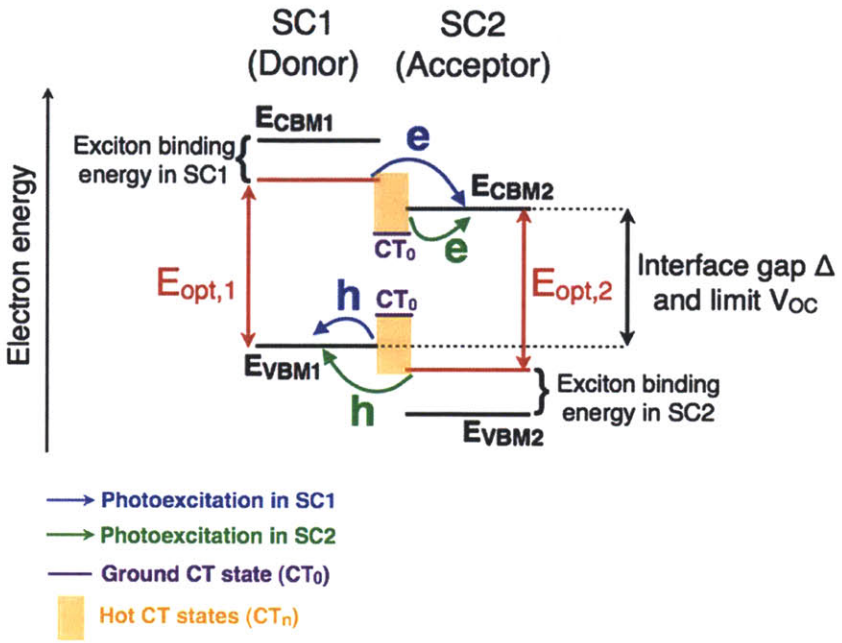

Figure 1.4: D-A interface energetics and type-II heterojunctions for XSC. The blue and green arrows show, respectively, the processes following photoexcitation of SC1 (the donor) and SC2 (the acceptor) in a type-II heterojunction. The electron and hole energies in ground CT_0 excitons are shown in purple, while the hot CT_n states are indicated in yellow as a continuum.

dissociation and charge carrier generation in an XSC, indeed a central point in this thesis. In what follows, the semiconductor with larger VBM energy (namely, smaller ionization potential) is called SC1, and the other semiconductor is called SC2; their VBM (CBM) energies are defined accordingly as E_{VBM1} (E_{CBM1}) and E_{VBM2} (E_{CBM2}), respectively. The first necessary condition we need to establish for exciton dissociation is that the interface presents a so-called type-II (staggered) alignment, namely that $E_{VBM1} > E_{VBM2}$ (our initial assumption) and $E_{CBM1} > E_{CBM2}$ are simultaneously satisfied[†]. Following photoexcitation of SC1, an exciton is formed that rapidly relaxes to the lowest-energy singlet excited state. Although an exciton is a two-particle system and thus strictly speaking cannot be visualized in the single-particle energy diagram in Figure 1.4, we focus here on the energy of an electron in the lowest-energy singlet exciton in SC1. Such a state is shown in red in Figure 1.4, and is energetically higher than E_{VBM1} by $E_{opt,1}$, the optical gap of SC1. Provided that the optical gap of SC1 is higher than the interface gap $\Delta = E_{CBM2} - E_{VBM1}$, the injection of an electron to the conduction band of SC2 at energy E_{CBM2} is energetically favored, and occurs provided the absence of unfavorable

[†]The case $E_{VBM1} > E_{VBM2}$ and $E_{CBM1} < E_{CBM2}$ corresponds to the formation of a type-I interface, in which excitons are energetically favored to transfer from SC2 to SC1 rather than being dissociated. Type-I interfaces are responsible for exciton transport in photosystem II of some photosynthetic organisms.

kinetics (see the blue arrow in Figure 1.4). As a consequence, a hole carrier is left behind in the valence band of SC1, and the net result is the generation of a pair of separated charge carriers: a hole in SC1 at energy E_{VBM1}, and an electron in SC2 at energy E_{CBM2}(Figure 1.4). Similarly, following photoabsorption in SC2 a singlet exciton is formed. The hole in such a state has an energy lower than E_{CBM2} by $E_{opt,2}$, the optical gap of SC2 (see the red line in Figure 1.4), given that the energy of holes increases in the opposite direction of the energy of electrons. The photoexcited hole can be injected to the valence band of SC1 at energy E_{VBM1} provided that the optical gap of SC2 is higher than the interface gap Δ, similar to what is found for the photoexcitation of SC1. We remark that regardless of whether it is SC1 or SC2 to absorb the photon, the final result after exciton dissociation is an electron in SC2 and a hole in SC1. For this reason, *SC1 is commonly called the donor, and SC2 the acceptor.*

To summarize, the first necessary condition for charge dissociation expresses the formation of a type-II heterojunction:

$$\begin{cases} E_{VBM1} > E_{VBM2} \\ E_{CBM1} > E_{CBM2} \end{cases} \tag{1.1}$$

Provided 1.1 is satisfied, the dissociation of excitons generated upon photoabsorption in SC1 requires:

$$E_{opt,1} \geq E_{CBM2} - E_{VBM1} \tag{1.2}$$

and the dissociation of excitons generated in SC2 requires:

$$E_{opt,2} \geq E_{CBM2} - E_{VBM1} \tag{1.3}$$

where in both cases, the righthand side is the interface gap Δ, and $E_{opt\,1,2}$ are the optical gaps of SC1 and SC2. There are additional requirements to guarantee effective energy conversion in XSC devices. First, excitons in nanostructures and organic materials commonly possess short diffusion lengths of $1-10$ nm, after which they decay either radiatively or non-radiatively (due to coupling with phonons or defects). This fact requires that following the formation of a localized exciton with random initial velocity, a donor-acceptor (D-A) interface should be available within $1-10$ nm from the point of photon absorption. For this reason, active layers consisting of disordered D-A mixtures in the so-called bulk-heterojunction (BHJ) morphology[7] are much more efficient than flat D-A bilayers in which only a small planar region ($\sim$20 nm thick) participates in exciton dissociation. The picture outlined here where excitons are thought of as classical particles moving with a random motion is particularly effective to model conjugated polymers where Frenkel excitons are strongly localized, but may break down in nanomaterials where the exciton radius is comparable in size to the thickness of the active layer (*e.g.*, in PbS QD).

Our discussion highlights how, different from conventional solar cells, electrons and holes are generated in pairs at the same point across an interface. Recently, an increasing amount of research has focused on the following dilemma: if an exciton is dissociated at a D-A interface, how can the generated electron and hole break free of their Coulomb interaction and avoid interface

recombination? We expand our discussion to explain, based on recent experimental findings, why this point is barely relevant in most circumstances and can be neglected to a first approximation when analyzing the energetics of the D-A interface to design efficient XSC. A bound exciton constituted by an electron and a hole localized across a D-A interface (the hole being on the donor, and the electron on the acceptor side) is called a charge-transfer (CT) exciton. Let's assume the formation of a CT exciton upon photoexcitation of the donor in Figure 1.4. An electron in the ground CT exciton state, called here CT_0, should have an energy lower than E_{CBM2} for otherwise it could be injected into the CBM of the acceptor and break free of the hole. For this reason, the CT_0 state should be regarded as a trap state hindering charge separation across the D-A interface. The energy for an electron in the CT_0 state is shown in Figure 1.4. We note that the energy to excite directly an electron from VBM1 to CT_0 is lower than the optical gap of SC1, and as such the existence of the CT_0 state can be probed by the presence of a peak at energy lower than $E_{opt,1}$ in a photoabsorption spectrum. Using this fact, a significant amount of experimental evidence has revealed the existence of CT states in a large number of D-A blends that nevertheless yielded devices with high photon-to-electron conversion efficiencies. This apparent contradiction can be explained by the existence of a number of higher energy CT states (known as "hot" CT states, called here CT_n) with higher energy than CT_0 (see Figure 1.4)[†]. As a consequence, once an exciton with energy equal to or higher than $E_{VBM1} + E_{opt,1}$ is formed upon photoabsorption in the donor, CT_n states higher in energy than CT_0 are readily accessible, and can favor electron injection into the conduction band of the acceptor while avoiding electron relaxation and trapping in the CT_0 state. This sequence of events leads to the formation of separated charges within very short time scales. Since the dynamics described here typically occurs at time scales of less than a picosecond, ultrafast time-resolved experiments are necessary to ascertain the precise mechanism of separated charge carrier generation. Recent pump-probe experiments[14,15,16] combining time-resolved absorption, second-harmonic generation, and photoemission spectroscopy have established for particular organic interfaces that hot CT_n exciton formation occurs on a timescale of 100 fs following donor excitation, while relaxation of CT_n exciton to CT_0 occurs $\sim$1 ps after the initial excitation. A key role seems to be played by the more delocalized nature of CT_n states compared to CT_0, thus favoring electron tunneling into the conduction band of the acceptor. These findings are rather general and hint at the fact that despite the presence of CT states, if the CBM of the donor and acceptor as well as the CT_n states are sufficiently delocalized, then exciton trapping at CT_0 occurs with low probability and does not hinder charge separation. Such information is valuable in modeling D-A interfaces as it suggests that accurate determination of CT states is often unnecessary given that in most cases they are not relevant for the energetics of solar energy conversion; on the other hand, CT states are crucial in determining the detailed subpicosecond dynamics at D-A interfaces.

We summarize our discussion by noting that exciton dissociation and charge generation at

[†]The existence of hot CT states can be understood in the spirit of a hydrogenic exciton model, or more simply in terms of an electron in a shallow energy well of depth $E_{CBM2} - E_{CT_0}$

D-A interfaces of nanoscale solar cells can be predicted by *computing a small number of spectroscopic quantities*, including the optical gaps of the donor and acceptor and the interface alignment of their VBM and CBM levels. A host of computational electronic structure calculation methods can be applied to compute these quantities, as explained in Chapter 2 of this thesis. The D-A interface model is thus useful to determine whether a certain material combination can work in an XSC, as well as to establish *upper limits and trends* for the current, voltage, and PCE as discussed later in this chapter. A number of factors beyond the dynamics at the D-A interface impact the actual performance of a real XSC. For example, processes related to exciton and charge transport occurring at the device length scale (μm to cm) are central to achieve a high PCE, and are therefore of interest when modeling nanoscale PV. However, models for exciton and charge transport at the device length scale tend to have a somewhat limited predictive character as they are commonly semi-empirical and require input parameters from either the experiment or more accurate theory, as well as employ simplified solar cell geometries. These aspects will be further examined in Chapter 4. We conclude that understanding the D-A interface is always a first necessary step in designing nanoscale solar cells, though the presence of a range of processes at higher length and time scales makes it difficult to predict the exact performance of a real device.

1.3 Materials and Devices

We provide a concise account of the evolution of different families of materials for nanoscale solar cells, as captured by the NREL plot in Figure 1.2. A large number of organic molecules and nanomaterials has been applied in nanoscale solar cells[17]. In polymer based XSC, initial studies have focused on the use of functionalized polythiophene donors (*e.g.* the P3HT polymer) in combination with the C_{60} fullerene or its chemical derivative PCBM as the acceptor. The P3HT/PCBM system has constituted a paradigm for polymer based PV for several years due to the high hole mobility in P3HT and ultrafast exciton dissociation at the P3HT/PCBM interface, resulting in record efficiencies of ~5 %[8]. Ultimately, the relatively large optical gap of P3HT (2.0 eV) limits the amount of absorbed sunlight, and polymer donors with lower gap in combination with C_{70} fullerene based acceptors have been developed to reach higher efficiencies of up to ~8 %[8,5]. Current record efficiencies for polymer based XSC are close to 10 % for tandem solar cells made by the Yang group at UCLA[5].

The other main family of organic XSC is based on conjugated small molecule donors such as phtalocyanines and perylenes in combination with a C_{60} acceptor[6,18]. After saturating at efficiencies around 4 % for several years before 2008, small-molecule XSC have recently seen a rebirth with current record efficiencies of up to 11 %, higher than the best polymer based devices. Organic small molecules offer limitless structural possibilities for improving key properties such as carrier mobility and morphology, and most importantly possess well-defined structures and high purity. While polymer solar cells are commonly deposited from solution, small molecules

can be deposited from both solution or vacuum evaporation. The latter approach is rather common in the literature since the small-molecule community applies expertise typical of the organic LED industry, thus making heavy use of vacuum processing methods to deposit thin-film active layers with precise morphology control. The use of vacuum deposition is particularly suitable to prepare tandem solar cells with broad absorption spectra and high efficiency. To date, the highest *published* efficiency for small-molecule PV is ~6 %, obtained by combining a Zn phtalocyanines donor with C_{60}, while higher efficiencies have been achieved by companies aiming at commercializing organic solar cells. Two companies are currently leading the research in small-molecule PV, Mitsubishi and Heliatek, both of which have reported efficiencies of above 10 % in 2012 (see Figure 1.2). Due to the potential for imminent commercialization, such recent developments are not being published in the scientific literature, and relatively little is known about the materials and architectures in these new high-efficiency devices[6]. The NREL plot in Figure 1.2 combines polymer and small molecule PV into a single category under the name of organic PV. Their current efficiencies of above 10 % are in principle adequate for commercialization, but the key remaining issue is the limited stability of active layer materials and packaged devices under combined exposure to sunlight and moisture, a problem especially relevant in polymer based PV. Understanding and preventing photodegradation processes is an area of focus in current organic PV research[19]. Other important aspects for future development of organic PV include: 1) Improving carrier mobilities beyond the present values of < 0.1 cm^2/Vs for most materials, thus enabling the use of thicker active layers desirable to absorb more sunlight; 2) Developing stable conjugated molecules with band gaps lower than 1.5 eV, a challenging goal since molecules with lower energy gaps tend to be less stable against photodegradation; 3) Understanding and designing improved buffer layers to favor selective hole/electron extraction and exciton reflection into the active layer. Buffer layers placed between the electrodes and the active layer are of crucial importance in modern XSC devices, and can dramatically impact their performance.

Another material family for nanoscale PV is constituted by colloidal QD[9]. While many semiconductors can be prepared in QD form by chemical synthesis, record devices have developed around the use of PbS (and more recently CdTe) reaching an efficiency of 7 %. One advantage in the use of QD is the possibility of tuning the optical gap from the far infrared to the visible by tuning the QD size, thus allowing effective harvesting of different portions of the solar spectrum. In addition, QD solar cells can be prepared in different configurations, including Schottky barriers, *p-n* junctions, and depleted heterojunctions. The main limitation of QD active layers is the low carrier mobility, deriving from a rather inefficient charge transport mechanism involving carrier hopping between nanocrystals passivated with electronically insulating ligands and possessing high surface trap densities. Due to the large exciton radius (over 20 nm) and small exciton binding energy in bulk PbS, experimental findings led by the Sargent group at the University of Toronto have been mostly explained in terms of simple models from conventional solar cells that neglect the presence of excitons. While the D-A interface model and the classical picture for exciton dynamics may need to be revised to model PbS QD solar cells, reliable models

cannot neglect the presence of excitons in the active layer. Other QD materials beyond PbS have potential for QD solar cells due to their large exciton Bohr radius (5 nm and above) and small bulk energy gap (1 eV and below). Examples include Pb(S,Se,Te), In(Sb,As), SnS and FeS_2 as a few promising cases of Earth abundant compounds[9]. In general, nanocrystals of these materials show strong excitonic effects, and thus the models described so far for organic XSC will form the basis for future theoretical developments in QD solar cells.

In this brief review of XSC, we have limited our attention to solid-state solar cells. An important family we have left out is known as dye-sensitized solar cells (DSSC). In their common implementation, these devices employ a molecular dye donor anchored to TiO_2 nanoparticle acceptors prepared in the form of a nanoporous film. A liquid electrolyte is employed to transport holes to the positive electrode, thus making this category of solar cells a hybrid between an electrochemical device and a solar cell. Recent work has shown the substitution of the liquid electrolyte with solid state hole conductors with ultrahigh (>500 cm^2/Vs) hole mobility, yielding efficiencies near 10 % in a solid-state DSSC. Other developments have involved replacing the molecular dyes with semiconducting QD absorbers, affording 9 % efficiency. This new type of solid-state, dye or QD based DSSC (also known with the misnomer of "mesoscopic solar cells") is still in its infancy and will not be discussed further. We refer the interested reader to a recent review at ref.[20]. In Chapter 3 of this thesis, we introduce two new families of ultrathin, tunable, photostable nanoscale solar cells based on carbon nanomaterials and two-dimensional monolayer materials. This thesis work has pioneered the theoretical study of both of these classes of materials in nanoscale PV. Starting from calculations presented in this thesis, our collaborators have prepared nanocarbon XSC with over 5 % efficiency. These devices are under NREL certification and may soon find place in the NREL chart in Figure 1.2.

1.4 Metrics and Figures of Merit

Similar to other energy conversion technologies, PV performance is measured using quantitative metrics and figures of merit. Since PV devices convert solar energy to electrical energy in planar devices, their efficiency can be measured as the ratio of output power to incident sunlight power, under reference illumination conditions and for a unit area. The reference for solar illumination is commonly taken as the AM1.5G solar spectrum (Figure 1.5a), representing solar radiation passing through 1.5 times the thickness of the atmosphere, which corresponds to a solar zenith angle of 48.2°. This choice represents a useful yearly average of solar radiation at mid-latitudes where most of the population, industry, and thus solar panel installations are located. For the numerical calculations of interest in this work, accurate data for the AM1.5G spectrum were obtained from NREL[21]. The AM1.5G spectrum can also be reproduced experimentally by applying a set of filters to a lamp in a solar simulator lab setup, an approach widely employed to test solar cells in scientific publications. The most common measure of the

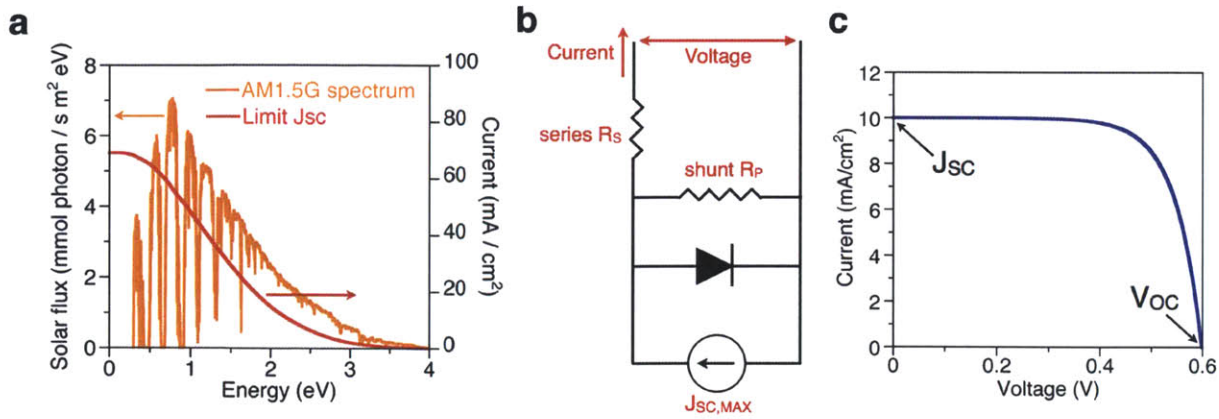

Figure 1.5: **Relevant variables in a solar cell. a,** AM1.5G solar spectrum from ref.[21] Also shown is the limit J_{sc} as a function of the optical gap, obtained by setting $A = 1$ in eq. 1.6. **b,** Equivalent circuit of a solar cell. **c,** J−V curve obtained by setting $R_s = 0$, $R_p = \infty$, $J_{sc,max} = 10$ mA/cm^2, and $J_D = 0.1$ μA/cm^2.

performance of a solar cell is the PCE under AM1.5G illumination, defined as:

$$\eta = \frac{J_{sc} \cdot V_{oc} \cdot \mathrm{FF}}{P_{in}} \tag{1.4}$$

where J_{sc} is the short-circuit current density (units of mA/cm^2), V_{oc} is the open-circuit voltage (units of V), FF is the fill factor (a dimensionless number), and P_{in} is the AM1.5G incident solar power density, with a value of 100 mW/cm^2 (also called 1 Sun). The numerator of eq. 1.4 is the power output from a unit solar cell area, and consists of three terms, each of which contributes linearly to the PCE and provides key insight into the physical processes occurring in the device. Before discussing this aspect in detail, we note the existence of an important limit to the PCE of solar cells, known as the Schockley-Queisser (SQ) limit[22]. The SQ limit dictates that under AM1.5G illumination the use of a single band gap for sunlight absorption in the active layer limits the PCE to a value of 33 %, and has been recently revised to show that in practical conditions the limit may be somewhat lower (∼30 %). Although the derivation is based on a conventional *p*-*n* junction model, the SQ limit is generally valid also for XSC when either the donor or the acceptor is the main absorber. The physical reason for the existence of the SQ limit is two-fold: 1) Photons with energy lower than the optical gap are not absorbed, while photons with energy higher than the optical gap generate excited carriers that quickly thermalize to band-edge energies before being extracted, thus losing the surplus energy; 2) While smaller energy gaps result in higher absorbed sunlight and currents, they lead to smaller voltages. Since the PCE is the product of a current and a voltage, this trade-off results in an ideal optical gap in the 1.3−1.5 eV range to achieve limit PCE values close to 30 %.

Next, we discuss in detail the origin of the three terms in the numerator of eq. 1.4. A solar cell, whether excitonic or not, is in its essence a diode-like rectifying device. Upon illumination, current flows in the device towards the contact with higher voltage, thus determining power

generation (*e.g.* like in a battery). The current is the result of separating photogenerated hole and electron carriers, and the voltage stems from the difference in the electrochemical potential of the carriers at the two contacts. An equivalent circuit for a solar cell, shown in Figure 1.5b, can be modeled as a current generator connected to a diode, a series resistance R_s, and a parallel resistance R_p, also known as the shunt resistance. The series resistance accounts for ohmic losses encountered as the carriers travel through the active layer towards the contacts, while the shunt resistance represents a short-circuit pathway between the electrodes leading to current loss, and is a way to model recombination as induced by impurities and defects in the active layer. In an ideal device, the series resistance is vanishingly small and does not lead to voltage loss, while the shunt resistance is infinite and does not lead to current loss by recombination. We write the equation for the current (J) as a function of voltage (V) for a solar cell modeled by the equivalent circuit in Figure 1.5b as:

$$J \approx J_{sc,max} - J_D \exp\left[\frac{q(V + JR_s)}{nkT}\right] - \frac{V + JR_s}{R_p} \tag{1.5}$$

where q is the elementary charge, J_D is an interface dark recombination current, $J_{sc,max}$ represents the maximum short-circuit current, and n is an ideality factor (a parameter equal to 1 for an ideal diode and to 2 for a high recombination regime). In the limit of $R_s \to 0$ and $R_p \to \infty$, eq. 1.5 reduces to the well-known Shockley diode equation under illumination, whose current-voltage characteristic is shown in Figure 1.5c.

The maximum short-circuit current $J_{sc,max}$ plays an important role in this thesis as it can be predicted from knowledge of the optical properties of the active layer, regardless of transport. In fact, $J_{sc,max}$ is simply the absorbed flux of photons, expressed as the equivalent electrical current when (under ideal conditions) every photon is converted to a carrier:

$$J_{sc,max} = q \int_{E_{opt}}^{\infty} J_{ph}(E) A(E)\, dE \tag{1.6}$$

Here, E is the photon energy, J_{ph} is the incident photon flux (Figure 1.5a for AM1.5G conditions), and $A(E)$ is the absorbance of the active layer, namely the fraction of absorbed photons at energy E. For the simple case of a flat active layer of thickness L, absorption coefficient $\alpha(E)$, and for p passes of light with normal incidence, the absorbance can be written as:

$$A(E) = 1 - e^{-p\alpha(E)L} \tag{1.7}$$

where the number of light passes p is usually equal to 1 or 2, depending on the arrangement of metallic and transparent contacts. The importance of eq. 1.6 lies in the fact that the absorption coefficient $\alpha(E)$ (and thus $J_{sc,max}$) can be computed with high accuracy using electronic structure calculation methods as described in Chapter 2. As seen from eq. 1.6, the two key quantities limiting the maximum short-circuit current in a PV device are the optical gap and the absorbance of the active layer material. The optical gap limits sunlight absorption to photon energies larger than E_{opt}, thus decreasing the available current even for active layers with unit

absorbance. Figure 1.5a shows the limit short-circuit current as a function of the optical gap, obtained from eq. 1.6 with $A = 1$. Out of a total current of 68.9 mA/cm^2 available under AM1.5G illumination, a significant fraction of 58 % lies at infrared photon energies of less than 1.5 eV, while 50 % derives from visible photons with 1.5−3.2 eV energy, and only 2 % from UV photons with energy greater than 3.2 eV. The absorbance in eq. 1.7 increases as a function of the active layer thickness and absorption coefficient. In a real device, a trade-off is needed to optimize the thickness, since thicker active layers require higher carrier mobilities for successful carrier extraction. The absorption coefficient $\alpha(E)$ is a property of the material constituting the active layer, and can be engineered to possess high values at energies where solar flux is higher, within limits dictated by optical sum rules[23]. [†] Out of the absorbed $J_{sc,max}$ photon current, only a fraction results in the device short-circuit J_{sc}, depending on carrier extraction efficiency. This aspect is quantified by introducing the energy-dependent internal quantum efficiency IQE, defined as the ratio of the electrical short-circuit current to the absorbed photon flux under monochromatic illumination with photons of energy E. We can thus write J_{sc} as:

$$J_{sc} = q \int_{E_{opt}}^{\infty} \mathrm{IQE}(E)\, J_{ph}(E)\, A(E)\, dE \tag{1.8}$$

Based on these definitions, IQE quantifies the efficiency for transporting and extracting photogenerated carriers. High IQE values near 100 % are a key indicator of a balance between active layer thickness and carrier mobility, the absence of high-density defects and traps, and efficient carrier injection into the contacts.

While the considerations examined so far for J_{sc} apply to both conventional and nanoscale solar cells, the open circuit voltage depends critically on the type of solar cell considered. Modeling V_{oc} is generally harder than modeling J_{sc}, and a large number of models have been proposed and applied. In conventional solar cells, V_{oc} is limited by the electronic gap of the active layer material, and is numerically equal to the separation of the quasi-Fermi hole and electron levels. This results in V_{oc} values usually lower by 0.3−0.4 eV than the band gap even in devices with efficient transport, both due to the inconvenience of doping the p and n layers degenerately and to subtle effects (under current debate) associated with the entropy change between absorbed and emitted sunlight[12,24]. In nanoscale XSC based on D-A interfaces, there is agreement that the interface electronic gap Δ (see Figure 1.4) is the upper limit for V_{oc}, since it corresponds to the difference between quasiparticle energy levels for the extracted electrons and holes. In many devices, V_{oc} has shown a linear dependence on both the donor's VBM and the acceptor's CBM, thus indicating that V_{oc} may be proportional to Δ and have the form[18,25]:

$$V_{oc} = \Delta - \text{loss term of 0.3 to 0.7 eV} \tag{1.9}$$

[†] Other strategies to enhance the absorbance include roughening the solar cell surface to increase the effective photon path within the active layer, and concentrating sunlight macroscopically using mirrors or locally using metallic nanostructures. This set of strategies falls under the umbrella of light management techniques in PV, and will be further discussed in Chapter 4.

where the loss term is commonly attributed to electron-hole recombination in the active layer or at the contacts. Recombination is in general more severe in nanoscale XSC compared to conventional solar cells due to large ratios between the D-A interface area and the macroscopic solar cell area. We can rationalize this fact by using an ideal diode model relating the current I to the voltage, the short-circuit current $I_{sc} = J_{sc} \cdot A$ (A is the device area), and the D-A interface recombination current $I_D = J_D \cdot A_{D-A}$ (A_{D-A} is the interface area between the donor and the acceptor):

$$I = I_{sc} - I_D \exp\left(\frac{qV}{kT}\right)$$

from which we extract the open circuit voltage by setting $I = 0$:

$$V_{oc} \approx \frac{kT}{q} \ln\left(\frac{I_{sc}}{I_0}\right) \tag{1.10}$$

We observe that in eq. 1.10 the ratio I_{sc}/I_0 is proportional to the ratio $r = \frac{A}{A_{D-A}}$ between the device macroscopic area and the D-A interface area, and $V_{oc} \propto \log(r)$. When the average domain size of the donor and acceptor decreases, the ratio r also decreases with a power law of the domain size thus leading to significant V_{oc} losses. This derivation clarifies why too small donor and acceptor domain sizes in XSC lead to significant recombination and generally low PCE. However, since small exciton diffusion lengths of order $1-10$ nm are found in most nanomaterials, effective charge generation requires nm to μm domain sizes. We conclude that optimal nanoscale solar cells employ intermediate domain sizes compromising between charge generation and recombination.

The third factor entering the definition of PCE in eq. 1.4 is the fill factor (FF), defined

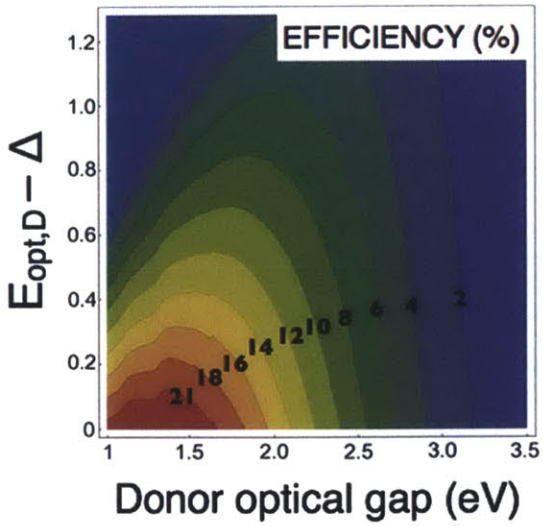

Figure 1.6: PCE trends in nanoscale solar cells. PCE level curves as a function of the optical gap of the absorber (assumed to be the donor in this case) and the effective conduction band offset $E_{opt,D} - \Delta$

.

as the ratio between the power generated by the solar cell and the $J_{sc} \cdot V_{oc}$ product. FF is a variable combining multiple effects linked to transport: in general, it decreases for increasing series resistance and decreasing shunt resistance, and is thus impacted by recombination, traps, and impurities. While ideal diode models predicts high FF values of 0.8–0.9[12], common FF values in nanoscale solar cells are in the 0.3–0.6 range, with maximum reported values near 0.75 for organic XSC[17].

Guidance towards the design of nanoscale solar cells with high PCE can be gained by using a model developed in this thesis and based on the work of Scharber *et al.*[25] We assume for simplicity that the main absorber is the donor (a common situation in organic solar cells), and adopt the limit conditions IQE = 100 % and $A = 1$, so that all sunlight above the donor optical gap $E_{opt,D}$ is converted to current. The short-circuit current obtained with this approach corresponds to an upper limit for a real device, but we shall be mostly concerned with trends in the PCE rather than absolute values. A reasonable FF value of 0.65 is assumed, and $V_{oc} = \Delta - 0.3$ V is chosen consistent with eq. 1.9. We fix the VBM, CBM, and optical gap of the acceptor, and study the PCE as a function of: 1) The donor optical gap, and 2) The effective conduction band offset γ between the lowest optically excited state in the donor and the CBM of the acceptor (see Figure 1.4):

$$\gamma = E_{opt,D} - \Delta = E_{opt,D} + E_{VBM,D} - E_{CBM,A}$$

where the D (A) subscripts refer to the donor (acceptor).

Figure 1.6 shows PCE contour lines as a function of $E_{opt,D}$ and γ. The plot suggests that tuning the optical gap and CBM energy of the donor for a fixed acceptor is an effective strategy to obtain high PCE values, and that the PCE varies significantly in response to moderate changes in the donor optical gap and CBM. The plot also shows two important design rules for efficient XSC: an optical gap around 1.4 eV is ideal for the absorber, consistent with the SQ model, combined with small γ values which favor high PCE since more of the donor gap contributes to V_{oc}. As pointed out in ref.[25], lines of constant donor VBM energies cut the plot with diagonals connecting low PCE to high PCE regions. Hence we conclude that when the main absorber is donor (acceptor), fine-tuning the absorber's optical gap and CBM level for a fixed VBM energy suffices to optimize the efficiency for a fixed acceptor (donor). The Scharber model has served as a guide for synthetic chemists over the last five years to search donor materials for efficient organic XSC based on fullerene acceptors.

2 Atomistic Simulations and Computational Spectroscopy in Nanoscale Photovoltaics

This chapter discusses the theoretical methods employed in this thesis to compute quantities of relevance in nanoscale PV. As outlined in Chapter 1, our main goal is to calculate the optical gaps, absorption spectra, and alignment of VBM and CBM energy levels of two materials at a D-A interface. These quantities can be measured experimentally using spectroscopic methods such as photoemission (for VBM and CBM levels) and photoabsorption (for optical gaps and absorption spectra), and for this reason their theoretical determination using computer calculations is referred to as *computational spectroscopy*. In this thesis, we employ *first-principles atomistic methods* to perform computational spectroscopy of novel materials and interfaces of interest in nanoscale PV. The methods employed to this end are density functional theory (DFT)[26], the so-called GW method (where G stands for the Green's function, and W for the screened Coulomb potential)[27], and the Bethe-Salpeter equation (BSE)[28]. Loosely speaking, these techniques are based on the solution of some form of the well-known time-independent Schroedinger equation:

$$H\,\psi(\mathbf{r}) = E\,\psi(\mathbf{r}) \tag{2.1}$$

where $H = T + V$ is the Hamiltonian of the system, equal to the sum of the kinetic energy T and the potential energy V, and $\psi(\mathbf{r})$ is a complex-valued wavefunction at the point of space $\mathbf{r}$. The GW and BSE methods rely on the framework of many-body perturbation theory, and in our work use the results of DFT calculations as a starting point. We refer to the methods employed here as *first-principles atomistic methods* since our quantum mechanical calculations do not require experimentally derived parameters, and the potential energy V entering the Hamiltonian is constructed based on the position and type of the atoms in the simulation cell, and no other information. We employ existing computational codes to construct the Hamiltonian of interest and diagonalize it in a plane wave basis set. Due to the use of plane waves, the simulation cell is defined as the unit cell of a Bravais lattice $\mathbf{R}$, so that only plane waves of the form $e^{i(\mathbf{k}+\mathbf{G})\cdot\mathbf{r}}$ with the periodicity of the lattice can be employed, where $\mathbf{k}$ is a vector in the Brillouin zone (BZ), and $\mathbf{G}$ is a vector of the reciprocal lattice. This formalism is general and can be employed for crystals – where the simulation cell coincides with a unit cell – as well as surfaces, interfaces, and nanostructures of any dimensionality, by leaving a large enough vacuum in the non-periodic directions to avoid spurious interactions with the image cells. As in most computational methods designed to solve differential equations, the representation of the operators is discretized in matrix form, and methods from linear algebra are employed to solve the problem. For this reason, convergence of all computed quantities with respect to the number of plane waves in the basis set and with the number of $\mathbf{k}$ points in the BZ needs to be carefully assessed in all calculations.

2.1 Density Functional Theory and Excited State Methods

We provide a concise discussion of DFT and the GW and BSE methods as tools to compute the spectroscopic quantities of interest in nanoscale PV. DFT is founded on the pioneering work of Hohenberg and Kohn (HK)[29], briefly summarized here. In a system of N electrons interacting with nuclei fixed at the equilibrium positions (in the spirit of the Born-Oppenheimer approximation), the external potential $v_{ext}(\mathbf{r})$ due to the nuclei and acting on each electron unequivocally specifies the nature of the system and the electronic Hamiltonian entering Schroedinger's equation. The two key theorems derived by HK show that the ground-state electron density $\rho(\mathbf{r})$ of the system is in a one-to-one correspondence with the external potential, so that all quantities of interest in the ground state, including the total energy E_{gd}, are functionals of the density. On this basis, the ground-state energy for the electronic system, corresponding to the Born-Oppenheimer surface for the chosen nuclear positions, can be derived by minimizing the energy functional $E_{gd}[\rho]$ with respect to the density. However, the functional $E_{gd}[\rho]$ is unknown, and approximate forms need to be employed for it in DFT. By introducing a fictitious non-interacting system of N electrons with the same ground-state density $\rho(\mathbf{r})$ as the system of the N interacting electrons under study, Kohn and Sham (KS) introduced a *self-consistent one-particle Schroedinger-like equation* to construct the density minimizing $E_{gd}[\rho]$. The resulting KS equation is a cornerstone of modern electronic structure calculations, and reads:

$$\boxed{\left\{\frac{-\hbar^2}{2m}\nabla^2 + v_{ext}(\mathbf{r}) + v_H[\rho(\mathbf{r})] + v_{xc}[\rho(\mathbf{r})]\right\}\phi_{n\mathbf{k}} = \epsilon_{n\mathbf{k}}\phi_{n\mathbf{k}}} \tag{2.2}$$

The one-particle KS Hamiltonian in eq. 2.2 is given by the sum of the kinetic energy $T = \frac{-\hbar^2}{2m}\nabla^2$, the external potential v_{ext} from the nuclei, the Hartree potential $v_H(\mathbf{r}) = \int d\mathbf{r}' \frac{\rho(\mathbf{r}')}{|\mathbf{r}-\mathbf{r}'|}$ for the repulsive interaction of the electron with the charge density from the N electrons in the system (including the self-interaction), and the exchange correlation potential v_{xc} capturing all electron-electron interactions beyond the Hartree term. The $\phi_{n\mathbf{k}}$ are KS orbitals, the $\epsilon_{n\mathbf{k}}$ are KS eigenvalues, and the subscripts n and $\mathbf{k}$ are, respectively, a band index and a vector in the BZ deriving from the use of a plane wave basis set in a periodic system.

The exchange-correlation potential is obtained as the functional derivative of the exchange-correlation energy E_{xc}: $v_{xc} = \frac{\delta E_{xc}}{\delta \rho}$, where $E_{xc}[\rho] = (T[\rho] - T_0[\rho]) + (V_{ee}[\rho] - V_H[\rho])$ is defined as the difference between the kinetic energy T of the interacting N electron system and the kinetic energy T_0 of the non-interacting system, plus the difference between the exact electron-electron interaction energy and the Hartree energy $V_H = 1/2 \int d\mathbf{r}\, v_H(\mathbf{r})\rho(\mathbf{r})$. The justification for this way of proceeding is to try to confine the unknown parts of the total energy in a small term E_{xc}, whose approximation would not result in dramatic errors in the total energy. In practice, there is a large number of possible approximations developed for E_{xc} and the resulting v_{xc}, and their nature can affect the DFT results quite significantly. The two most common local forms of v_{xc}, acting on the KS orbitals in a multiplicative way, include the local density approximation (LDA) and the generalized gradient approximation (GGA)[26]. These local forms

of v_{xc} have enabled successful calculations of a large number of properties of materials, although they fail to capture the non-locality (as well as other features) of the exact exchange-correlation potential. The external potential employed in the solution of the KS equation in this thesis is not the full Coulomb potential of the bare nuclei composing the system, since this approach would require the use of all the electrons – including those in core atomic states that do not participate in bonding – and hence the use of very large basis sets to guarantee the orthogonality of the valence electrons to the localized core electrons. In most of our calculations, we follow the common practice of including only the valence electrons of all the atoms employed. With this approximation, the external potential is given by a sum of pseudopotentials representing the nucleus plus the core electrons of each atom in the system, thus reducing significantly the number of electrons treated explicitly in the calculation and the overall computational cost*. Atomic pseudopotentials (PP) of different types can be used in DFT calculations, and a full discussion is outside the scope of this thesis. It suffices here to say that DFT codes available nowadays come with full sets of PP for most atoms in the periodic table, constructed by comparing a number of atomic properties to all-electron calculations[26].

The self-consistent solution of the KS equations results in the determination of the ground-state energy E_{gd}. This constitutes a great advancement in the study of materials, enabling one to calculate properties such as the relative stability of different phases, the elastic, vibrational, and thermal properties of materials, and their spontaneous polarization and magnetization. In addition to this list of properties which DFT is naturally designed to compute with high accuracy, it is tempting to further regard the KS equation 2.2 as a quasiparticle (QP) equation, implying that the energy levels $\epsilon_{n\mathbf{k}}$ could be interpreted as energies for addition and removal of electrons in the system. This would be a major achievement for determining spectroscopic properties of interest here, since the VBM energy E_v (and thus the ionization potential IP†), the CBM energy E_c (and thus the electron affinity EA‡), and the electronic gap E_g could be determined from the corresponding KS eigenvalues ϵ_v and ϵ_c, respectively the highest occupied and lowest unoccupied KS eigenvalues. This situation verifies in the Hartree-Fock equations, where Koopman's theorem[26] guarantees that the energy for the addition/removal of an electron is given by the one-particle eigenvalue of the orbital involved in the electron addition/removal process. In the framework of *exact* DFT, an analog of Koopman's theorem can be shown,

*While in s-p bonded systems it is common to include all the core electrons in the pseudopotential, in systems with d electrons it is sometimes necessary to include part of the core electrons explicitly in the calculation. It should be noted that although not employed in this work, the use of all-electron calculations treating all of the core plus valence electrons explicitly is necessary in some specific cases.

†The ionization potential is the positive energy difference between the vacuum level and the VBM.

‡The electron affinity is the positive energy difference between the vacuum level and the CBM.

yielding the following results:[30]

$$\epsilon_v = -IP \tag{2.3}$$

$$\epsilon_c = -EA - \Delta_{xc} \tag{2.4}$$

$$E_g = IP - EA = \epsilon_c - \epsilon_v + \Delta_{xc}. \tag{2.5}$$

where $\epsilon_c - \epsilon_v$ is the KS electronic gap, and the (positive-valued) exchange-correlation derivative discontinuity $\Delta_{xc} = \frac{\delta E_{xc}}{\delta \rho}(N + \delta N) - \frac{\delta E_{xc}}{\delta \rho}(N - \delta N)$ represents a discontinuity in $v_{xc} = \frac{\delta E_{xc}}{\delta \rho}$ as the number of particles is increased/decreased from N (for the neutral system) by a small amount δN. Eqs. 2.3−2.5 seem to suggest that DFT is well-equipped to compute spectroscopic levels using the highest occupied and lowest unoccupied KS eigenvalues. This is a somewhat surprising result considering that in the derivation of the KS equation, the KS eigenvalues merely play the role of Lagrange multipliers and thus by-products in the computation of the ground-state density. The caveat however is that in practice the KS equations are solved using *approximate* exchange-correlation functionals, so that eqs. 2.3−2.5 may not work to compute QP energies. For example, for commonly employed LDA and GGA functionals, the derivative discontinuity vanishes, so that the KS gap $\epsilon_c - \epsilon_v$ is lower than the experimental electronic gap (the difference being Δ_{xc}), usually by 30−50 %. Even when using non-local exchange-correlation functionals, the non-zero derivative discontinuity Δ_{xc} is difficult to compute and thus eq. 2.5 is of limited practical use to compute the electronic gap E_g from DFT. Similarly, while the highest occupied KS level should be the negative of the ionization potential and thus possess a physical interpretation as a QP level (see eq. 2.3), within common approximations for v_{xc} it can be off by as much as several eV from the experimental value[30]. The picture that emerges is that at present it is unclear whether DFT can provide QP energies and electronic/optical gaps, and much debate is ongoing regarding whether this is an achievable goal even in principle[30]. It must be noted that nevertheless it is not uncommon in the literature to interpret KS eigenvalues as QP levels, and in certain problems – largely due to error compensations – this approach can yield qualitative (if not quantitative) agreement with the experiment.

Next, we turn our attention to methods based on many-body perturbation theory (MBPT) to compute accurate values of the spectroscopic quantities of interest in nanoscale PV, and discuss in this context the GW and BSE methods used in this thesis. These approaches are in general much more computationally expensive than DFT, but guarantee spectroscopic results with state-of-the-art accuracy. Within the MBPT formulation of quantum mechanics, the central role in the theory is played by the one-particle (for GW) and two-particle (for BSE) Green's function of the system. We will not enter into the detailed formalism behind these methods, but will limit ourselves to discuss the key equations involved in practice and focus on some physical facts. Within the context of the one-particle Green's function, QPs are associated with the peaks in the spectral function, a quantity that can be accessed from photoemission experiments. If the peak is sufficiently sharp, a well-defined QP energy can be obtained. For the general case of an inhomogeneous electronic system like a material, the QP energies and wavefunctions can be

obtained by solving[27]:

$$\boxed{\left[\frac{-\hbar^2}{2m}\nabla^2 + v_{ext}(\mathbf{r}) + v_H(\mathbf{r})\right]\psi_{n\mathbf{k}} + \int d\mathbf{r}'\Sigma(\mathbf{r},\mathbf{r}';E_{n\mathbf{k}})\psi_{n\mathbf{k}}(\mathbf{r}') = E_{n\mathbf{k}}\psi_{n\mathbf{k}}(\mathbf{r})} \tag{2.6}$$

where $E_{n\mathbf{k}}$ and $\psi_{n\mathbf{k}}$ are, respectively, QP energies and wavefunctions, and Σ is the electron self-energy operator containing the effect of exchange and correlation among the electrons. The self-energy is in general a non-local, energy-dependent, and non-Hermitian operator, replacing the v_{xc} potential in the KS equation. The central difficulty in a QP theory is to find a suitable approximation for the self-energy. Within the GW method, the self-energy is taken as the first-order approximation of a perturbation series expansion of Σ in the screened Coulomb interaction W: this yields $\Sigma = iGW$ (hence the name of the method), where G is the one-electron Green's function, and $W = \epsilon^{-1}v_c$ is the screened Coulomb interaction, where v_c is the Coulomb potential, and ϵ^{-1} is the inverse dielectric tensor describing the dynamical electron screening in the system. A formally correct procedure to solve eq. 2.6 involves constructing G, ϵ^{-1}, and W starting from the KS eigenvalues and eigenfunctions, and then solving eq. 2.6 *self-consistently* until converged values of $E_{n\mathbf{k}}$ and $\psi_{n\mathbf{k}}$ are obtained. In practice, the self-consistent solution is very demanding, and it is highly debated in the literature whether full self-consistency on both G and W can lead to accurate results. In this thesis, we used the much more common approach of solving eq. 2.6 only once (the so-called "one-shot" GW, also known as the G_0W_0 method), which corresponds to applying first-order perturbation theory to the KS equation, thus correcting the KS eigenvalues $\epsilon_{n\mathbf{k}}$ by computing the diagonal elements of the perturbing potential $\Sigma - v_{xc}$:

$$E_{n\mathbf{k}} = \epsilon_{n\mathbf{k}} + \langle\phi_{n\mathbf{k}}|\,\Sigma(E_{n\mathbf{k}}) - v_{xc}\,|\phi_{n\mathbf{k}}\rangle \tag{2.7}$$

It should be noted that in this approach the QP orbitals are the same as the KS orbitals. In many cases this approximation is not severe, since self-consistent QP calculations updating the wavefunctions have shown that KS orbitals and QP orbitals are often almost identical, sometimes showing overlaps in excess of 99 %[31]. The reason for using the GW method in this thesis is two-fold: 1) The QP energies obtained from GW are useful *per se* to determine band alignments, and 2) GW calculations are a necessary starting point to compute photoabsorption spectra *including excitonic effects*, a task that can be accomplished within the BSE formalism employing an accurate treatment of the electron-hole interaction.

While the GW method can compute the QP energies for charged excitations of the system (adding or removing particles), optical excitations do not alter the total charge of the system but rather create electron-hole pairs, with significant Coulomb interaction in the case of nanomaterials due to the low screening. Hence photoabsorption in nanomaterials leads to the formation of excitons, a key ingredient to predict the optical properties of materials employed in nanoscale solar cells. The BSE is the method of choice to correctly take into account excitonic effects, since its formalism is grounded in the use of the two-particle Green's function. In the single-electron picture of band theory, one-particle optical transitions induced by light at visible frequency are

usually vertical in the BZ (due to low photon momentum), and excite an electron in a valence orbital to a conduction orbital at the same point $\mathbf{k}$ of the BZ. In contrast, excitonic transitions should be thought of as composed by weighted sums of all possible vertical transitions between one-particle valence states $\phi_{v\mathbf{k}}$ and conduction states $\phi_{c\mathbf{k}}$ at the same $\mathbf{k}$ point of the BZ. The excitonic wavefunctions $|S\rangle$ corresponding to excitation energies Ω_S are thus two-particle states mixing all possible optical transitions through coefficients $A^S_{c,v,\mathbf{k}}$:

$$\langle \mathbf{r_h}\, \mathbf{r_e}|\, S\rangle = \sum_{c,v,\mathbf{k}} A^S_{c,v,\mathbf{k}} \phi^*_{v\mathbf{k}}(\mathbf{r_h}) \phi_{c\mathbf{k}}(\mathbf{r_e})$$

The excitation energies Ω_S and the coefficients $A^S_{c,v,\mathbf{k}}$ entering the excitonic wavefunction can be obtained by solving the BSE, which amounts to diagonalizing an effective excitonic Hamiltonian H^{exc},[†] constructed by knowledge of the QP energies and the screening W from a GW calculation. Using a two-particle basis, the BSE to be solved reads:

$$\sum_{c'v'\mathbf{k}'} H^{exc}_{cv\mathbf{k},c'v'\mathbf{k}'}\ A^S_{c'v'\mathbf{k}'} = \Omega_S\, A^S_{cv\mathbf{k}} \tag{2.8}$$

The solution of eq. 2.8 requires choosing a number of $\mathbf{k}$ points and valence and conduction bands sufficient to converge the absorption spectrum up to the highest energy of interest in the problem. Knowledge of the energies Ω_S and excitonic wavefunctions $A^S_{c,v,\mathbf{k}}$ allows one to compute several optical properties of interest, as explained in the next section.

2.2 Calculation of Band Alignments, Optical Absorption, and Excitons

This section describes how the methods introduced in this chapter can be used to determine quantities of interest in nanoscale PV. We first turn our attention to the qualitative and quantitative determination of band offsets, as needed to determine the formation of type-II D-A interfaces. As discussed above, DFT in its practical implementations lacks the necessary accuracy for the determination of VBM and CBM energy levels involved in PV processes. However, the quantities of interest to determine band alignments in nanoscale PV are *energy differences*, such as valence and conduction band offsets, rather than absolute QP energies. Due to error compensation effects, DFT may be significantly more accurate in computing VBM and CBM energy differences, as discussed next.

Upon formation of an interface between two semiconducting materials, significant charge redistribution takes place, leading to the formation of a dipole with an associated dipole potential ΔV often with the same order of magnitude (1–1.5 eV) of the band gap of the materials involved (see Figure 2.1a)[31]. The interface dipole needs to be computed in a supercell containing an interface of the two materials, and added to the valence band offset (VBO) and conduction band offset (CBO). When starting from valence band offsets ΔE_v and conduction band offsets

[†]We skip here the derivation of the Bethe-Salpeter equation as well as technical details on how to construct and solve the excitonic Hamiltonian. The interested reader can find further information at ref.[28]

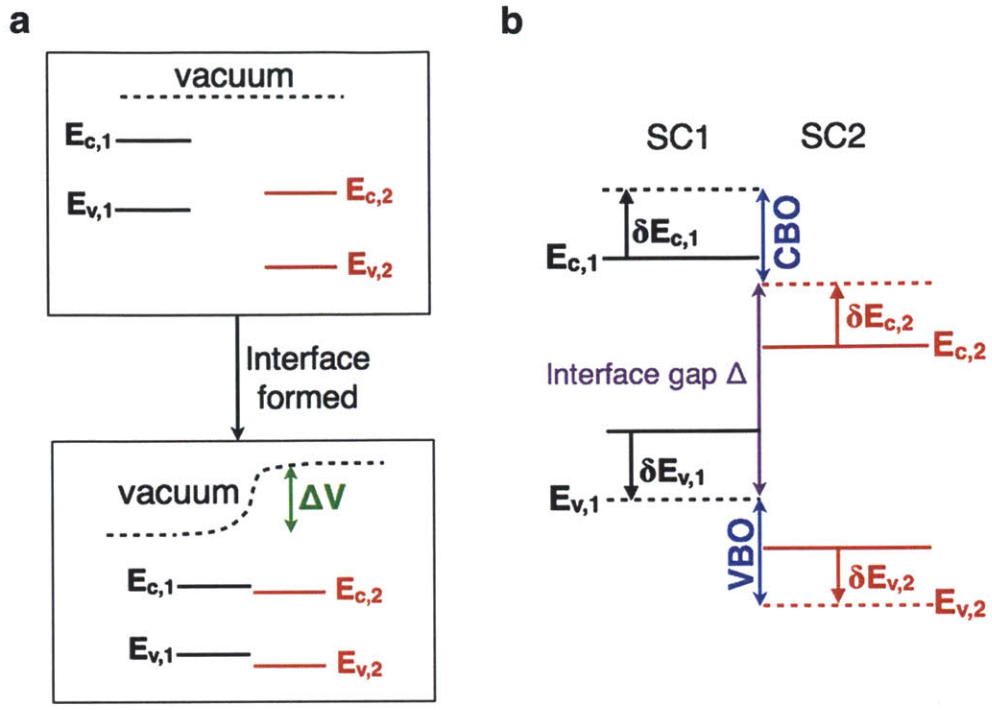

Figure 2.1: **Band alignment in DFT and GW. a,** Band alignment in DFT before the formation of an interface (upper panel) and after the formation of an interface. The dipole potential ΔV induces a significant change in the band alignment compared to the case of two isolated systems. **b,** DFT energy levels (shown as solid lines), and GW quasiparticle levels (shown as broken lines). When the GW correction is applied, the gap opens both in the donor (SC1) and the acceptor (SC2) material, causing shifts of the energy levels. Also shown are the VBO, CBO, and interface gap in the QP picture. Due to a compensation of errors, the VBO and CBO at the DFT level have similar values to the same quantities at the GW level.

ΔE_c obtained from calculations of the isolated materials composing the interface – thus not accounting for the interface dipole – the VBO and CBO can be computed as (see Figure 2.1):

$$\text{VBO} = \Delta E_v + \Delta V \tag{2.9}$$

$$\text{CBO} = \Delta E_c + \Delta V. \tag{2.10}$$

While this framework seems to require three separate calculations to determine the DFT band offsets (one for each isolated material and one for the interface to determine ΔV), the projected density of states (PDOS) of a single DFT calculation of the interface can yield both the VBO and the CBO directly. The PDOS is obtained by projecting KS orbitals of a given energy onto atomic orbitals localized at different atoms, thus providing an atom-resolved density of states. For interfaces between two semiconductors, peaks in the PDOS are found at the band edges for each material composing the interface, thus allowing one to determine VBO and CBO values within the broadening (of order 10 meV) used to compute the PDOS.

Comparisons performed in the literature between DFT and GW calculations of the dipole

potential ΔV at interfaces between semiconductors with only s and p electrons have shown only small discrepancies of the order 50−100 meV, suggesting that the dipole potential ΔV can be computed accurately within DFT[31]. This success of DFT is due to the fact that ΔV is mostly determined by the electrostatic potential at the interface, and thus by the ground state density which is computed accurately in DFT. Conversely, the determination of ΔV at interfaces between semiconductors and transition metal oxides containing localized d or f electrons can be much more challenging due to the self-interaction error in DFT leading to unnatural spreading of localized orbitals. As a rule of thumb, whenever the localization of valence electrons changes significantly between the two materials forming the interface (*e.g.* at metal/molecule or transition metal oxide/semiconductor interfaces), DFT is subject to larger and unpredictable errors in the interface alignments[32].[†] This fact generally holds true even with hybrid exchange-correlation functionals partially correcting the self-interaction error by employing a fraction of exact Hartree-Fock exchange. Since this thesis is mostly concerned with interfaces between *sp*-bonded semiconductors, we generally assume that ΔV can be safely taken from DFT calculations.

When ΔV is computed using DFT, QP corrections can be obtained from separate GW calculations on the two materials composing the interface, and have the net effect of shifting the VBM and CBM levels, respectively, by δE_v and δE_c (see Figure 2.1b). Within these approximations, the band offsets can be written as:

$$\text{VBO} = \Delta E_v + \Delta(\delta E_v) + \Delta V \tag{2.11}$$

$$\text{CBO} = \Delta E_c + \Delta(\delta E_c) + \Delta V. \tag{2.12}$$

where $\Delta(\delta E_{v,c}) = \delta E^1_{v,c} - \delta E^2_{v,c}$ is the difference between the VBM or CBM correction of the two materials. Several calculations at interfaces between *s-p* bonded semiconductors have shown that VBM corrections take similar values in the two semiconductors composing the interface, thus leading to small corrections $\Delta(\delta E_v) < 0.2$ eV of the DFT valence band offsets. As a result of this cancellation of errors, DFT is quite successful at computing the VBO for this class of interfaces, while for insulator-semiconductor interfaces the errors tend to be larger. Furthermore, when the DFT value of the VBO is assumed, the CBO $= \Delta E_c + \Delta(\delta E_g) + \Delta V$, and thus it is sufficient to determine the electronic gap E_g of the donor and acceptor in separate GW calculations to correct the CBO. Alternative methods to correct the electronic gaps include using experimental band gap values (when available), an approach commonly referred to as a scissor correction, or using hybrid functionals in a semi-empirical spirit by adjusting the fraction of exact exchange to the experimental gap. When the DFT error on the band gap of the two materials is of similar magnitude, $\Delta(\delta E_c)$ in eq. 2.12 is small, and *qualitatively correct* CBO values can be obtained

[†]This situation is similar to the DFT error in predicting atomization energies: when comparing systems of similar delocalization, the energy difference is in general reliable in DFT. However, when computing energy differences between two systems with very different electron localization, like a crystal and an atom in the calculation of atomization energies, the errors don't cancel and the results are usually quite poor.

from a single DFT calculation of the interface. We remark however that only GW calculations can achieve at present quantitative accuracy for CBO at interfaces between semiconductors, and avoiding the use of GW should only be done to reduce computational cost (see below). Once the band alignment is obtained with a judicious choice of the methods described above, the interface gap Δ (Figure 2.1b) setting an upper limit for V_{oc} in nanoscale solar cells can be extracted. In addition, by calculating the optical gap of the donor and acceptor using BSE, the effective band offsets $\gamma = E_{opt} - \Delta$ introduced in Chapter 1 can be computed, providing information on the possibility to dissociate excitons upon photoexcitation of a D-A interface.

Besides band offsets, the other key spectroscopic quantity we are concerned with in this thesis is the energy-dependent macroscopic dielectric function, linked to the optical absorption of the active layer material. The absorption coefficient $\alpha(E)$ at photon energy E introduced in Chapter 1 is proportional to the imaginary part of the dielectric function $\epsilon_2(E)$[23]:

$$\alpha(E) = \frac{E}{\hbar c\, n(E)} \epsilon_2(E) \tag{2.13}$$

where $n(E)$ is the refractive index, which can also be computed from knowledge of the dielectric function. The two equations used in this thesis to compute $\epsilon_2(E)$ derive from the DFT-RPA (where RPA stands for "random phase approximation") and the BSE approximations. The DFT-RPA approach is equivalent to the application of Fermi's golden rule to the KS system, and sums over vertical transitions (due to the small photon momentum $\mathbf{q} \to 0$) between independent particles using KS eigenvalues $\epsilon_{n\mathbf{k}}$ and orbitals $\phi_{n\mathbf{k}}$:

$$\epsilon_2(E) = \lim_{\mathbf{q}\to 0} \frac{8\pi^2}{q^2 V_{uc}} \sum_{vc\mathbf{k}} \left| \langle \phi_{c\mathbf{k}+\mathbf{q}} | \, e^{i\mathbf{q}\cdot\mathbf{r}} \, | \phi_{v\mathbf{k}} \rangle \right|^2 \delta(E - (\epsilon_{c\mathbf{k}+\mathbf{q}} - \epsilon_{v\mathbf{k}})) \tag{2.14}$$

where V_{uc} is the unit cell volume. The first peak in the DFT-RPA absorption spectrum corresponds to the optical gap as evaluated within DFT, which as discussed above lacks an accurate treatment of both the electron-electron and the electron-hole correlation. The BSE absorption spectrum, obtained by first finding the GW QP energies and then constructing and diagonalizing the BSE excitonic Hamiltonian in eq. 2.8, shows major differences from the DFT-RPA absorption spectrum, both in the intensity and in the position of the peaks. For the BSE case, the formula for ϵ_2 reads:

$$\epsilon_2(E) = \lim_{\mathbf{q}\to 0} \frac{8\pi^2}{q^2 V_{uc}} \sum_{S} \left| \sum_{vc\mathbf{k}} A^S_{vc\mathbf{k}} \langle \phi_{c\mathbf{k}+\mathbf{q}} | \, e^{i\mathbf{q}\cdot\mathbf{r}} \, | \phi_{v\mathbf{k}} \rangle \right|^2 \delta(E - \Omega_S) \tag{2.15}$$

This formula has an intuitive physical interpretation when compared to the DFT-RPA in eq. 2.14: it shows that at the BSE level, different one-particle vertical transitions are mixed in the oscillator strength and weighted by the excitonic wavefunctions $A^S_{vc\mathbf{k}}$, while the excitation energies Ω_S are not mere differences of quasiparticle levels. BSE optical spectra have shown remarkable agreement with the experiment for many semiconductors and oxides[†]. Two additional

[†]One of the key missing features in the BSE spectra is phonon-assisted transitions. These can be included in *ab initio* calculations with recently developed methods[33], and in most cases only lead to broadening of the absorption peaks.

quantities of interest in nanoscale PV that can be computed using the GW-BSE formalism are the exciton binding energy and wavefunction. The binding energy of the lowest singlet exciton can be obtained as the difference between the GW quasiparticle gap and the BSE optical gap, while the exciton wavefunction in eq. 2.1 can be obtained by fixing the position of the hole (electron) and plotting the square modulus of the excitonic wavefunction of the electron (hole), thus allowing one to establish the localization of an exciton formed immediately after a Frank-Condon optical transition when the nuclei haven't yet relaxed.

2.3 Computational Cost and Accuracy

When applying the framework discussed in this chapter to real systems of interest in nanoscale PV, the approximations adopted in practice as well as the computational cost need to be considered. In all the electronic structure calculations discussed here, the computational cost scales as some power of N, the number of valence electrons included explicitly in the calculation. The GW and BSE approaches are in general much more computationally demanding than DFT: while DFT scales as $\mathcal{O}(N^2)\log(N) - \mathcal{O}(N^3)$, GW scales as $\mathcal{O}(N^4)$[34], and the BSE scales as up to $\mathcal{O}(N^6)$ depending on the implementation and the approximations employed. The much larger computational cost of the GW-BSE approach in its current implementations compared to DFT explains why so much effort has been placed in extracting QP levels from DFT calculations. Using a parallel code installed on a modern computer architecture, a DFT calculation for an interface with ~1,000 valence electrons in the unit cell can be completed in approximately one day using 100 CPUs. For comparison, 1,000 electron GW calculations are unfeasible at present, and GW calculations with 100−200 electrons are already challenging and may require week-long calculations, especially due to the number of convergence tests required[†]. The additional computational cost in the GW method derives from the use of a large number of empty states to converge the screening matrix ϵ^{-1}, and additional time is spent in computing the matrix elements of the self-energy in eq. 2.7, requiring a double summation over the reciprocal lattice vectors involved in the calculation, as well as an integration over the BZ[27,34]. For these reasons, the convergence of QP energies in GW must be tested carefully as a function of the number of empty bands, $\mathbf{k}$ points in the BZ, and number of plane waves used to compute the screening.

In this thesis, we employed the QUANTUM ESPRESSO[35] and VASP[36] codes to perform DFT calculations, followed by, respectively, the Yambo[37] and VASP[38] codes for GW-BSE calculations. These codes differ somewhat in the detailed implementation of the equations presented in this chapter, but overall require similar computational resources to complete calculations of similar complexity. At present, efforts in the development of faster methods to estimate spectroscopic quantities of interest in nanoscale PV are being actively pursued, mainly in two directions: 1) Computing spectroscopic quantities more accurately using DFT, for example by

[†]The BSE method has higher computational cost than GW, but is in any case limited by the ability to perform a GW calculation that constitutes the starting point for BSE

computing the derivative discontinuity or developing Koopmans-compliant exchange-correlation functionals; 2) Reducing the cost of GW-BSE calculations by eliminating the use of empty states in the calculation of the dielectric matrix. For example, recent GW-BSE calculations without empty states have achieved BSE spectra in systems as large as 500 electrons. Other approaches to speed up GW calculations are driven by optimizing the numerical algorithms, and aim at taking advantage of the sparsity of the self-energy matrix to find faster linear algebra routines to compute QP energies. The hope is that in the near future both the DFT and the GW communities will generate highly scalable approaches to compute interface band alignments, optical absorption spectra, and excitons.

Beyond cost, computer calculations must be assessed for accuracy. There are several concerns when applying the DFT-GW-BSE ladder of approximations, including the quality of the pseudopotentials and of the KS orbitals. The former should reproduce as closely as possible all-electron results, while the latter should be free of the self-interaction errors typical of functionals not compensating for the self-interaction in the Hartree potential. Systems possessing d electrons are particularly critical in this respect, as we will discuss in our work on monolayer materials in Chapter 3. The accuracy of the electronic and optical gaps in GW-BSE calculations is usually within $100-200$ meV compared to experiment[28], although in some particular cases of oxides with localized electrons or shallow core states special care must be employed to achieve high accuracy. Band alignments and the interface gap are computed from combinations of QP energies, and thus their errors may compensate or add depending on the particular case. Of further concern when computing band alignments using GW is the fact that while energy gap corrections δE_g show little dependence on the numerical method chosen to obtain the self-energy[†], in some cases the corrections δE_v to the VBM and δE_c CBM show differences depending on the approximation used, sometimes by up to $0.3-0.5$ eV[31]. When the VBO is computed with sufficient accuracy within DFT, it is convenient for this reason to apply the correction only to the electronic gaps of the two isolated materials as described above.

When the ultimate aim in a calculation of a D-A interface for nanoscale PV is to estimate the PCE, special attention should be placed in estimating how errors in the absorber optical gap and band alignment affect the PCE. In our recent work[39], we have carried out an error analysis by computing the relative PCE error as a function of the error in the optical gap of the donor (considered as the main absorber) and the interface gap, considered as the V_{oc}[39]. The PCE was computed by assuming a constant value of the IQE and FF, so that these quantities do not enter the formula for the relative PCE error. Figure 2.2 taken from our work[39] shows that an accuracy of better than 0.2 eV in the absorber optical gap and D-A interface electronic gap is necessary to estimate the PCE with less than $20-50$ % relative error. We also show that errors

[†]The self-energy in the GW method is written as $\Sigma = iGW$, which translates to a convolution integral in frequency space. To avoid performing the integral explicitly on the real frequency axis, approximate models of the frequency dependence of W have been developed, called *plasmon pole models* as they capture the plasmon peak in the imaginary part of ϵ^{-1} using delta functions.

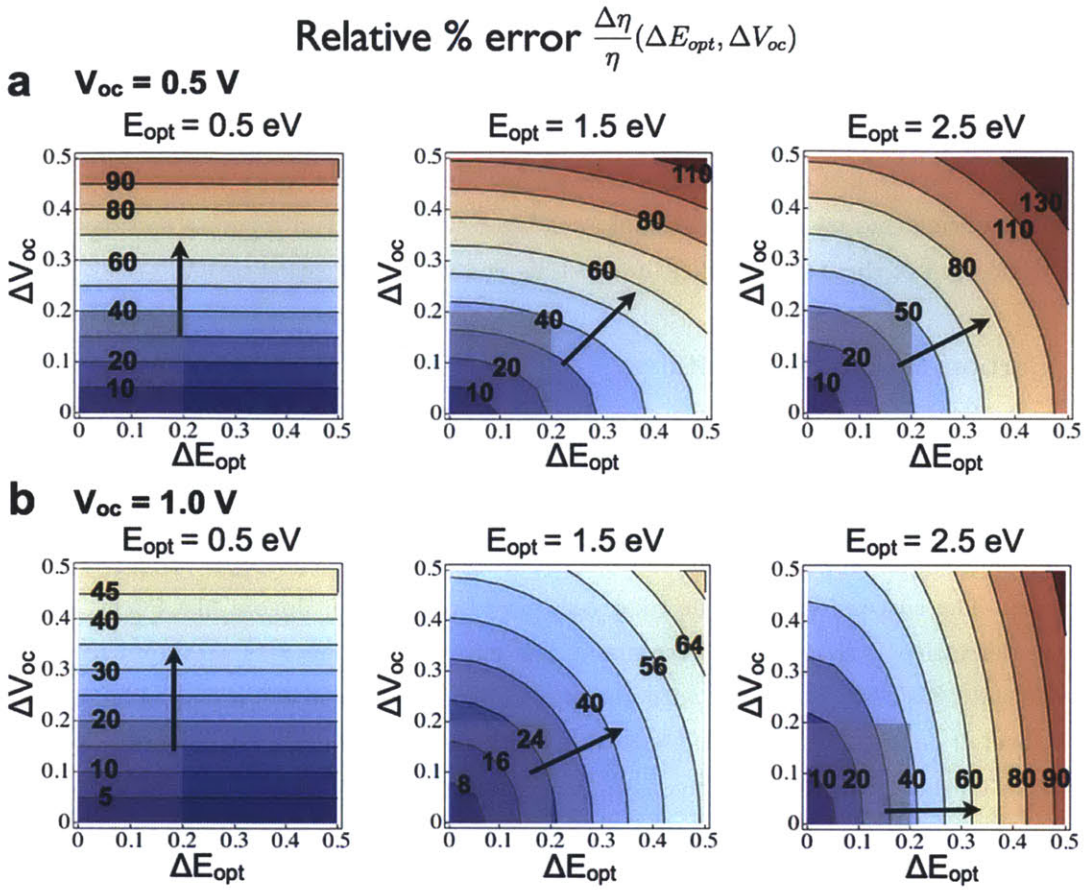

Figure 2.2: **Analysis of PCE errors.** Contour plots of the relative PCE error $\Delta\eta/\eta$ (in percent units) as a function of the open circuit voltage and optical gap errors (respectively, ΔV_{oc} and ΔE_{opt}). Two cases are shown with $V_{oc} = 0.5$ V in **a**, and $V_{oc} = 1.0$ V in **b**, each for three optical gaps $E_{opt} = 0.5$, 1.5, and 2.5 eV. The arrows point normal to the isoerror surfaces and thus in the direction of steepest error increase. The shaded squares indicate an area where both the ΔV_{oc} and ΔE_{opt} errors are kept below 0.2 eV, leading to material-dependent PCE relative errors in the 5−50 % range.

of 0.3−0.4 eV in these quantities can lead to material-dependent PCE errors of up to 50−100 %, largely undermining one's ability to rank materials for best PCE within a large set of candidates. The material dependence of the error combined with the large errors for even moderate errors on the electronic and optical gaps is of particular concern in the context of high-throughput studies of efficient nanoscale solar cells using large libraries of D-A pairs, as done recently for organic PV (see ref.[40]). On the other hand, it is not a particular point of concert in this thesis, where specific systems have been examined. We emphasize that knowledge of the spectroscopic quantities at D-A interfaces is chiefly useful to extract limit PCE values and trends, while the currents and voltages in a real solar cell device depend heavily on how efficiently photogenerated carriers are transported in the active layer and extracted at the contacts, as further discussed in Chapter 4.

3 Novel Materials for Nanoscale Solar Cells

This chapter describes the core research carried out in this thesis, consisting in the design of novel materials and interfaces for nanoscale solar cells using atomistic quantum mechanical calculations. The two new classes of solar cells we introduce here are based, respectively, on carbon nanomaterials and on two-dimensional monolayer materials. Two separate sections discuss our work on each of these two families of materials and their application to PV.

3.1 Carbon-Based Photovoltaics

3.1.1 From Polymer/Carbon Nanotube Solar Cells to All-Carbon Solar Cells

Single-walled carbon nanotubes (SWCNT) are attractive nanomaterials for the development of nanoscale solar cells due to their high carrier mobility and tunable optical and electronic properties. The success of nanoscale solar cells based on polymer donors like P3HT and the fullerene derivative PCBM as the acceptor[7,5] has encouraged numerous attempts to replace fullerenes with SWCNT acceptors, with the aim of improving transport in the polymer blend and the overall device efficiency. BHJ solar cells using blends of conjugated polymers as donors and SWCNT as acceptors in the active layer have been reported by several groups, but increasing their PCE has proven challenging[41,42]. Three key factors affecting the device performance are the nanotubes' electronic structure, their diameter, and the morphology of the active layer, as discussed below. Semiconducting SWCNT (s-SWCNT) display type-II alignment and ultrafast charge transfer with conjugated polymers such as P3HT, and it has been suggested that they can act as efficient acceptors at the interface with P3HT[43,44]. By contrast, recent investigations showed that metallic SWCNT (m-SWCNT) in the active layer have a detrimental impact on the photocurrent[42], and theoretical studies have predicted that the band alignment of P3HT/m-SWCNT is unfavorable for charge separation[43]. Prior to our work, most reported BHJ polymer/SWCNT solar cells were based on a typical mixture of non-enriched two-thirds semiconducting and one-third metallic SWCNT, and possessed significantly lower efficiencies than fullerene-based devices. For example, the polymer/SWCNT solar cells reported by Kymakis *et al.* with a PCE of 0.05%, achieved the highest efficiency for this type of device before our work[41].

Motivated by improving the efficiency of polymer/SWCNT solar cells, we have studied the structure of the D-A interface between P3HT and SWCNT of different chiralities using computer simulations. In collaboration with experimental collaborators, we employed the results of our structural study to guide the development of P3HT/s-SWCNT solar cells with a record PCE for this type of device of 0.72%[45]. A structural study of the D-A interface is a necessary step when dealing with organic-inorganic heterojunctions since their properties are strongly affected by the arrangement of the organic molecule at the interface attained during deposition from

solution. For example, an NMR study by Yang et al.[46] revealed the crucial role of the nanoscale arrangement of P3HT at the interface with PCBM, where annealing induces local separation of P3HT sheets and enhances the interface charge transfer at the interface. Their work suggests that besides the formation of a type-II heterojunction, the donor molecule's structure at the interface is critical, and extended polymer conjugation can favor charge transfer analogous to the effect of crystallinity in the bulk of semiconducting polymers[7].

To determine the structure of P3HT/SWCNT interfaces, we employed classical molecular dynamics (MD) simulations[47]. Classical MD as employed here time-propagates the classical equations of motion for the atoms using forces derived from semiempirical inter-atomic potentials able to reproduce some experimental property of the system. A range of constraints can be imposed to the system, including constant volume and temperature as adopted here. We will not delve into details of the method, but rather refer the reader to ref.[47] for further details. Our MD simulations are carried out using the LAMMPS code[48]. Briefly, we employ a constant temperature of 300 K using the Nose-Hoover thermostat[47] and a time step of 1 fs. A combination of classical force fields is adopted to describe the intramolecular degrees of freedom of the P3HT and the SWCNT and their intermolecular interactions (see ref.[45]). P3HT molecules are modeled using 20-repeat-units long chains with regioregular structure (rr-P3HT 20-mer, i.e., 40 thiophene rings) or 50 repeat unit long chains, which corresponds to approximately 1/10 of the length of rr-P3HT commonly employed experimentally. We study the interface of P3HT with three different SWCNT, including the zigzag (15,0), chiral (10,4), and armchair (8,8) nanotubes, all with a similar diameter of $\sim$12 Å.

In a first set of simulation runs, a single P3HT molecule was initialized at a distance of 9−10 Å from a single SWCNT surface, either orthogonal or parallel to the SWCNT axis to explore the role of different possible geometries when a polymer/SWCNT encounter occurs in solution. Our calculations indicate that regardless of nanotube chirality, folding of P3HT chains onto SWCNT is a relatively fast phenomenon (100 ps), following which the P3HT equilibrates and remains bound to the SWCNT surface. After equilibration, the competition between the $\pi-\pi$ stacking interaction and the torsional rigidity of the polymer determine the chain dynamics, and several structures are possible depending on the initialization and chain length. Figure 3.1a shows the formation of a P3HT helix with a pitch distance of 5.1 nm on a (15,0) SWCNT, closely matching the P3HT helical structure with 5.4±0.7 nm pitch observed in STM measurements of P3HT adsorbed on (15,0) SWCNT[49]. In other cases, the P3HT chain becomes kinetically trapped (within MD time scales) in disordered conformations closely resembling those observed in recent TEM measurements[50] (see Figure 3.1a). Since P3HT/SWCNT PV active layers are deposited from solutions of the two components, the assembly of the polymer chains on the nanotube begins already in solution. Given the strong adsorption observed at short time scales in our simulations, we suggest that the assembly process in the solution phase determines the final morphology of the active layer. On this basis, we simulate the assembly of a *larger set of P3HT chains and SWCNT as a function of SWCNT weight fraction in the blend*, and study the

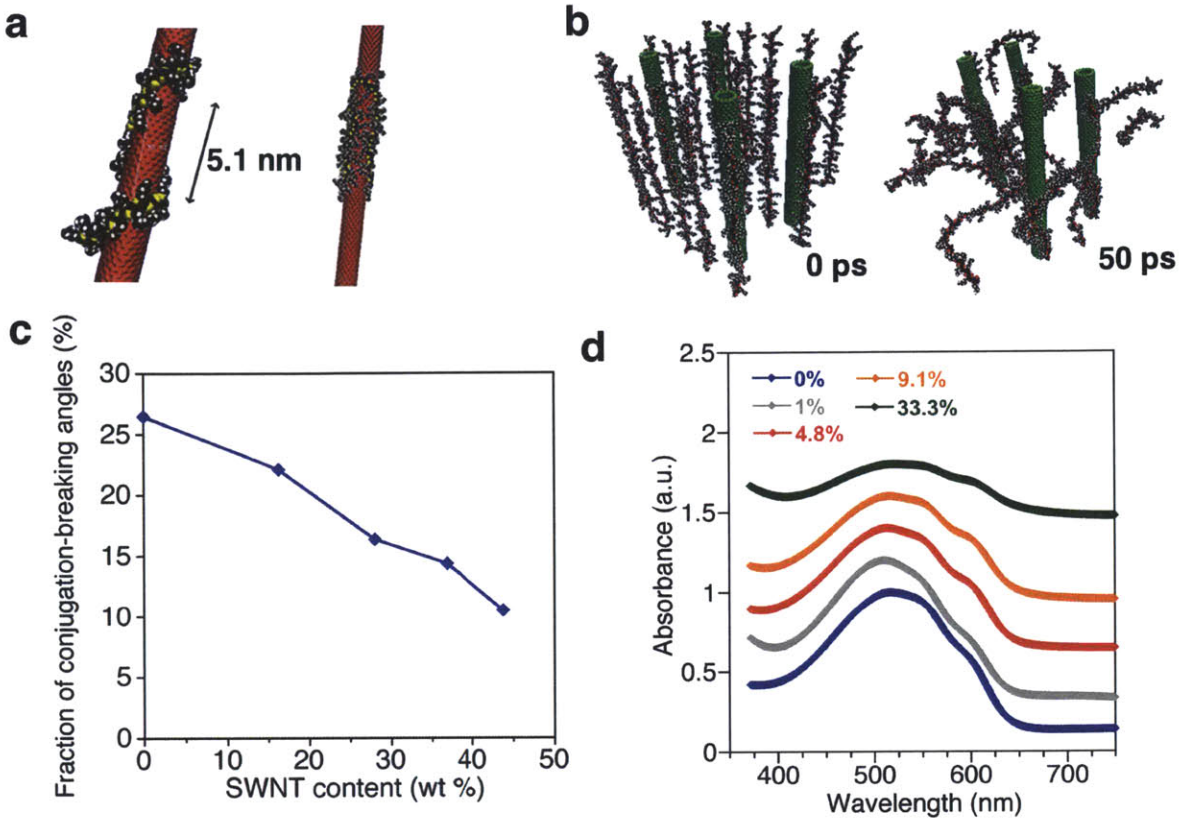

Figure 3.1: **Structure and properties of P3HT/SWCNT interfaces. a,** Locally stable conformations found using MD simulations and also observed experimentally. Left, a P3HT helix on a (15,0) SWCNT formed during the folding of P3HT 20-mers with orthogonal initialization. Right, a kinetically trapped "bundled" configuration. The SWCNT is shown in red, while the C, S, and H atoms in P3HT are shown, respectively, in black, yellow, and white. **b,** Simulation run of 20 P3HT 20-mer molecules and 40 wt % (15,0) SWCNT (shown in green) in a simulation cell with 30,000 atoms and periodic boundary conditions. Both the initial configuration and the configuration after 50 ps are shown. The C, S, and H atoms in P3HT are shown, respectively, in black, red, and white. **c,** Fraction of conjugation-breaking angles f for five different SWCNT concentrations. **d,** Optical absorption spectrum (in arbitrary units) of P3HT/DWCNT composites at different nanotube weight fractions. The curves are shifted to different baselines for clarity.

conjugation length – defined by the number of adjacent thiophene units arranged in a planar conformation – as a key variable determining charge transfer rates at the polymer-nanotube interface. The unit cell consists of twenty P3HT 20-mer chains initialized in the all-trans conformation, together with a number of (15,0) SWCNT necessary to span a composition range of 0–40 wt %. The initial configuration has a density of ~1/40 that of bulk P3HT (1.1 g/cm^3), resembling the situation of a drying P3HT/SWCNT solution where most of the solvent has been previously evaporated. Periodic boundary conditions are imposed throughout the runs to resemble an infinite medium. The initial P3HT/SWCNT arrangement, shown in Figure 3.1b,

evolves during the simulation to show P3HT adsorption on the SWCNT sidewalls as well as the formation of nanotube aggregates. For each SWCNT concentration, the conjugation length is sampled at 100 ps intervals after equilibration, assuming that a conjugation-breaking event results from torsion angles between adjacent thiophene units greater than 42°.[45] This procedure yields the time-averaged conjugation length as a function of nanotube weight fraction. Figure 3.1c shows the inverse conjugation length, expressed as the fraction f of conjugation-breaking angles; with this choice, the conjugation length expressing the number of adjacent conjugated thiophene units is $1/f$. As the concentration of SWCNT increases, f is seen to decrease monotonically, and the conjugation length $1/f$ increases accordingly. For example, the conjugation length increases from approximately $1/0.25 \approx 4$ thiophene units for pure P3HT to $1/0.1 \approx 10$ units (approximately 5 nm) for a SWCNT concentration of 40 wt %. The conjugation length attained at high SWCNT concentrations is close to the conjugation length for a single P3HT molecule at the interface with SWCNT (as verified in independent simulations), consistent with the presence of a large SWCNT area to adsorb P3HT at high SWCNT concentrations. This suggests the key role in imparting torsional order and higher conjugation lengths played by the SWCNT sidewalls, and specifically by the coplanar $\pi-\pi$ stacking.

The increase in conjugation length predicted from MD as a result of a larger nanotube fractions is supported by optical absorption spectra of P3HT/nanotube thin films with different nanotube weight fractions measured by our collaborator Dr. Michele Giulianini. In these experiments, the use of double-walled nanotubes (DWCNT) is preferred to SWCNT due to their superior transparency in the visible, mechanical stiffness, and thermal stability; on the other hand, the nanotube templating effect and interface structure should be the same as for SWCNT due to the closely related structures of SWCNT and DWCNT. Figure 3.1d shows UV-visible optical absorption spectra of P3HT/DWCNT films with nanotube concentrations in the 1−33 wt % range. The shoulder at 615 nm represents a transition due to interchain polymer absorption, corresponding to the formation of an exciton delocalized over multiple P3HT chains[51]. Higher absorption intensities at 615 nm are correlated to higher degrees of torsional order and conjugation in the polymer. As the DWCNT concentration is increased from 0 to 33 wt %, we observe an increase in the relative intensity of the interchain transition at 615 nm and the maximum intrachain transition intensity at 512 nm (see ref.[45]), by a factor of 1.45 for the highest DWCNT concentration compared to pure P3HT. This can be understood from the fact that when torsional rotations of the thiophene rings are reduced due to the ordering effect from SWCNT (or DWCNT), the overlap of the wavefunctions of neighboring chains increases and so does the intensity of interchain absorption. These experimental results, together with our MD simulations, provide strong evidence for the increase of the π-conjugation length of P3HT due to adsorption on the SWCNT sidewalls. As described in detail in our work in ref.[45], we further assess the impact of the conjugation length on the charge transfer rate, using Bardeen's tunneling theory to model charge transfer at P3HT/SWCNT interfaces. Our calculations indicate an increase in the charge transfer rate when the conjugation length is increased: for a doubling of the conju-

gation length (and thus of the initial electron state before charge injection into SWCNT), we predict an increase in the charge transfer rate by a factor of 2−20. Our results thus suggests that if a higher conjugation length can be achieved at the P3HT/SWCNT interface − by either increasing the nanotube weight fraction in the active layer, or by using the templating effect of SWCNT − more efficient charge transfer could be achieved, leading to higher currents in a PV solar cell. Notably, similar concepts attributing efficient charge transfer to the delocalization hot CT states (see Chapter 1) have recently received a great deal of attention from the PV community due to time-resolved spectroscopic experiments evidencing the role of delocalization in charge transfer[16]. In this sense, our estimate of the role of delocalization is the first of this kind, and may constitute a starting point for further investigation.

The design principles inferred from the interface structure study described above were employed to guide the preparation of P3HT/SWCNT solar cells with over 0.7% efficiency[52]. This work was performed in collaboration with Dr. Shenqiang Ren and Prof. Silvija Gradecak, who carried out the experimental part of the project described below. The active layers of the devices prepared by our collaborators are composed of P3HT/s-SWCNT nanofilaments, where each nanofilament consists of a s-SWCNT coated by P3HT (Figure 3.2a). The nanofilaments were prepared starting from a solution of P3HT and high purity s-SWCNT (98% purity nanotubes with a nominal diameter of 1.2−1.7 nm) prior to active layer deposition, as detailed in ref.[52] The resulting active layer morphology, analyzed using transmission electron microscopy and atomic-force microscopy, shows the presence of a large number of closely packed nanofilaments with 10−20 nm diameter (Figure 3.2b)[52]. By contrast, P3HT/s-SWCNT mixtures spin-cast from solution without nanofilament formation show a typical amorphous morphology with SWCNT embedded in a P3HT matrix. In addition to enhancing the P3HT conjugation, the nanofilament morphology prevents undesired nanotube bundling, defined here as the formation of μm-scale aggregates of nanotubes. SWCNT aggregation reduces the amount of interface available for charge separation, alters the properties of the isolated tubes, and restricts PV operation to low SWCNT concentrations.

The optical absorption spectrum of P3HT/s-SWCNT nanofilaments shows a strong absorption peak at 610 nm indicating a high degree of structural order in the polymer layer, imparted by the $\pi-\pi$ stacking as found in our MD simulations[45]. Upon photoillumination, the P3HT/s-SWCNT nanofilaments show a much stronger quenching of the photoluminescence compared to P3HT/s-SWCNT mixtures spin-cast from solution. This result confirms our theoretical prediction that higher conjugation at the P3HT/SWCNT interfaces leads to enhanced dissociation of excitons generated in the polymer[45,52], thus leading to stronger quenching of the photoluminescence.

We next investigated the dependence on SWCNT concentration x of the electrical and optical properties of active layers based on P3HT/s-SWCNT nanofilaments; these measurements are crucial to understand exciton and charge carrier dynamics in the nanofilament based active layers. Figure 3.2c−d shows the operating characteristics of P3HT/s-SWCNT nanofilament

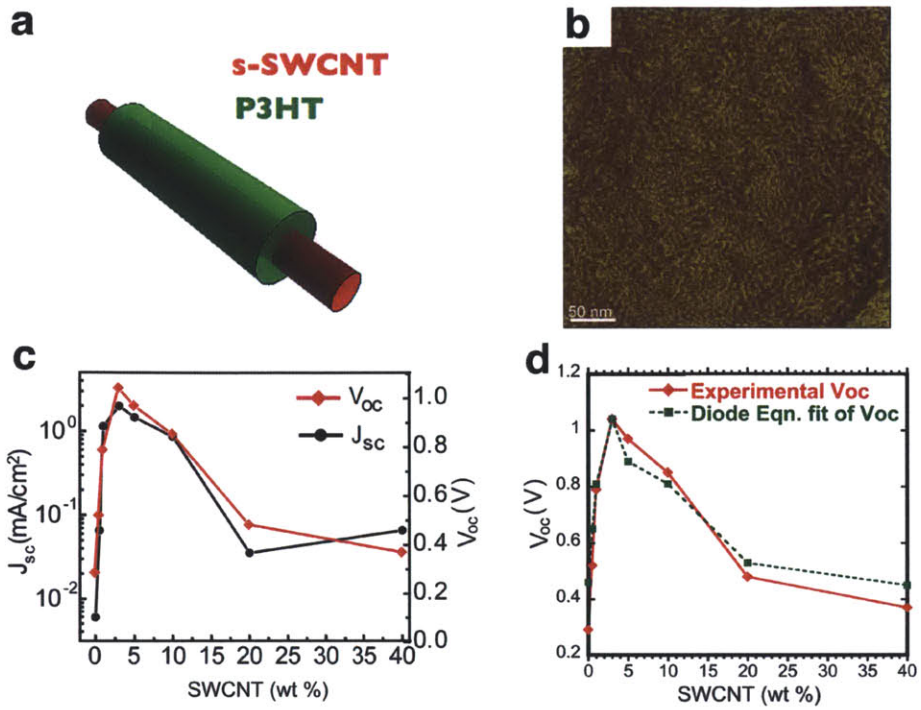

Figure 3.2: **P3HT/s-SWCNT nanofilament based solar cells. a,** Schematic image of a P3HT (green)/s-SWCNT (red) nanofilament employed in the active layer. **b,** AFM phase image of P3HT/s-SWCNT nanofilaments deposited in a thin film active layer with SWCNT concentration $x = 3$ %. **c,** Experimentally measured open-circuit voltage (red curve) and short-circuit current (black curve) as a function of SWCNT weight fraction in the active layer of P3HT/s-SWCNT nanofilament based solar cells. **d,** Comparison of the measured open-circuit voltage (red curve) with our model based on the biased diode in eq 3.1 (green curve). For SWCNT concentrations $x > 1$ % the dependence of V_{oc} on J_{sc} and J_D is well captured by the diode model.

devices at different nanotube concentrations (the results were obtained by averaging measurements from more than 20 devices for each nanotube concentration with a standard deviation of 4−5%); the complete set of results is reported in ref.[52]. Both the open-circuit voltage and the short-circuit current density are seen to increase with nanotube loading at low SWCNT weight concentrations (x < 3 %), until a peak value of $V_{oc} = 1.04$ V and J_{sc} =1.99 mA/cm^2 is achieved at $x \approx 3$ %, a SWCNT concentration value three times larger than the previously reported optimal concentration for mixed metallic and semiconducting SWCNT devices[41]. Notably, the best device with $x \approx 3$ % achieves a PCE of 0.72 %, which represents an increase by a factor of 15−20 over previously reported devices where both semiconducting and metallic SWCNT were employed in combination with a polymer. For the same SWCNT concentration of 3 % we also observe an increase in the J_{sc} by a factor of 350 compared to devices where only P3HT was used in the active layer, a clear sign that at least a fraction of the s-SWCNT form type-II heterojunctions and can effectively dissociate excitons in the active layer[52]. The increase in V_{oc} and J_{sc} at small SWCNT concentrations of less than 3 % can be attributed to the incipient for-

mation of a continuous percolating network in the SWCNT phase enabling charge transport to the electrodes, similar to the behavior observed in BHJ blends based on nanowires. At SWCNT fractions higher than 3 %, both the V_{oc} and J_{sc} decrease for increasing nanotube concentrations, while the dark recombination current J_D increases by over three orders of magnitude.

We interpret the decrease of V_{oc} for SWCNT concentrations above $x = 3$ wt % as an effect due to recombination; for SWCNT concentrations higher than $x = 1$ %, we find that V_{oc} can be related to the dark and short-circuit currents using a modified diode equation:

$$V_{oc} = \frac{nkT}{e} \ln\left(\frac{J_{sc}}{J_D}\right) + W \tag{3.1}$$

where $W = 0.76$ V is a biasing constant used here to match the value of V_{oc} at $x = 3$ %, and we set the ideality factor $n = 2$ for a regime where carrier recombination is dominant. With this choice, we find that for $x > 1$ % the dependence of V_{oc} on the nanotube concentration through the measured values of J_{sc} and J_D can be well captured by the simple diode model in eq. 3.1. The excellent agreement of this model with our data strongly supports our hypothesis that V_{oc} is regulated by carrier recombination processes. As discussed previously, modeling V_{oc} is challenging, and certain aspects of P3HT/s-SWCNT blends deserve further investigation. For example, the physical origin of the large correction W used here could be due to space-charge effects or to the formation of a large interface dipole modifying the band alignment[52]. The internal quantum efficiency (IQE) in the device with maximum PCE (see ref.[52]) shows contributions in the 1300−1400 nm wavelength region from optical transitions to the lowest-energy singlet excited state S_{11} in the nanotubes, achieving a maximum IQE value of 26 % at 1350 nm. Using this information in combination with the known optical gaps of s-SWCNT nanotubes as a function of diameter[53], we infer that the SWCNT contributing more substantially to the photocurrent possess a diameter of 1.3−1.4 nm, roughly equal to the average diameter in the sample[52]. The larger IQE for intermediate diameters seems to suggest a trade-off of different physical effects: smaller diameter nanotubes possess larger band offset favoring type-II alignment and exciton dissociation, while larger diameter nanotubes possess higher carrier mobilities and smaller exciton binding energies. Small IQE values in the 800−1100 nm spectral region further indicate that higher-energy S_{22} transitions do not contribute significantly to the photocurrent in spite of the larger band offsets, an effect likely related to a different exciton dynamics for such excitations.

In summary, our work shows the preparation of P3HT/s-SWCNT solar cells with a record PCE of 0.72% and a large $V_{oc} = 1.04$ V. The determination of current-voltage curves with an optimal SWCNT loading of 3 % suggests that the formation of larger D-A interface areas ultimately limits the device performance at high SWCNT content due to extensive carrier recombination, consistent with our discussion in Chapter 1. Despite the relatively low maximum PCE values obtained, we believe that our work shows insight into the working principles of P3HT/s-SWCNT solar cells. Another crucial factor for our work on carbon based solar cells is the observation that at very large nanotube fractions of ~40 % (see Figure 3.2c) we find an open circuit voltage of 0.4 V, similar to the band gap of the nanotubes with larger diameters in the blend. This

fact inspired us to study active layers where the polymer is completely absent, and only carbon nanomaterials are employed. Since the polymer is at the origin of the photodegradation in organic solar cells[19], the investigation of polymer-free nanoscale PV devices is also motivated by the pressing need to create solution processable solar cells with long-term stability. Our work on nanocarbon based solar cells has guided the preparation of efficient and photostable solar cells with polymer-free active layers based entirely on carbon nanomaterials, as discussed in the next section.

3.1.2 Efficient Nanocarbon Solar Cells

Carbon, one of the few elements known since antiquity, holds remarkable potential as an inexpensive material for solar cells[54]. Not only is it abundant in the Earth's crust (~0.2 wt %), but it can also be found in nature in several forms such as graphite, diamond, and coal, and it is widely used technologically with a record production among other elements of 9 Gt/year[55]. Nanostructured carbon allotropes such as SWCNT, fullerenes, graphene, and their chemical derivatives hold record values for physical properties important for PV such as carrier mobility and optical absorption, and are appealing for PV due to their thermal and photostability. In addition, carbon nanomaterials can be dissolved in organic solvents to deposit thin solar cell active layers from solution, thus presenting the same manufacturing advantages of polymer based solar cells (solution processable, potentially flexible, and chemically tunable) but with increased photostability. Other carbon allotropes such as amorphous carbon, nanodiamonds, and graphene can be deposited in thin film form on flexible substrates using chemical vapor deposition, similar to other thin film solar cell technologies such as amorphous Si and $CdTe$[2]. While there has been intense focus on the use of carbon nanomaterials in electronics and photonics[56], the potential of carbon as the active layer material in PV is still largely unexplored. In PV, carbon materials have been mainly used as acceptors in polymer-based solar cells or as transparent electrodes, buffer layers, interfacial layers, and interconnects[54], but only recently as the main sunlight absorbers in PV active layers. The use of pure carbon materials with strong carbon-carbon bonds to host photogenerated excitons has a dramatic potential to enhance the photostability of solution processable solar cells, and is an approach similar to how the stability problem has been solved in organic LED – indeed, by using materials with strong bonds and high purity. We discuss our work on carbon based solar cells starting from the *design of efficient active layers made completely out of carbon nanomaterials and free of conjugated polymers and small molecules.* We remark that the carbon based devices discussed here are radically different from polymer based solar cells with fullerene acceptors: the carbon content of the active layers of our carbon based devices can be as high as 90 at. %, *versus* a much lower fraction of ~40 % for polymer based PV. Hence the active layers discussed here are nearly "all carbon".

In our first paper on this topic[57], we employed DFT calculations to compute the valence and conduction band offsets (ΔE_v and ΔE_c, respectively) of $PC_{60}BM$/s-SWCNT interfaces and

predict the band alignment as a function of s-SWCNT diameter d. As explained above, only semiconducting nanotubes are considered since metallic SWCNT have been shown to decrease exciton lifetime significantly, as well as short-circuit the device even when present in small concentrations[58]. The DFT calculations were performed using the QUANTUM ESPRESSO[35] code. We employed the Perdew-Burke-Ernzerhof (PBE) exchange-correlation functional[59], and a kinetic energy cutoff of 35 Ry was used for the plane-wave basis set and of 200 Ry for the charge density; ultrasoft pseudopotentials[60] were used to describe the core electrons. An orthorhombic unit cell with 10 Å vacuum in the non-periodic directions was employed. Between 1 and 4 s-SWCNT repeat units (depending on the nanotube chirality) were used with a Monkhorst-Pack $\vec{k}$-grid of $1 \times 1 \times n_z$, where n_z values up to 20 were used to achieve convergence in the Brillouin zone sampling in the nanotube axis direction. The PCBM was placed at a van der Waals distance of 3.3 Å from to the nanotube, and all structures were relaxed to less than 50 meV/Å in their residual atomic forces. The final calculations were carried out on such combined $PC_{60}BM$/s-SWCNT systems with up to ~1,000 valence electrons. The valence and conduction band offsets were computed as differences in the peaks of the projected density of states (PDOS). While this method can yield accurate interface dipoles and valence band offsets for *sp*-bonded materials interacting by van der Waals forces[31], accurate estimates of the conduction band offsets can only be achieved as a consequence of a compensation of the DFT error on the energy gaps of the two materials composing the interface, as typical when employing local exchange-correlation functionals such as the PBE (see Chapter 2). For the interfaces studied here with up to 1,000 valence electrons, more accurate calculations with non-local functionals (*e.g.*, hybrid functionals or the GW self-energy) would be extremely time-consuming and almost unfeasible at present. Nonetheless, the error cancellation on the DFT band gap for both the s-SWCNT and $PC_{60}BM$ composing the interface leads here to qualitatively correct trends and band offsets as shown below.

For all s-SWCNT studied here (with diameter $d = 0.75-1.7$ nm), the nanotube HOMO level is found to be higher in energy than the HOMO of PCBM (*i.e.* $\Delta E_v > 0$ in Figure 3.3a), and thus the HOMO orbital of the interface is localized on s-SWCNT. For small d between 0.75−1.2 nm, positive conduction band offsets are found, as confirmed by the interface LUMO orbitals localized on the nanotube (Figure 3.3a). A type-II alignment favorable for PV operation is thus predicted for nanotube diameters smaller than approximately 1.2 nm. In particular, for the (6,5) nanotube ($d = 0.75$ nm) constituting up to 50% of the small diameter s-SWCNT sample used in our experiments, the alignment is predicted to be type-II with $\Delta E_c \approx 0.2$ eV, as shown in Figure 3.3a. We also observe that the small-diameter (10,0) nanotube ($d \approx 0.8$ nm) is an outlier and yields type-I alignment within our DFT calculation; however, the lack of contribution to the photocurrent from the (10,0) s-SWCNT is irrelevant given the large number of chiralities in a s-SWCNT sample with diameters of 0.75−1.2 nm. For large diameter nanotubes with $d >$ 1.2 nm, the LUMO levels of PCBM and s-SWCNT become nearly degenerate, and the LUMO orbital is seen to extend across the interface (Figure 3.3a), thus yielding type-I alignment. Based

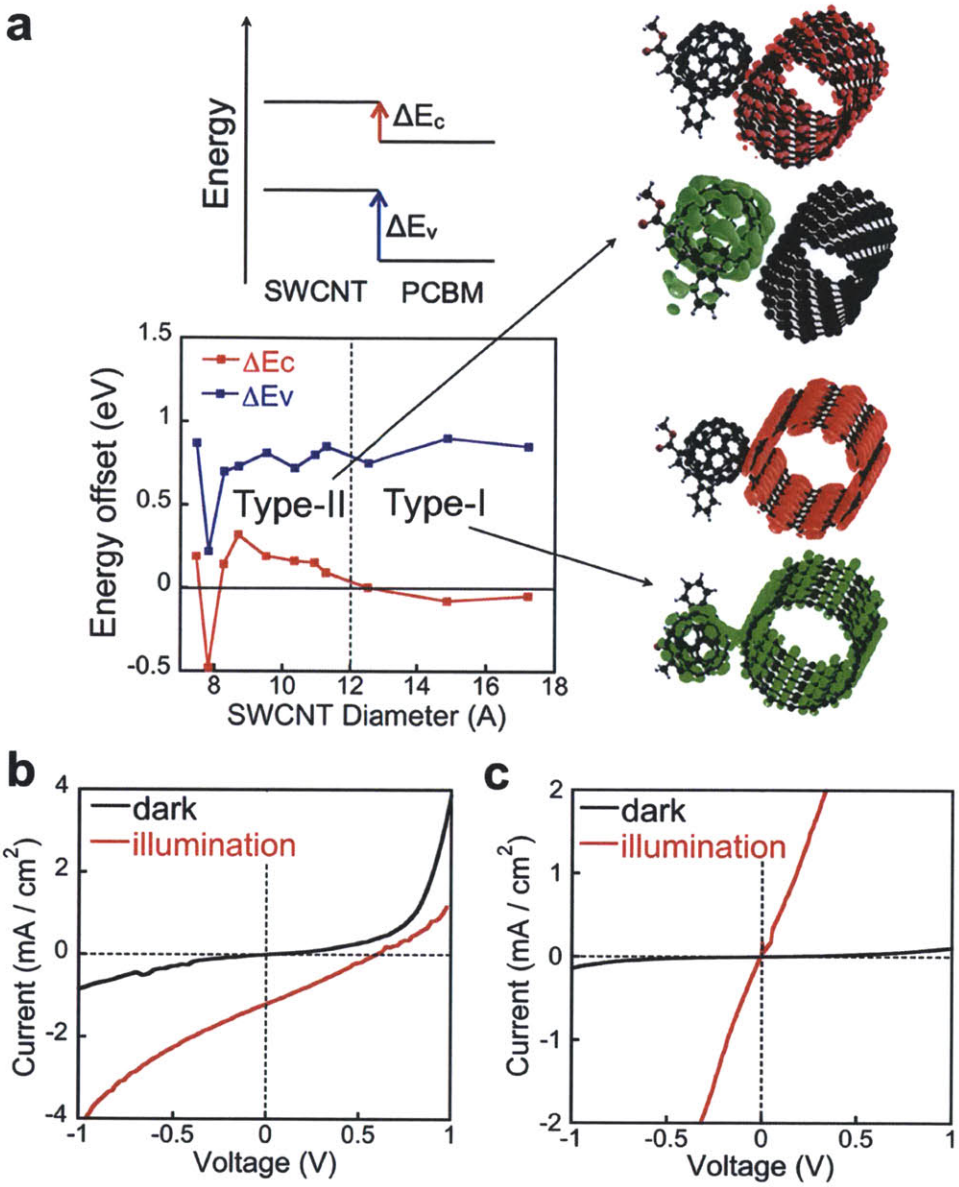

Figure 3.3: **Band alignment at s-SWCNT/PCBM interfaces. a,** Energy offsets of HOMO (ΔE_v) and LUMO (ΔE_c) levels for PCBM/s-SWCNT interfaces, calculated using DFT and shown as a function of nanotube diameter. The offsets are referenced to the HOMO and LUMO levels of the acceptor, as shown above the plot. The two diameter ranges with type-I and type-II alignment are indicated and delimited by a vertical dashed line at $d = 1.2$ nm. The smallest diameter shown is the (6,5) nanotube, with type-II alignment and $\Delta E_c \approx 0.2$ eV. Also shown are charge density plots for the HOMO (in red) and LUMO (in green) orbitals for type-II and type-I cases, as indicated by the arrows. The band offset predictions are confirmed by measurements of the current-voltage characteristics, shown in panel **b** for our fabricated devices with nanotube diameter of $0.75-1.2$ nm, and in panel **c** for devices with nanotubes with $d > 1.2$ nm. The same trends are found if $PC_{70}BM$ is used instead of $PC_{60}BM$.

on these trends, a rectifying behavior with non-zero PV efficiency is expected for a BHJ device employing PCBM and s-SWCNT with $d \approx 0.75 - 1.2$ nm in the active layer, while ohmic behavior and no PV effect are expected in a device employing PCBM and s-SWCNT with $d > 1.2$ nm due to the presence of degenerate LUMO levels. As a result, we deduce that a maximum $d \approx$ 1.2 nm needs to be employed for favorable PV operation in a PCBM/s-SWCNT active layer.

Our collaborators have verified experimentally our DFT predictions by preparing BHJ solar cells using PCBM and diameter-sorted s-SWCNT, and found excellent agreement with our interface calculations, both for $PC_{60}BM$ and $PC_{70}BM$ (Figure 3.3b–c)[57]. In practice, $PC_{70}BM$ is preferred to $PC_{60}BM$ for solar cell fabrication due to its stronger absorption in the visible; on the other hand, due to the similarity of the two fullerenes, their electronic structure is almost identical, so that our DFT calculations hold for both $PC_{60}BM$ and $PC_{70}BM$[†]. In this first part of our study, we thus conclude that large diameter s-SWCNT in combination with PCBM cannot provide PV conversion, while an efficient carbon based solar cell can be prepared using a two-phase active layer of $PC_{60}BM$ (or $PC_{70}BM$) and s-SWCNT with $d \approx 0.75–1.2$ nm.

However, practical realization of active layers using small diameter s-SWCNT is highly challenging: the high van der Waals attractive force between small-diameter nanotubes causes extensive nanotube bundling and poor overall morphology, and at first our collaborators were only able to achieve devices with a maximum efficiency of ~0.4 % using either $PC_{60}BM$ or $PC_{70}BM$ in combination with small-diameter nanotubes (see ref.[57]). On the other hand, a much smoother active layer morphology was observed for nanotubes of larger diameter d>1.2 nm blended with PCBM, although as mentioned before these blends are unsuitable for PV operation due to type-I alignment. In order to take advantage of the favorable morphology of this blend, we introduce reduced graphene oxide (rGO)[61] as a third material phase that can induce exciton dissociation at the interface with PCBM or s-SWCNT. Using DFT calculations of the PCBM/rGO interface detailed in ref.[57], we predict the formation of a large (> 1 eV) electron Schottky barrier at this interface, and thus predict the possibility to dissociate excitons generated on PCBM at the interface with rGO. Our collaborators confirmed experimentally that this three-phase combination of PCBM/rGO/s-SWCNT with $d > 1.2$ nm can simultaneously achieve favorable morphology and exciton dissociation, and constitutes the active layer material of our best-efficiency device, as discussed next.

Figure 3.4a shows a schematic drawing of the carbon-based solar cells fabricated by our collaborators based on our calculations, which achieve a maximum efficiency of 1.3%. The active layer is entirely deposited from solution and is composed of s-SWCNT, the fullerene derivative $PC_{70}BM$, and rGO[61], forming a BHJ morphology made entirely of carbon nanomaterials. Optimized carrier extraction is achieved using hole transport and exciton blocking layers in conjunction with transparent indium tin oxide (ITO) and Al contacts. The active layer does not contain other constituents such as conjugated polymers or small molecules, and the atomic

[†]We study the case of $PC_{60}BM$ for convenience: due to its higher symmetry, the interfaces with s-SWCNT can be more straightforwardly defined.

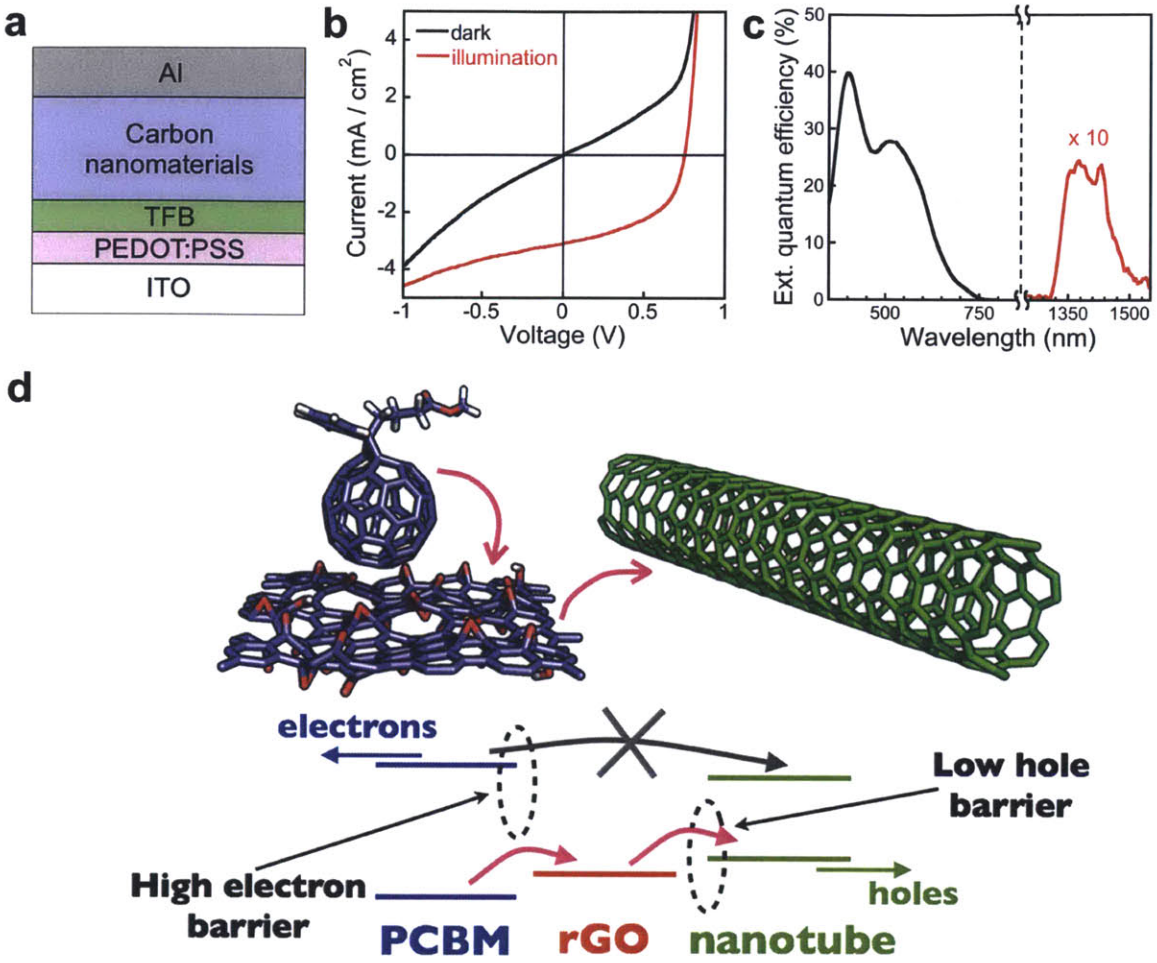

Figure 3.4: **1.3 % efficient carbon based solar cells. a,** Structure of carbon solar cells prepared in our work in ref.[57]. Al is the top contact,TFB and PEDOT:PSS are respectively an exciton-blocking and a hole-conducting layer deposited on top of the ITO bottom contact. For the best-efficiency device, the active layer, denoted by "carbon nanomaterials", contains a blend of rGO, $PC_{70}BM$, and s-SWCNT with a diameter of 1.2−1.7 nm. **b,** Current-voltage curves in the dark and under simulated sunlight illumination (1 Sun, AM1.5G spectrum) of the best-efficiency device studied in our work. **c,** EQE of the best-efficiency device, showing contributions from the $PC_{70}BM$ at visible wavelengths (black curve), and from the nanotube S_{11} optical transitions centered at 1400 nm in the infrared (red line, multiplied by 10 for clarity). **d,** Interface of PCBM/rGO sheet/s-SWCNT, representing schematically the active layer components of the best-efficiency device. The pink arrows trace the transfer cascade of hole carriers photogenerated within PCBM, selectively injected to rGO due to a large Schottky barrier for electrons, and then transferred to s-SWCNT. The schematic band diagram below shows the same process together with the HOMO and LUMO energies for PCBM and carbon nanotubes, and the Fermi energy of rGO (shown in red). The crossed gray arrow indicates the absence of electron flow from PCBM to rGO and s-SWCNT.

carbon concentration in the active layer is as high as 80−90 at. %, in contrast with carbon concentrations of 40−50 at. % for typical solar cells based on P3HT/PCBM. The best-efficiency device fabricated using these carbon nanomaterials has a composition of $PC_{70}BM$ (95 wt %) / rGO (2 wt %) / s-SWCNT (3 wt %, $d > 1.2$ nm); it achieves an efficiency of 1.3 %, deriving from a short-circuit current $J_{sc} = 3.1$ mA/cm^2, an open circuit voltage $V_{oc} = 0.75$ V, and a fill factor $FF = 0.55$ (Figure 3.4b). For comparison, a control sample constituted only by $PC_{70}BM$/rGO without nanotubes showed an efficiency of 0.009%, more than two orders of magnitude lower. This indicates the key role of s-SWCNT as a hole transport material as well as infrared absorber. The external quantum efficiency (EQE, Figure 3.4c) shows contributions from both the s-SWCNT donor and the $PC_{70}BM$ acceptor. The EQE in the visible derives from optical transitions in the $PC_{70}BM$, with a main peak at ~400 nm and a shoulder at 550 nm. The EQE peak in the infrared centered at 1400 nm is due to the S_{11} optical transitions in s-SWCNT with 1.2−1.7 nm diameter[53], as found in our previous work using the same nanotubes in a polymer-based device (see above). The PV operating mechanism involves a photogenerated hole carrier cascade from $PC_{70}BM$ to rGO and then to s-SWCNT (Figure 3.4d), as predicted using DFT. A large set of devices was prepared using different carbon nanomaterial combinations beyond the optimal one shown here (see ref.[57] for details).

Next, we discuss the photodegradation (PD) behavior of our carbon based solar cells. PD is an open technological problem in polymer based PV, requiring tight encapsulation and leading to device failure. Recent studies have significantly contributed to the understanding of PD patterns in polymer/PCBM solar cells, by showing the presence of a burn-in process leading to the rapid initial degradation of encapsulated devices due to the formation of intra-gap trap states[19]. In Figure 3.5a we compare the PD of the PCBM/rGO/s-SWCNT carbon solar cell with best efficiency prepared in our work, with that of a polymer based P3HT/PCBM device prepared and tested at the same time, under natural illumination and exposed to ambient environment without encapsulation. The P3HT/PCBM device shows a burn-in process leading to a rapid efficiency drop in the first 100 h, while the carbon based device shows a gradual efficiency decrease without burn-in, contributed in equal measure from a decrease in J_{sc} and V_{oc} (see ref.[57]). After aging both devices for 500 h, the efficiency of the polymer based device reduces to ~15 % of the initial value versus a much lower reduction to ~50 % of the initial value for the carbon based solar cell. The fact that the burn-in process only appears in devices where the polymer is present is in agreement with the findings in ref.[19] that attribute the rapid initial efficiency decrease to the presence of the polymer. If oxygen and moisture are eliminated by carrying out the same aging test in a nitrogen glove box (Figure 3.5a), the efficiency only decreases by 5−10 % over 500 h for the carbon based solar cell (both with and without rGO), while a decrease by as much as 50 % is observed for the polymer based device. The significantly lower PD rate for carbon based devices in a nitrogen environment compared to air suggests that oxidative processes due to the presence of PCBM are responsible for the PD in air seen in Figure 3.5a, consistent with recent PD studies of PCBM[62]. The residual PD for the polymer

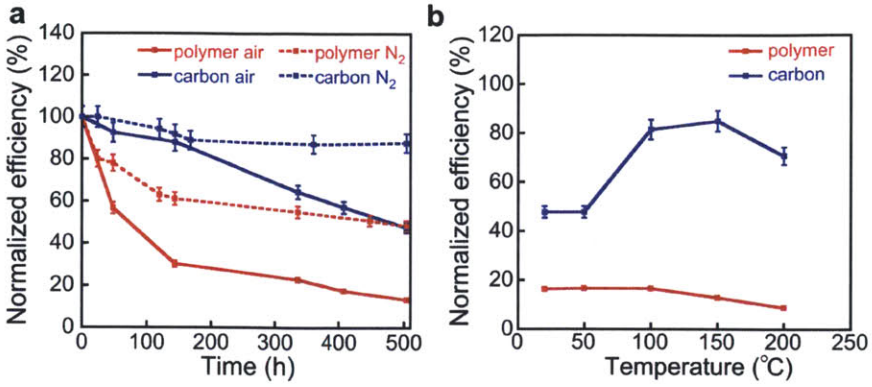

Figure 3.5: **Photodegradation in carbon based solar cells. a,** Aging in air and in nitrogen of non-encapsulated solar cells, quantified by the time evolution of the percent fraction of the initial efficiency for the given device. A P3HT polymer/PCBM solar cell (referred to as "polymer" in figure) is compared with a PCBM/rGO/s-SWCNT solar cell ("carbon" curves in figure). A standard deviation of ~5 % is shown for all the efficiency values reported here, based on a statistical sample of ~10 devices tested under the same conditions for each case. **b,** Thermal annealing at different temperatures of devices previously aged in air for 500 h. An optimal annealing temperature of 150 C allows a partial reversal of the photodegradation of carbon-based devices, by restoring the efficiency up to 85% of the initial value. The same reversibility is not observed in a polymer based device.

solar cell in nitrogen suggests on the other hand that polymer PD is partially contributed by optical excitation processes independent of the presence of oxygen. Finally, we show in Figure 3.5b an effect unique to the carbon based solar cells prepared here: upon thermal heating in vacuum for 10 min of a PCBM/rGO/s-SWCNT solar cell previously aged for 500 h in air, the efficiency can be restored to 85 % of its initial value if the proper temperature range is chosen for the annealing process, likely due to the partial reversibility of the PD oxidative processes. The same effect is not observed for a polymer based solar cell (Figure 3.5b).

Recently, we have focused on the role of rGO in stabilizing the solar cell. Our collaborators have shown that if the PEDOT:PSS buffer layer is replaced by rGO in solar cells with only small-diameter s-SWCNT and PCBM in the active layer, air-stable devices with negligible degradation for over 1,500 h can be achieved. We have further shown using a combination of *ab initio* molecular dynamics and DFT calculations that rGO is a promising buffer layer and contact material for carbon based PV (see ref.[63] for details). In particular, our calculations suggest that a variability of the workfunction in a 2.5 eV window can be achieved by fine-tuning the type and concentration of oxygen-containing functional groups attached to the graphene sheet in rGO[63]. These results encourage further research on rGO as a candidate material with wide applicability for contacts or interface layers in carbon based PV as well as other optoelectronic applications.

There is significant potential to increase the efficiency of carbon-based solar cells beyond the 1.3 % value reported here. The theoretical efficiency limit of such devices depends on the

absorption spectrum and energy gap of the materials present in the active layer, as well as on the maximum voltage achievable and on recombination. For the solar cells based on PCBM and s-SWCNT fabricated in this work, we estimate efficiency limits of 9 % and 13 %, respectively, for nanotube diameters of 1.2−1.7 nm and 0.75−1.2 nm, as derived in the analysis that follows. The main active layer constituent (~90 wt %) in our study is $PC_{60}BM$ (or $PC_{70}BM$), which contributes to most of the photocurrent and quantum efficiency as shown in Figure 3.4c. This also implies that absorption is limited to photons with energy above the optical gap of PCBM – apart from a small contribution from s-SWCNT absorption in the infrared, neglected here – and we can thus approximate the maximum short-circuit current J_{sc} as:

$$J_{sc} = e \int_{E_g}^{\infty} J_{ph}(E)\, dE$$

where E_g is the optical gap of PCBM (~1.8 eV), J_{ph} is the incident solar photon flux for the AM1.5G spectrum, E is the incident photon energy, and e the elementary charge. For the case of PCBM absorber, this yields an upper limit for J_{sc} of ~20 mA/cm^2 assuming and EQE of 100%; the contribution from the nanotubes, which may be sizeable, is neglected in this order-of-magnitude estimate. For an XSC with exciton dissociation occurring at a D-A heterojunction, the maximum V_{oc} can be approximated by the interface energy gap (see Chapter 1). For small values of ΔE_c, *e.g.* ~0.2 eV as found here, the maximum interface energy gap is approximately equal to the s-SWCNT optical gap, here taken as the average for the considered diameter range. This leads to a limit in V_{oc} values of approximately 1.0 V for nanotube diameters of 0.75−1.2 nm and 0.7 V for nanotube diameters of 1.2−1.7 nm, in agreement with the V_{oc} found in this work. A reasonable limit for FF can be taken as 0.65 as done in estimating PCE limits for polymer solar cells[25]; this is not far from the 0.55 value obtained in our best device. Finally, the maximum PCE η_{max} under AM1.5G illumination is calculated as the product $J_{sc} \cdot V_{oc} \cdot FF$, normalized by the incident power of 100 mW/cm^2 for AM1.5G illumination. Using the values reported above, we obtain η_{max} = 9 % for nanotubes with large diameter of 1.2−1.7 nm, and η_{max} = 13 % for nanotubes with small diameter of 0.75−1.2 nm. In comparing these limit values to the performance of the devices fabricated in this work, we note that V_{oc} is near-optimal despite the limited efforts in our work to optimize this parameter, while J_{sc} is 7−10 times lower than the limit value of ~20 mA/cm^2. The main challenges to significantly improve J_{sc} lie in the fabrication of thicker active layers than shown here (only ~100 nm) and the use of materials with higher purity to minimize recombination, as well as achieving optimal morphology using small-diameter nanotubes with potential to yield higher sunlight absorption, currents, and voltages. These observations together with the high limits predicted for s-SWCNT/PCBM solar cells have motivated further work on efficient carbon based solar cells devices.

Recently, our collaborator Dr. Shenqiang Ren has developed 5.6 % efficient PCBM/s-SWCNT solar cells, made using high-purity s-SWCNT with only 5 different chiralities and diameters smaller than 1.2 nm[64], as predicted in our DFT calculations in Figure 3.3. The presence of small diameter nanotubes allows one to eliminate rGO from the active layer, thus forming

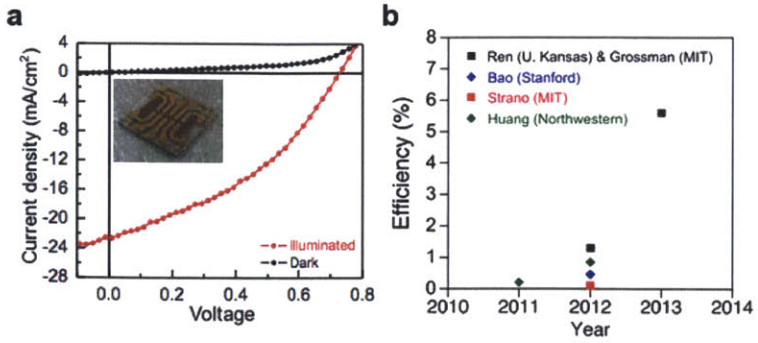

Figure 3.6: **Efficiency of carbon based solar cells.** **a,** Current-voltage measurement of a 5.6% efficient carbon based solar cell, also shown in the inset photo. **b,** Efficiency chart of carbon based solar cells.

an active layer with better control of the composition. Strict control of the morphology using solvent annealing enabled the preparation of smooth active layers without nanotube bundling. A current-voltage curve of a representative device with over 5 % efficiency is shown in Figure 3.6a, showing the achievement of large J_{sc} of order 20 mA/cm^2, close to the limits predicted from us prior to the preparation of these more recent high-efficiency devices. Other research groups have also been recently involved in developing efficient carbon based solar cells. In one of these works, C_{60} or C_{70} fullerenes were evaporated to form bilayer devices in combination with SWCNT to achieve efficiencies of less than 0.1 %[65]. Another group has employed a composite of SWCNT/rGO/fullerene deposited from aqueous solution[66,67], yielding efficiencies of 0.21 % for active layers based on C_{60}[66] and 0.85 % for devices employing C_{70}[67]. Recently, a 0.46 % efficient "all-carbon" solar cell in which the electrodes were also made entirely out of carbon has been reported by the Bao group[68]. Figure 3.6b summarizes the time evolution of the efficiency for carbon based solar cells, showing the name of the group leaders involved in the work as well as their institution. At the time of writing, the 5.6 % efficient devices prepared by our collaborators based on our DFT predictions are being certified by NREL; they may constitute the first point for carbon based solar cells in the NREL efficiency chart shown in Chapter 1.

In summary, our calculations have guided the design of carbon based solar cells with efficiencies of up to 5.6 %. Our results demonstrate that carbon based PV active layers free of conjugated polymers or small molecules constitute a promising novel direction for photostable, efficient, solution-processable, thin-film solar cells that are amenable to large-scale manufacturing. Candidate active layer materials are not limited to nanotubes and fullerenes as shown here, but rather span a vast array of suitable carbon compounds with yet untapped potential for thin-film solar cells. In combination with recently reported carbon based transparent electrodes, carbon PV active layers could enable in the near future the development of efficient "all carbon" solar cells[68]. We observe that the efficiency limits of 9−13 % predicted here for nanocarbon based PV are similar to those predicted for polymer-solar cells based on PCBM acceptors, where $\eta_{max} \approx 11$ % has been estimated and almost practically achieved after a decade

of intense research[5]. The main reason for this is that the optical gap of PCBM is similar to that of common polymer absorbers such as P3HT. However, the added benefit of using carbon is the superior photostability, indeed a key feature for widespread application of a solar cell technology. We believe that an optimization effort similar to that for polymer based solar cells should be undertaken for carbon based devices, by identifying high-mobility and high purity semiconducting carbon materials – both bulk and nanostructured allotropes – amenable to low-cost mass fabrication. Some possibilities of bulk carbon materials for thin-film PV are discussed briefly in the next section.

3.1.3 Beyond Nanocarbon: Amorphous Carbon and Coal

While carbon nanomaterials conveniently combine a host of appealing features for solar cells, they require precisely controlled structures to achieve the desired functionality within a PV device. For example, carbon nanotubes show diameter-dependent band alignment with PCBM fullerene as shown above, and individual nanotube chiralities may be necessary to optimize the efficiency of solar cells based on s-SWCNT and fullerenes. These requirements pose at present significant challenges to fabricate large quantities of the active layer carbon nanomaterials. Such a scenario motivates a search for bulk carbon materials possessing the same desirable features of carbon nanomaterials (namely, photostability, strong sunlight absorption, and potential for simple thin film fabrication) coupled to large-scale manufacturability and abundance in the Earth's crust. Within this family of materials, amorphous carbon (a-C) holds a particularly promising place owing to its presence in a large number of abundant compounds, including coal and shale rocks, and its ease of deposition in thin film form with control of the structure and chemistry[69]. As an amorphous material of the fourth group of the periodic table, a-C holds similarities to amorphous Si (a-Si)[69]. Due to its strong optical absorption and thin-film manufacturability, hydrogenated a-Si (a-Si:H) has been investigated extensively for PV applications, resulting in solar cells with up to ~10 % efficiency[2]; on the other hand, there is a surprising lack of information regarding the potential of a-C for solar cells. In spite of the presence of H atoms to passivate potentially detrimental dangling bonds, a-Si:H is affected by the so-called Staebler-Wronski (SW) photodegradation effect[69]. The concentration of defects and traps increases with light exposure in a-Si:H due to the SW effect, thus reducing the efficiency and significantly undermining the durability and technological potential of solar cells based on a-Si:H. In contrast, C atoms in a-C can bind in different configurations by forming threefold (sp^2) and fourfold (sp^3) coordination, thus allowing for dangling bonds to be partially passivated within the a-C framework even in the absence of hydrogen. For this reason, a-C does not display an equivalent of the SW effect of a-Si. In a-C, the sp^2 bonds chiefly control the electronic and optical properties[70], while the sp^3 bonds control the stability and mechanical properties[71]. Perhaps an even more critical issue in a-Si is the low value of hole mobilities dramatically limiting the achievement of high PCE in a-Si. The hole mobility in a-C has not been studied in detail to

date, and a-C may display much more favorable mobilities than a-Si.

In general, the complex network of C atoms with tunable sp^3/sp^2 ratio present in a-C is expected to impart a desirable tunabillity to the electronic, optical, and transport properties of relevance in solar cell devices, while the strong and flexible C−C bonding geometries are promising to achieve superior photostability. In PV, a-C has been employed only in combination with other materials to realize solar cells based on *p*-*n* junctions[72], *p*-type a-C/*n*-type silicon (*n*-Si) junctions[73], and Schottky junctions[74]. Theoretical modeling of a-C using first-principles calculations has focused on structural features for a fixed value of the density[75,76], while only recently diamond-like a-C has been investigated for solar energy applications[77]. We show here our recent results obtained in collaboration with Dr. Giancarlo Cicero and Francesca Risplendi correlating structural and optical properties of a-C and showing its promise for PV.

We combined *ab initio* molecular dynamics and DFT calculations to explore the electronic and optical properties of a large statistical set of a-C and hydrogenated a-C (a-C:H) structures, with densities in the range from 2.25 g/cm^3 to 3.5 g/cm^3 (with increments in steps of 0.25 g/cm^3), respectively the density values of sp^2 bonded graphene sp^3 bonded diamond, and H content in the 0−20 % range, with increments of 5 %. Each a-C structure consists of a cubic simulation cell with a total of 216 C atoms (Figure 3.7a), and in order to obtain meaningful statistical averages, we studied 10 samples for each density and H content. Briefly, we adopted the local density approximation (LDA) for the exchange-correlation energy functional, and PAW pseudopotentials[78] as implemented in the VASP code[36]. For the MD simulations, the Kohn-Sham states were expanded in plane waves with a kinetic energy cutoff of 350 eV, and the Brillouin zone was sampled at the Γ point. The same settings were employed to relax the final structures in DFT and to obtain the DOS. The optical absorption spectrum was obtained using up to 1,000 empty bands and the DFT-RPA approximation for the imaginary part of the dielectric matrix (see Chapter 2). The a-C preparation follows a multi-step protocol: using an in-house developed code, the atomic positions are initially randomized using the algorithm from Wooten, Winer and Weaire[79]. Once randomized, the a-C and a-C:H samples are annealed at 5,000 K for 3 ps using *ab initio* MD and subsequently cooled to 300 K over 0.3 ps, and further equilibrated for 3 ps. We have verified that our cooling rate was sufficiently slow by comparing with simulations with 10 times slower cooling rates for some selected cases. Following equilibration, all structures were relaxed within DFT to less than 10^{-4} eV/Å residual atomic forces.

Our results, detailed in ref.[80], correlate structural features such as the density, concentration of sp^2 and sp^3 hybridized C atoms, and H content to optical and electronic properties of interest in PV such as the density of states, Tauc and mobility gaps[81], and optical absorption. In our structures, the ratio of four-fold (sp^3) to three-fold (sp^2, or sp^3 with a dangling bond) coordinated C atoms decreases when the density is decreased from the diamond value of 3.5 g/cm^3 to the graphite value of ∼2.25 g/cm^3 (Figure 3.7a). In addition, hydrogenation of a-C increases the structural disorder and induces H atoms to saturate the π bonds, thus converting sp^2 C double

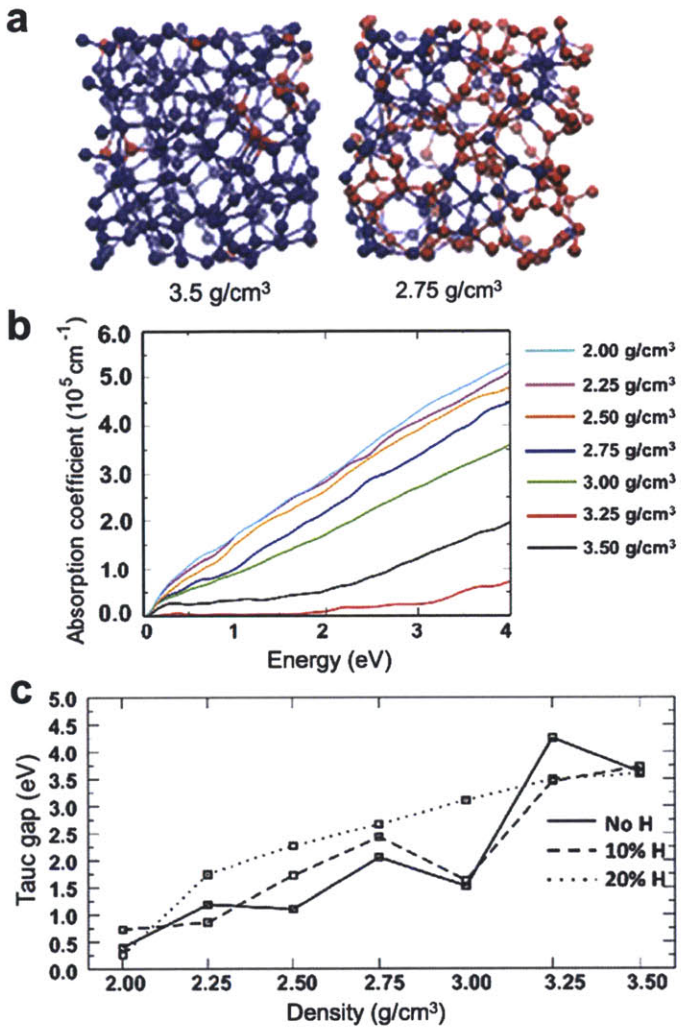

Figure 3.7: **Structure and properties of amorphous carbon. a,** Two a-C structures employed in this work, with different densities as shown in figure. The simulation cells contain 216 C atoms (without H) with four-fold coordination or three-fold coordination, shown respectively as blue and red spheres. The fraction of three-fold coordinated C atoms increases for decreasing densities. **b,** Absorption coefficient of a-C at different densities, computed for photon energies in the range useful for sunlight absorption. **c,** Tauc gaps as a function of density and H content.

bonds to two sp^3 C−H groups and consequently increasing the sp^3 fraction. As the density decreases from the 3.5 g/cm^3 value of diamond, the number of states with energy in the original gap of diamond increases, and the energy gap gets narrower until it closes completely when the defect tails touch, at a density $\rho \approx 3$ g/cm^3. The top of the valence band and the bottom of the conduction band are contributed chiefly by π states of sp^2 C atoms, forming weaker π bonds contributing to the tail states within the gap. This is consistent with the closure of the gap as the sp^2 fraction increases in the samples with lower densities. Additional structural details are discussed in ref.[80], while we focus here on the optical properties of a-C. Figure 3.7b shows the DFT-RPA optical absorption spectrum $\alpha(E)$ as a function of photon energy E

for a-C samples of different densities and without H. For each case, the absorption spectrum was obtained by averaging over ten simulations for each density. We observe relatively broad absorption spectra with large values of $\alpha \approx 10^5$ cm^{-1} at visible energies, comparable to the absorption in a-Si and the best organic and inorganic absorbers employed in PV, thus making a-C (and a-C:H) an excellent candidate for sunlight harvesting. In a-C and a-C:H, α is mainly determined by interband transitions, with strong contributions from π to π^* transitions for the energies of interest in sunlight absorption ($\sim$0.5$-$4 eV). Local disorder crucially impacts the optical properties as it determines the energy and localization of π and π^* states in a-C and a-C:H. For lower densities with a large fraction of sp^2 C atoms, the absorption is significant at low energy due to the presence of occupied and unoccupied states with energy within the mobility gap. By contrast, samples with higher densities show absorption onsets at higher energies, and can absorb light significantly only around 2.5$-$3 eV. These observations suggest the crucial role of π states for optical absorption in a-C, similar to optical transitions at visible energy in graphene and to HOMO$-$LUMO transitions in conjugated molecules and polymers. The a-C:H absorption spectra, reported in ref.[80], present a similar behavior with subtle differences related to the structural effect of H atoms. In particular, H atoms enhance absorption in samples with higher densities as they introduce disorder (and thus states close to the Fermi energy), and reduce absorption in samples with lower densities since H saturates double C$-$C bonds thus decreasing the sp^2 C atom content.

Figure 3.7c shows the Tauc optical gap E_t in samples of a-C as a function of density and H content, obtained from α by using a linear fitting of $(\alpha E)^{1/2}$ *vs* E. The Tauc gap of an amorphous material is a concept similar to the optical gap in a crystalline system, and marks the onset of substantial optical absorption in the material[81]. We observe that E_t increases as a function of density and H content, thus following similar trends to the mobility gap E_m (not shown) obtained by analyzing the localization of the electronic states in our samples[80]. This situation is ideal since $E_t \approx E_m$ guarantees that photogenerated electrons and holes possess the necessary mobility to accomplish PV operation rather than being trapped in localized states. Our results further suggest that by tuning the deposition process to obtain a-C with a specific density and H concentration, a set of possible PV device configurations can be realized. For example, a device consisting of a heterojunction of two stacked a-C layers with different H concentrations and densities may enable efficient carrier separation and PV operation. Alternatively, a-C could be used as a matrix for the dissolution of fullerenes or other carbon materials and form a BHJ active layer working with a mechanism similar to BHJ polymer/fullerene solar cells. We believe that such configurations possess the potential to offer enhanced photostability and charge carrier mobility compared to polymer based PV, while retaining similar advantages in terms of manufacturability. Research aimed at developing these two families of devices will require a deeper understanding of a-C and a-C:H as well as the study a-C heterojunctions and interface band alignments, together with a deeper understanding of transport and carrier recombination in a-C.

Further work of a-C is also important to understand the potential of more complex carbon phases containing large amounts of a-C, such as coal and shale rocks, both of which are highly abundant and inexpensive. While combustion is the main use of coal for electrical energy generation, given the new possibilities offered by materials design combustion is no longer the only means for carbon atoms to generate energy. PV conversion in a solar cell based on carbon as discussed in this chapter can efficiently deliver clean, renewable electricity.

A simple example is in order to compare the energetics and cost of carbon combustion versus sunlight conversion. Up to 350 kg of coal are needed to power a 100 W light bulb for one year when generating electricity from coal in a state-of-the-art coal plant with 30 % efficiency[82]. The same light bulb can also be powered using only 5 g of carbon, in the form of a 1 μm thick solar cell of 5 m^2 area, with an assumed 2 % efficiency. Not only is the amount of carbon employed 70,000 times smaller: the solar panels can further power the light bulb throughout their lifetime (for a Si solar cell, this amounts to ~20 years), and without any negative environmental impact. Our work on PV active layers based on carbon nanotubes, fullerenes, and other carbon nanomaterials shows that it is possible to prepare solar cells based exclusively on carbon with efficiencies of up to ~5 %, as well as to tune and control the bonding geometry and the optical and electronic properties in a-C. This scenario encourages the search for pathways to convert inexpensive coal into a useful material for PV using cheap low temperature processing, thus creating a new paradigm for solar energy generation from coal. It is our opinion that the carbonaceous materials in the coal, oil, and shale rock we are currently pumping out of the ground and burning, represent a unique opportunity for renewable energy, especially when viewed in the context of engineering functional properties in materials. Although a full cost analysis is necessary to establish the potential of carbon-based solar cells, the comparison provided above between combustion and PV as two possible ways to power a light bulb suggests dramatic cost and environmental advantages for renewable electricity generation from carbon based solar cells. Since the industrial revolution, human activity has modified the carbon cycle by changing its components functions and directly adding carbon to the geosphere and atmosphere, in ways defying careful prediction and analysis. Rich surprises await the future employment of carbon minerals as energy sources, including novel ways to use coal and carbon nanomaterials. While our present energy landscape is dominated by carbon combustion, sunlight conversion may be able to brighten a renewable future for carbon.

3.2 Two-Dimensional Monolayer Materials for Photovoltaics

The recent advent of two-dimensional monolayer materials with strong and tunable optical absorption and high carrier mobility offers renewed opportunities for efficient, ultrathin XSC alternative to those based on conjugated polymer and small molecule donors or quantum dots. Following the pioneering work from Geim and colleagues showing the mechanical exfoliation of graphene with the scotch tape method[83], monolayers of BN[84], hybrid graphene-BN[85], MoS_2[86,87], $MoSe_2$[88], and WS_2[89] have been prepared by mechanical or liquid phase exfoliation[90]

and chemical vapor deposition. While technical barriers continue to be overcome towards large-scale synthesis of monolayer materials, studies of micron scale flakes have already displayed a host of novel optical and electronic properties of relevance for PV. For example, two-dimensional monolayer materials are in general photostable, display extremely high optical absorption at visible energies considering their Angstrom scale thickness, as well as high carrier mobilities of over 200,000 $cm^2/V{\cdot}s$ for suspended graphene[91], and up to 200 $cm^2/V{\cdot}s$ in MoS_2[86] and 20 $cm^2/V{\cdot}s$ in hybrid graphene-BN monolayers[85]. Such high mobilities coupled to the possibility of making ultrathin solar cell active layers can lead to monolayer based PV devices with very low series resistance, large voltages, and near-optimal I-V curves. Some monolayers are (semi)metallic, like graphene, and are thus only suitable to form Schottky barrier solar cells; some others, like transition metal dichalcogenides, are semiconducting with energy gaps in the ideal range of 1.5−2.5 eV for PV operation. Despite these encouraging properties, the study of monolayer materials for solar energy absorption and conversion using PV (or photoelectrochemical) cells is still in its infancy. In the remainder of this chapter, we discuss our recent research on two families of semiconducting monolayer systems for application in PV: 1) Hybrid graphene-BN monolayers, for which we characterize the electronic structure, optical properties, and potential for PV, and 2) Monolayer transition metal dichalcogenides such as MoS_2, $MoSe_2$, and WS_2, for which we study sunlight absorption and PV devices with a thickness of just a few Angstroms.

3.2.1 Graphene-Boron Nitride Hybrid Monolayers

Monolayers of hybridized carbon and boron nitride (CBN) present highly appealing optical and electronic properties due to their tunable optical gap, physically deriving from the large band gap difference between pure hexagonal BN (h-BN, energy gap $E_g > 5.0$ eV) and graphene, a semimetal with zero energy gap[91]. The C and BN phases are immiscible in 2D, leading to phase separation in the sheet with formation of distinct C and BN domains[85]. The optical absorption spectrum of CBN measured in the recent work from Li *et al.*[85] shows two main absorption edges located (using Tauc's extrapolation procedure[81]) at around 1.6 eV and 4.5 eV for a sample with 65 % C content. For higher C concentrations, both absorption peaks were found to shift to lower energies. These two features were attributed to the existence of C and h-BN domains large enough to resume their individual band gap identities, rather than behave as a CBN alloy. The electronic band gap of the CBN monolayer has been calculated for different C and BN domain geometries including quantum dot and superlattices that approximate the experimental structure, using tight-binding and DFT calculations[92,93,94,95,96,97,98]. For quantum dot geometries, the band gap tunability arises due to confinement in both dimensions[95], but DFT level calculations were only applied to limited domain sizes up to ∼1 nm, well below the experimental value. CBN two-dimensional (2D) superlattices can provide band gap values closer to the experimental regime due to lack of confinement in one of the two in-plane dimensions. However, the results appeared in the literature up to now have addressed the band gap

tunability as a function of *composition*[93] rather than C domain size, and without attempting to interpret the experimental optical absorption spectrum in ref.[85] and its connection to the calculated bandstructure.

We discuss here our recent work (detailed in ref.[99]) in which we shed light on the optical and electronic properties of CBN monolayers and show that the double optical peak measured in[85] is inherently related to the bandstructure of the CBN system, regardless of the composition and domain size. Such excitation peaks are not due to large C and BN domains, but rather to the near-absence of mixing of C and BN states at the valence band maximum (VBM) and conduction band minimum (CBM), generating two distinct sets of optical transitions: low energy transitions between C states near the band gap resulting in bound bright excitons localized within the C domains, and higher energy transitions from states that are mostly BN-like in character and lie deeper within the conduction and valence bands. We further demonstrate that composition is not the main variable regulating the CBN electronic structure, band gap and optical absorption, in contrast with the well-known behavior of bulk semiconductor alloys whose energy gap varies continuously with the concentration of the composing elements[100]. We also find large corrections to the DFT band gap using GW calculations and strongly bound excitons, both effects contributing to an optical absorption spectrum similar to the DFT-RPA spectrum due to large error compensations in the latter. All these feature are relevant for tuning the properties of nanoscale solar cells, as discussed later in this section.

We carried out *ab-initio* DFT calculations using the QUANTUM ESPRESSO code[35] separately on CBN superlattices with armchair and zig-zag edges. An orthorhombic unit cell was adopted for the armchair structure and a hexagonal unit cell was used for the zig-zag case (Figure 3.8). A vacuum spacing of 15 Å was used in the direction perpendicular to the sheet to avoid spurious interaction with the image system. We employed a total number of 8 or 16 C and BN atom rows in the unit cell (Figure 3.8) in distinct sets of calculations. In this way, electronic structure data are available for a given composition for two different values of C domain sizes. The PBE exchange-correlation functional[59] is adopted and ultrasoft psuedopotentials[60] are used to describe the core electrons. A kinetic energy cutoff of 35 Ry was used for the plane-wave basis set and of 200 Ry for the charge density. Converged Monkhorst-Pack $\vec{k}$-grids[101] of $3 \times 3 \times 1$ and $15 \times 5 \times 1$ were used for the zig-zag and armchair cases, respectively. The GW and BSE calculations[28] were performed only on three armchair cases [†] with different C concentrations using the Yambo code[37] [‡]. Briefly, a plasmon-pole model was adopted for the self-energy and cutoff

[†]We calculated the formation energy of the armchair and zig-zag type edges and inferred a ratio of 2.5 between the thermal equilibrium length of the armchair and zig-zag domain edges at intermediate compositions and room temperature. This justifies our more accurate study of the optical properties and band gap for the armchair edge type as it is expected to contribute more significantly to the experimental results observed in[85]

[‡]For the calculations performed with the Yambo code, the ground state Kohn-Sham wavefunctions and eigenvalues were obtained using an LDA exchange-correlation functional (*Phys. Rev. B* **23,** 5048, 1981) with Troullier-Martins norm-conserving pseudopotentials (*Phys. Rev. B* **43,** 1993, 1991) as implemented in the QUANTUM ESPRESSO code. A kinetic energy cutoff of 55 Ry was used for the wavefunction. These calculations yielded

energies of 35 Ry and 5 Ry were used, respectively, for the exchange and correlation part of the self-energy; the Coulomb interaction was truncated in the direction perpendicular to the sheet to avoid spurious interaction with the image system. The GW calculations were performed without self-consistency in the Green's function and the screened Coulomb interaction using the G_0W_0 approximation scheme. A total number of 300 bands (> 150 empty bands) was used, together with a converged $\vec{k}$-point grid of $16 \times 6 \times 1$. Both DFT and GW levels of theory were employed in combination with RPA or BSE calculations to compute the optical absorption spectra.

Figure 3.8a shows the evolution of the DFT band gap as a function of C concentration for armchair superlattices with a simulation cell constituted by a total of 8 and 16 atom rows. For a given composition, the two cases with different number of atom rows give different band gap values; a same band gap value for the two systems is found when comparing superlattices with a same number of C rows (and thus a same C domain size). For example, the arrows in Figure 3.8a point at structures with three C rows, corresponding to different concentrations for systems with a total of 8 and 16 rows in the unit cell, and yet showing a same energy gap to within 0.1 eV. This behavior is observed for all such pairs of structures with a same number of C rows. A similar trend is found for the zig-zag case (Figure 3.8a) where systems with a given number of C rows, but corresponding to different C concentrations, show a same energy gap to within 0.1 eV. As observed in previous work[92], the addition of a single C row causes a drop in the band gap from 4.6 eV for pure h-BN to < 2.0 eV within DFT calculations.

A more detailed analysis of the DFT electronic structure is presented in Figure 3.9, where the CBN systems are labelled as $C_x(BN)_{(8-x)}$ for superlattices with x carbon rows out of a total of 8 rows. A direct band gap was found for all the armchair and zig-zag systems studied, thus justifying the high optical absorption observed experimentally. In the armchair cases shown here, the band gap closes progressively for increasing C concentrations but the formation of the Dirac cone only occurs when 1–2 residual BN rows are present, as seen by the increasing dispersion in the Y–Γ direction (normal to the domain edge) resulting in the closure of the gap at the equivalent of the K point of the hexagonal lattice [†] . We interpret this behavior as a sign of the incipient delocalization of the VBM and CBM states when the system is close to being a sheet of pure graphene. The PDOS shows that for all the compositions studied the states with energy near the gap are mainly due to C, while states farther in energy from the gap result from a clear hybridization of C and BN states. The zig-zag case shows analogous behavior (see ref.[99]), with subtle differences in the band gap closing near the pure C composition. The dependence of the band gap on the C domain size, rather than on the overall CBN layer composition, can be regarded as an electronic confinement effect, whereby the C states near the band gap are

identical results to the ones using the PBE exchange-correlation functional with ultrasoft pseudopotentials, and were carried out with the only scope of obtaining an input compatible with the Yambo code.

[†]See ref.[93] for the nomenclature of the Brillouin zone for the orthorhombic cell used here. The K point of the hexagonal lattice, where the graphene band gap is expected to close at high C concentration, falls between the Γ and Y point within this scheme.

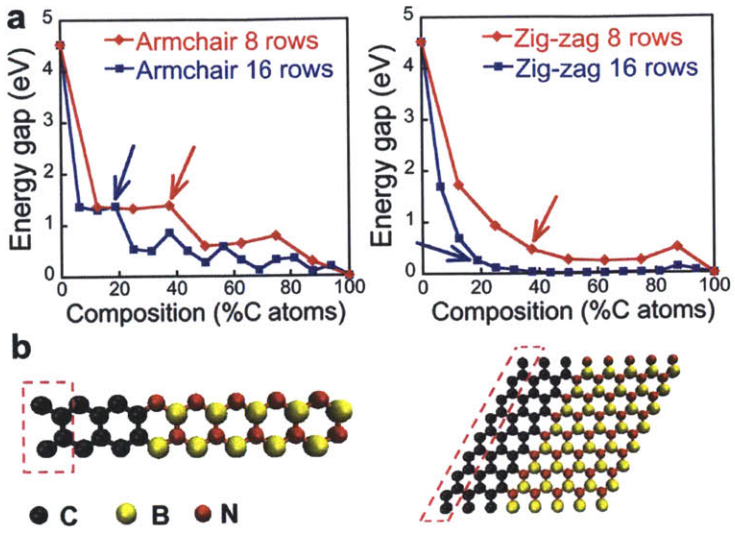

Figure 3.8: **DFT band gaps of CBN superlattices. a,** Kohn-Sham band gap calculated using DFT for CBN superlattices with armchair (left) and zig-zag (right) edge. Starting from pure BN (zero %C), each consecutive point for increasing C concentrations corresponds to the addition of a C row to the structure. **b,** Unit cells employed in the 8-rows calculations for the armchair (left) and zig-zag (right) cases. The parts referred to as "one row" in the text are shown in dashed boxes, and have a width of approximately 0.25 nm.

confined by an effective quasiparticle barrier within the conduction and valence bands formed by the BN states, as seen by the analysis of the PDOS. Nevertheless, the detail of the edge type and binding at the C-BN interface is also relevant to determine the specific value of the gap (and consequently of the optical properties), as shown by the different band gap values for the zig-zag and armchair cases.

Next, we analyze the results from the GW-BSE calculations. For the three armchair cases studied with beyond-DFT methods, we found quasiparticle (GW) band gap values significantly higher than the DFT gap (Table 1), with corrections in the range of 0.8−1.8 eV. On the other hand, the optical (GW-BSE) gap values were found to be within 0.4 eV of the DFT gaps due to large exciton binding energies of 0.7−1.5 eV (Table 1), inferred from the difference between the quasiparticle (GW) and optical (GW-BSE) gaps. The DFT-RPA absorption spectra for the

Table 1: Values of the band gap (in eV) within different approximations for three armchair structures studied with the GW and BSE methods. The exciton binding energy (in eV) is also shown.

Structure	DFT	GW	GW+BSE	Exciton b. e.
$C_1(BN)_7$ (12.5% C)	1.39	3.25	1.80	1.45
$C_4(BN)_4$ (50% C)	0.60	1.72	0.59	1.04
$C_7(BN)_1$ (87.5% C)	0.30	1.04	0.32	0.72

armchair (Figure 3.10a) and zig-zag (ref.[99]) cases show two absorption peaks resulting from the

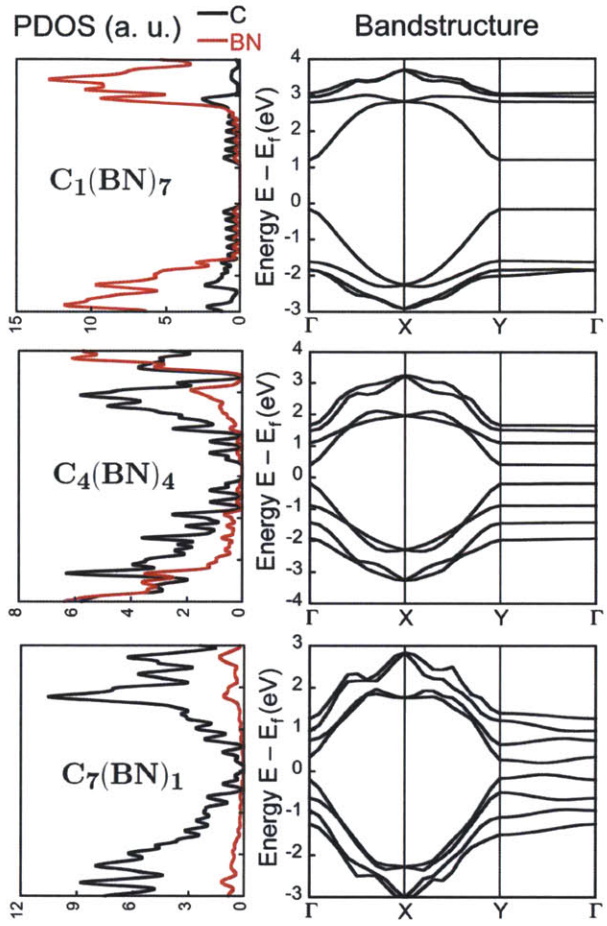

Figure 3.9: **Bandstructure of CBN superlattices.** PDOS and corresponding bandstructure plots for three armchair superlattices. The energies are referenced to the Fermi energy. The C domain size increases from the top to the bottom panel, and the band gap decreases accordingly. The Dirac cone typical of graphene starts forming for 1−2 residual BN rows, as seen in the bottom panel for the $C_7(BN)_1$ case, where the dispersion along the Y−Γ line culminates in the formation of the Dirac cone. The PDOS shows that the states close in energy to the gap are mainly due to mixing of C valence states with almost no contribution from BN.

DFT bandstructures in Figure 3.9, with transitions due to the direct band gap along the Y−Γ direction (low energy absorption onset) and to the direct gap from higher energy states formed at the X point. These two features are retained in the GW-BSE spectrum (Figure 3.10b) and can ultimately be indicated as the reason for the two absorption peaks observed experimentally in ref.[85] Nevertheless, the GW-BSE spectrum contains information about two important physical effects: the opening of the quasiparticle gap due to electron-electron interaction at the GW level of theory, causing by itself an almost rigid blue-shift of the absorption spectrum (GW-RPA curve in Figure 3.10b), and the formation of strongly bound excitonic states resulting in a red-shift of the spectrum back to energies similar to the DFT-RPA approximation level, as seen in the GW-BSE spectra in Figure 3.10b. This explains the excellent qualitative agreement of the DFT-RPA optical absorption spectrum seen in Figure 3.10b, due to a compensation of large errors within DFT.

Consistent with the experiments in[85], for increasing C concentrations both absorption peaks are red-shifted and their relative intensity varies, thus showing the tunability of the optical properties of the CBN sheet. By comparing with ref.[85] where systems with over 65 % C concentration show an optical gap of 1.5 eV, we infer that such a low energy absorption edge arises from small C domains with at least one dimension of 1−2 nm. However, we note that the Tauc's extrapolation procedure[81] used in ref.[85] can lead to significant errors in the estimation of the absorption onset, and suggest that the experimental spectrum should be regarded as formed by the superposition of the spectra shown in Figure 3.10 weighed for the different C domain sizes present in the system, a fact justified by the absence of a well-defined low energy peak in the experimental absorption data[85]. The exciton wavefunction obtained within the BSE framework (Figure 3.10c) is found to be confined by an effective quasiparticle gap at the CBN interfaces: when the hole is fixed in a given position within the C domain, the electron wavefunction localizes within the same C domain, compatible with the presence of VBM and CBM states with C character, and BN-like states farther in energy from the gap. Such delocalized, yet strongly bound excitons are a unique feature of nanoscale systems that has been predicted previously for 1D armchair graphene nanoribbons[102]; we believe that this feature may be typical of excitons in other monolayer systems.

In summary, we elucidate the mechanisms underlying the band gap formation and optical processes including absorption and excitons in the CBN monolayer. We find that the energy gap is uniquely regulated by the size of the C domains regardless of the overall system composition, a novel mechanism in clear contrast with the behavior of bulk semiconductor alloys. The absorption spectra of CBN monolayers show two main absorption peaks whose strength and position depend on the C domain size, with transitions between the VBM and CBM states contributing to the low energy absorption onset and to the formation of strongly bound excitons within the C domains. Large quasiparticle and excitonic corrections show that DFT calculations are inadequate to predict the experimental behavior of monolayer CBN alloys. The unique dependence of the band gap and absorption spectrum on domain size rather than concentration opens new

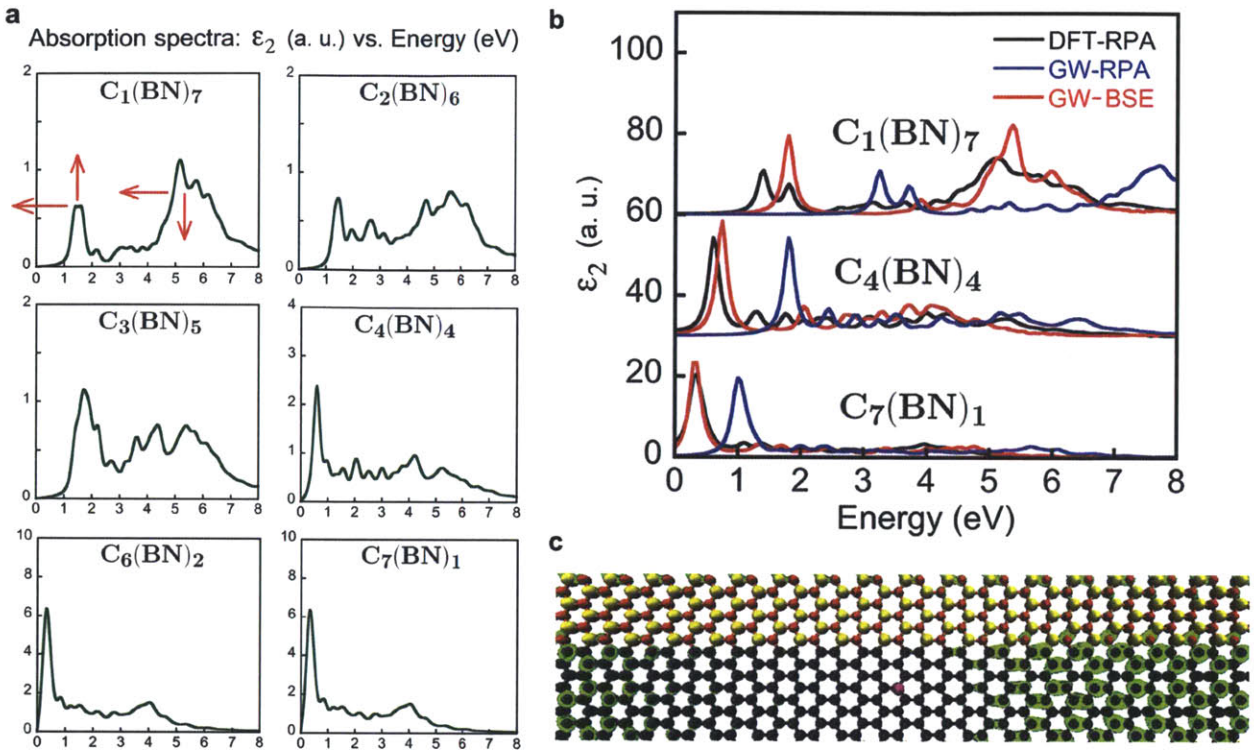

Figure 3.10: **Optical properties of CBN monolayers.** **a,** Evolution of the DFT-RPA optical absorption (expressed as the imaginary part of the dielectric tensor, ϵ_2) for increasing C domain sizes, for the armchair structures with 8 atom rows shown in Figure 3.8a. The two absorption peaks redshift and vary their relative strength for an increasing C domain size as indicated by the red arrows. **b,** Comparison of absorption spectra for the armchair structures discussed in Table 1. The imaginary part of the dielectric tensor (averaged for the three directions) is shown for different levels of approximation including DFT-RPA, GW-RPA and GW-BSE. **c,** Exciton spatial distribution (shown in green) for the $C_4(BN)_4$ armchair superlattice when the hole is fixed in the position represented by the magenta spot in the C domain. The atoms coloring follows the legend in Figure 3.8b.

possibilities for band gap engineering and in general for optoelectronic and PV applications distinct from those existing for *h*-BN and graphene. In particular, our work shows that quantum confinement by formation of nanometer size domains within a two-dimensional monolayer can be achieved similarly to the case of bulk systems. This novel mechanism to tune the optical gap, VBM and CBM energies, and exciton binding energy is extremely relevant in PV, since tailoring the band offsets at a D-A heterojunctions is a well-known pathway to optimize voltages and currents in XSC, as discussed in Chapter 1.

In what follows, we discuss how CBN monolayers can be employed in CBN/PCBM, CBN/s-SWCNT, and CBN/CBN heterojunctions for novel nanoscale PV. This work, reported here concisely, is discussed in full detail in ref.[103] In polymer/PCBM devices, the polymer donor dominates (and limits) the key physical processes in the solar cell, including optical absorption and transport of excitons and charge carriers. Exciton diffusion lengths of 5−10 nm prevent

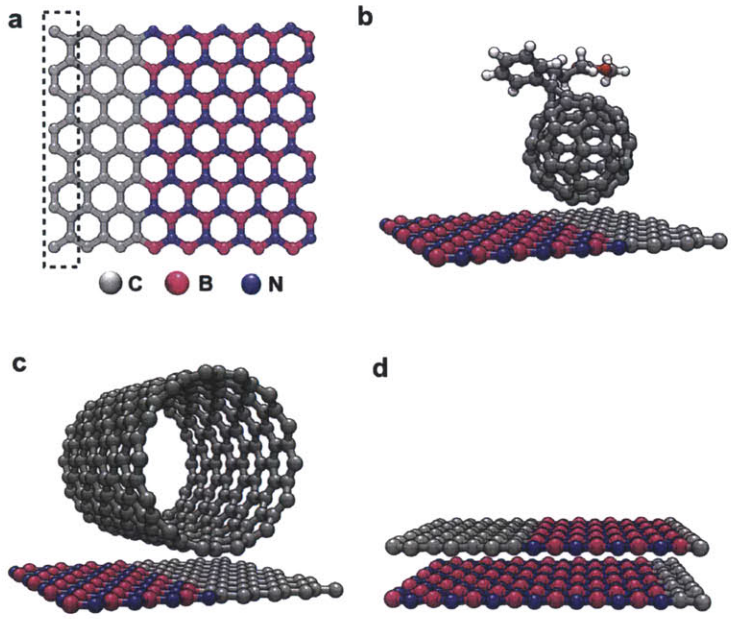

Figure 3.11: **CBN heterojunctions for nanoscale solar cells. a,** CBN monolayer unit cell used in our DFT calculations, with an armchair edge between the C and BN domains. Shown in the dashed box is a C atom row, with an approximate width of 0.25 nm. Following the nomenclature used here, the unit cell shown is $C_3(BN)_5$. Panels **b**–**d** show interfaces between a CBN monolayer and **b** PCBM fullerene, **c** a (14,0) zig-zag s-SWCNT, and **d** another CBN layer with different composition.

the use of bilayer devices, and mobilities much lower than 1 cm^2/Vs limit the thickness of bulk heterojunction devices to less than the absorption depth (typically $0.1 - 1\mu m$), thus limiting the output current. As discussed in Chapter 1, tuning the VBM and CBM levels of conjugated polymers is a challenging task, requiring trial and error chemical synthesis of a large number of compounds; band gaps of less than 1.5 eV are hard to achieve, and thus a large fraction of incident solar energy cannot be absorbed. First, we study here whether CBN monolayers can act as the donor at CBN/PCBM and other interfaces and thus replace the polymer with a material with much higher carrier mobility and a band gap tunable by quantum confinement as discussed above.

We form interfaces containing armchair CBN sheets (Figure 3.11a–d) by placing PCBM, or s-SWCNT of chirality (10,0), (14,0), and (16,0), or a second CBN layer at a van der Waals distance of 3.3 Å from a given CBN monolayer. In CBN bilayer calculations, the unit cell consists of two $C_x(BN)_{(8-x)}$ layers with AB stacking in the BN domains (B atoms on top of N atoms). We compute the electronic structure of such CBN interfaces by means of *ab initio* DFT calculations with a similar methodology as the one discussed above for CBN monolayers (see also ref.[103]). The DFT band offsets are estimated in all cases as differences in the peaks of the PDOS for the two structures constituting the interface. While this approach is usually reliable for the estimate of valence band offsets[31], as previously mentioned the accuracy of conduction band offsets depends on a compensation of errors on the DFT band gap of the two materials

constituting the interface. Hence for the case of CBN/PCBM interfaces, we choose to compute band offsets with higher accuracy at the GW and GW-BSE levels of theory, justified by the interest in estimating the efficiency of solar cells based on CBN/PCBM, a quantity rather sensitive to errors in the optical gaps and interface band offsets. On the other hand, for the CBN/s-SWCNT and CBN bilayers our analysis is based solely on DFT results, and is mainly aimed at determining qualitatively the possibility of forming type-II interfaces involving CBN monolayers.

Figure 3.12a shows DFT valence band offsets (ΔE_v) and conduction band offsets (ΔE_c)

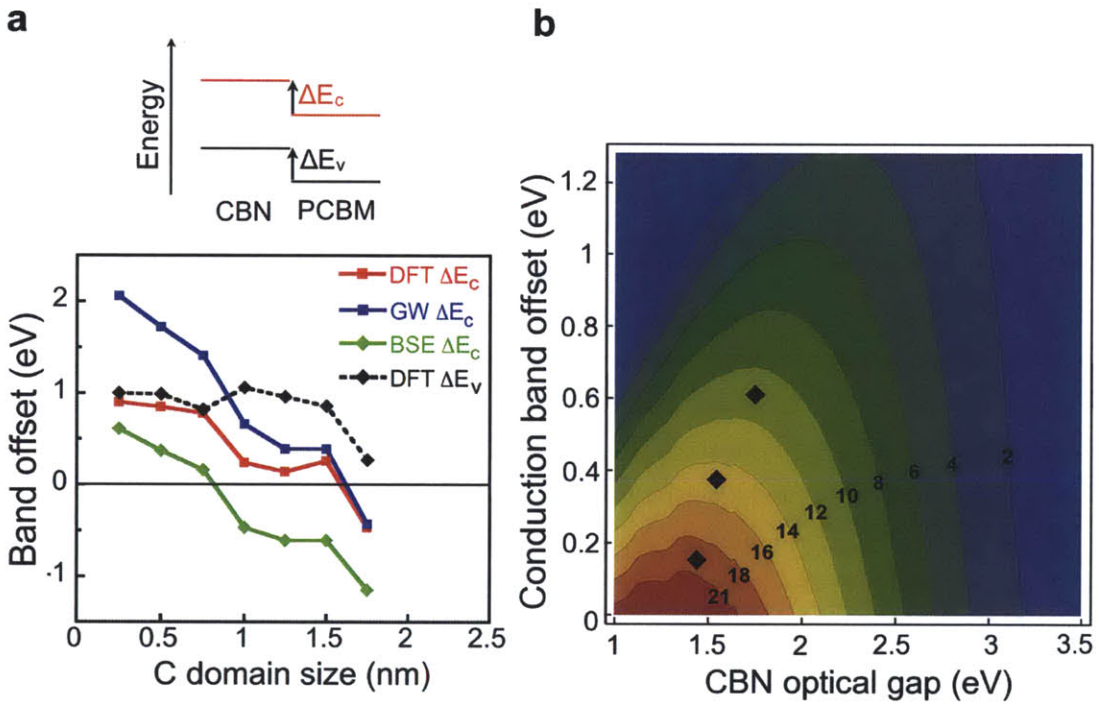

Figure 3.12: Band offsets and maximum efficiencies of CBN/PCBM active layers. a, DFT valence band offset (ΔE_v, dashed curve) and DFT, GW and BSE conduction band offsets (ΔE_c, solid curves) between $C_x(BN)_{(8-x)}$ monolayers and PCBM fullerene, expressed as a function of the C domain size in the CBN layer. ΔE_v and ΔE_c are referenced, respectively, to the valence and conduction band edges of the acceptor, as shown schematically above the plot. Within our model, ΔE_v is the same at all levels of theory since the GW corrections were applied as a rigid shift of the LUMO levels[103]. The number x of C atom rows in the CBN superlattice structure increases by one unit (from 1 to 7) at each consecutive point in the plot, and for each added row the C lateral domain size increases by 0.25 nm. The alignment is consistently found to be type-II for C domain sizes of up to approximately 1−2 nm depending on the level of theory used. **b,** PCE contour plot as a function of the CBN donor optical gap and conduction band offset ΔE_c. Constant efficiency level curves up to 21 % are shown in figure. The diamonds represent the efficiency limits of the three CBN/PCBM combinations yielding type-II alignment in the BSE curve in **a**. Efficiency values in the 10−20 % range are predicted depending on the C domain size.

at different levels of theory for interfaces between PCBM and $C_x(BN)_{(8-x)}$ monolayers with

different C domain sizes. Each consecutive point represents the addition of one C atom row and the removal of one BN row in the unit cell (Figure 3.11a), leading to a 0.25 nm increase of the C domain size. The DFT band alignment is found to be type-II for C domain sizes of up to 1.5 nm, with the PCBM acting as the acceptor at the interface, as seen by the positive values of ΔE_v and ΔE_c using the convention shown in Figure 3.12a. The trends in ΔE_v and ΔE_c show that the HOMO and LUMO energies of the donor can be tuned according to the C domain size, yielding unique control over the interface band offsets. This results in a tunable PCE, as explained below. To confirm the type-II alignment found within DFT, we apply GW corrections separately to the LUMO levels of CBN and PCBM (see ref.[103]). The GW corrected ΔE_c values, shown in Figure 3.12a (GW curve) yield the same qualitative trends as the DFT results, with type-II alignment for C domain sizes of up to 1.5 nm. Assuming that CBN is the main absorber in the solar cell, the exciton binding energy in the CBN layer is a key quantity to determine the energetics of photoexcited electron transfer to PCBM. To address this point, we calculate ΔE_c values as differences between the optical LUMO level of the CBN donor (using GW-BSE, and thus accounting for exciton binding energy) and the GW LUMO level of the PCBM acceptor; ΔE_c as defined here is thus equivalent to the effective conduction band offset γ introduced in Chapter 1. The *combined scheme* adopted here utilizing the optical LUMO of the donor and the quasiparticle LUMO of the acceptor takes into account the minimum energy of the exciton formed after photoabsorption in the CBN donor, as well as the electronic quasiparticle level for the transfer of a photoexcited electron to the acceptor. Given the presence of a continuum of CT exciton states in the real interface (see Chapter 1), this approximation is rather conservative and perhaps underestimates ΔE_c and the ability to dissociate excitons at a particular interface. The ΔE_c values derived at this combined level of theory are shown in Figure 3.12a (BSE ΔE_c curve), and are used below to compute the PCE; within this approximation, the useful range for PV operation is restricted to C domain sizes of up to $\sim$1 nm, for which the $\Delta E_c > 0$ condition is met.[†] The three CBN/PCBM interfaces satisfying this condition include the CBN layers $C_1(BN)_7$, $C_2(BN)_6$ and $C_3(BN)_5$, as seen from the BSE curve in Figure 3.12a. For these cases, we estimate upper limits for the PCE. Following Scharber *et al.*[25], the maximum PCE η for CBN/PCBM devices with type-II alignment is computed as:

$$\eta = \frac{0.65 \cdot (E_{opt,D} - \Delta E_c - 0.3) \cdot \int_{E_{opt,D}}^{\infty} J_{ph}(E)\, dE}{P_{in}} \tag{3.2}$$

where 0.65 is the assumed FF value, $J_{ph}(E)$ is the AM1.5G solar energy flux (in units of photons/cm^2·s·eV)[21] at the photon energy E, and $E_{opt,D}$ is the optical band gap of the CBN donor. In eq. 4.2, the $(E_{opt,D} - \Delta E_c - 0.3)$ term is an estimate of the maximum V_{oc}, calculated as the effective interface gap $\Delta = E_{opt,D} - \Delta E_c$, taken here between the DFT HOMO level of the donor and the GW LUMO level of the acceptor, minus 0.3 eV which accounts for a loss term

[†]We remark that given the choice to work in the combined BSE-donor, GW-acceptor scheme as well as using CBN superlattices instead of dot geometries, the C domain size delimiting type-I and type-II behaviors found here is expected to be a lower bound, and type-II interfaces may be found for larger C domain sizes in practice.

compared to the limit V_{oc} due to transport (see Chapter 1). The integral in the numerator is the short circuit current J_{sc} calculated using a limit external quantum efficiency (EQE, the ratio of the incident photons and extracted electrons) of 100 %, while the denominator is the integrated AM1.5G solar energy flux, which amounts to 100 mW/cm^2. The efficiency η is thus estimated as the product $J_{sc} \cdot V_{oc} \cdot$ FF normalized by the incident energy flux, in the limit of unity EQE.

Figure 3.12b shows the efficiency of the three CBN-PCBM interfaces with type-II alignment, as a function of the CBN donor optical gap and the interface ΔE_c, the latter computed as the difference between the optical LUMO level of CBN and the GW LUMO level of PCBM, as explained above. For the $C_1(BN)_7$, $C_2(BN)_6$ and $C_3(BN)_5$ monolayers, the computed efficiency values are, respectively, 11%, 15% and 20%. We observe that a larger C domain size leads to a smaller conduction band offset ΔE_c combined with a smaller optical gap. This combination is desirable since more of the donor gap contributes to the interface gap, thus yielding potential for larger voltage, while at the same time allowing to absorb more sunlight due to the smaller optical gap. The error analysis, carried out in ref.[103], yields a relative error of the order of $\frac{\Delta\eta}{\eta} \approx 0.1-0.15$. This translates to an overall efficiency range of $\eta = 10-20 \pm 3\%$ for the three type-II cases studied here, where higher efficiencies values correspond to larger C domain sizes. We remark that our assumptions here to obtain these high efficiency values would imply a quantitative absorption of sunlight from CBN, for which stacking several layers up to $\sim$10 nm thickness may be necessary. While the efficiency values should be understood as maximum limits, the striking efficiency tunability found here is a relevant property to optimize efficiency in PV, and is achieved by merely varying the C domain size within the CBN monolayer in a $\sim$1 nm range. Though such small C domains might seem challenging to achieve in practice, the immiscibility of C and BN in a monolayer leads to the formation of a large amount of sub-nm scale domains, to the point that single C and BN domains cannot be resolved in as-synthesized CBN monolayers[85]. While several approaches for controlling the domain size and shape at the atomistic scale in CBN are being actively explored[104,105], the strategy found here to tune the band gap by laterally confining excitons in two-dimensional monolayers is general, and can be extended to other monolayer materials for which the domain size requirements may be significantly less stringent.

Part of our study are also the CBN/s-SWCNT and CBN/CBN interfaces in Figure 3.11c–d, which are analyzed in detail in ref.[103] Briefly, we find that CBN/s-SWCNT interfaces can also achieve type-II alignment for C domain sizes in CBN of up to $\sim$1 nm and for nanotube diameters $d < 1.2$ nm. At these interfaces, CBN behaves as the donor, and s-SWCNT as the acceptor, similar to CBN/PCBM. For CBN/CBN interfaces with different C domain sizes, we also observe the possibility to form type-II interfaces. Our results suggest that it may be possible to fabricate a two atomic layer thick ($\sim$3.3 Å) solar cell device by stacking two CBN monolayers with the proper C domain structure. Alternatively, given the tunability of the CBN layer electronic structure, a Schottky junction solar cell may be formed between graphene and a monolayer of CBN. While a similar device would likely not absorb a large fraction of sunlight and thus

present low efficiency, it could constitute a new platform for the experimental study of quantum transport effects (characteristic of 2D monolayers) under PV operation, and could further achieve high generated power per unit volume of active layer; this topic is developed in detail in the next session in the context of ultrathin solar cells based on transition metal dichalcogenide monolayers.

A suite of transport phenomena not possible in thicker BHJ solar cells may be possible in solar cell devices based on just a few stacked monolayers. For example, while hot carrier injection and hot exciton dissociation are possible at or near an interface[106], in BHJ nanoscale solar cells they're hindered by the need for excitons to diffuse through the bulk of the absorber. However, if a solar cell is made with just one or two monolayers, no bulk diffusion would be involved and the hot carrier regime could be enabled. Similarly, it could be possible to study the impact of coherent exciton transport performance, a topic poorly explored in PV due to the fact that exciton transport operates in an incoherent regime in μm thick BHJ solar cells. As a test bed for these fundamental effects, as well as for the validation of the band offsets predicted in this work, we propose in Figure 3.13 an architecture whereby ultrathin solar cells based on monolayer materials could be fabricated and characterized – for example using time-resolved spectroscopy measurements – to study the presence of hot exciton or hot carrier effects. Other device examples are considered in the next section.

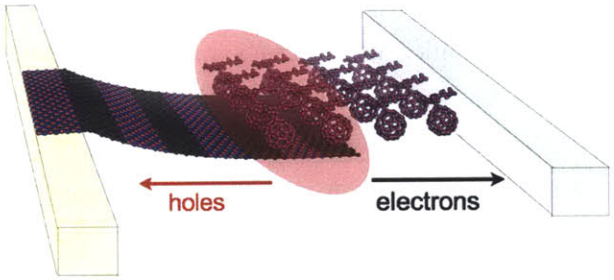

Figure 3.13: CBN/PCBM ultrathin solar cell. Proof-of-concept design of a solar cell based on semiconducting monolayer materials, for the CBN/PCBM material combination. Note that the PCBM could be replaced by a second monolayer, and the same architecture can be extended to other monolayer materials. The shaded oval indicates the interface where excitons are dissociated upon illumination (from the top in figure), and the arrows indicate the direction of carrier diffusion and extraction at the contacts, shown as thin metal fingers.

In summary, we introduce the idea of solar cells based on semiconducting monolayer materials using the case of CBN monolayers, for which tunable optical and electronic properties are possible due to exciton quantum confinement within C domains. We show the potential to achieve efficiencies of 10–20% in CBN/PCBM solar cells. Even a photovoltaic device as thin as two atomic layers of CBN (or other monolayer materials with type-II band alignment) holds the potential to achieve solar energy conversion at exceptionally small length and ultra-fast time scales. While a similar device configuration would allow one to probe transport in this poorly

explored physical regime, multi-layer stackings could be employed to absorb a significant fraction of incident sunlight, and could enable ultra-thin solar cells based on photostable materials with high carrier mobility. The unique tunability in two-dimensional monolayer materials of the band gap, interface band alignment, exciton binding energy, optical absorption, carrier mobility, and electron-phonon coupling entails new exciting opportunities for fundamental studies and practical implementation of solar cell devices. Additional tuning of physical quantities of interest in PV could be achieved by stacking sequences of different semiconducting monolayers or by chemical functionalization of monolayers. The exploration of this extremely vast design space for PV starts with the work presented in this thesis.

3.2.2 Transition Metal Dichalcogenides for Sunlight Absorption and Angstrom-Thick Solar Cells

We develop further the discussion on monolayer based PV by showing our recent work on Angstrom-thick solar cells based on graphene and transition metal dichalcogenide (TMD) monolayers. Graphene and TMD monolayers are promising materials for next-generation ultrathin electronic and optoelectronic devices[91,107,108,86,109]. Although visually transparent, graphene is an excellent sunlight absorber achieving 2.3 % visible light absorbance in just 3.3 Å thickness[110], *versus* visible absorbances in the 0.05−0.5 % range for 1 nm thick Si and GaAs[111], namely two of the most commonly used absorbers in solar cells. Similarly, TMD monolayer materials[112] may also hold potential as sunlight absorbers, and due to their semiconducting character may enable ultrathin PV devices, based for example on TMD bilayer heterojunctions or TMD monolayer/graphene Schottky barriers. We discuss here our calculations of accurate absorbance spectra for MoS_2, $MoSe_2$, and WS_2 TMD monolayers, and show they can absorb up to 5−10 % incident sunlight in a thickness of just a few Angstroms, thus achieving one order of magnitude higher sunlight absorption than 1 nm thick GaAs and Si. We further demonstrate the feasibility and estimate the performance of PV devices based on two stacked monolayers in the form of 1) a Schottky barrier solar cell between p-type MoS_2 and graphene, and 2) an XSC based on a MoS_2/WS_2 bilayer. Our calculations suggest that such active layers can attain power conversion efficiencies of up to ∼1 %, using 9−12 Å thick materials weighing only a few mg/m^2; this corresponds to enormous power densities[113] of up to ∼2.5 MW/kg (or ∼10 MW/L), a value higher than any existing energy conversion device and higher by a factor of 100−1,000 than the best ultrathin solar cells based on GaAs or Si. Our work shows that two-dimensional monolayer materials such as MoS_2 and graphene hold yet untapped potential to push PV operation toward Angstrom length scales and ultrahigh power density regimes.

TMD monolayers such as MoS_2, $MoSe_2$, and WS_2 display unique optical properties. For example, they undergo a crossover from indirect to direct gap when going from bilayer to monolayer[114], resulting in enhanced monolayer absorption and photoluminescence[115,88,89]. It may

appear counterintuitive to use graphene as a key active material in PV given its transparency and metallic behavior. However, the idea of coupling a semiconducting TMD monolayer with graphene to create a bilayer Schottky barrier solar cell is viable. Similarly, solar cell active layers obtained by stacking two different TMD monolayers are also possible, but have received little attention to date. In this section we study the feasibility and predict the performance of Angstrom-thick solar cells based on bilayers of MoS_2/graphene or two stacked TMD monolayers. First, we use a combination of first principles calculations based on DFT and the GW-BSE approach to compute accurate absorbance spectra for MoS_2, $MoSe_2$, WS_2, and graphene, showing quantitative agreement with experiment for the two materials for which accurate absorbance measurements are available (MoS_2[114] and graphene[110]). Our calculations show that a *single TMD monolayer* of a few Angstrom thickness can absorb 10−20 times more sunlight than 1 nm thick GaAs and Si, and generate electrical currents as high as 2−4 mA/cm^2. Next, we compute the maximum short-circuit current and interface band alignment in MoS_2/graphene and MoS_2/WS_2 bilayers, and demonstrate that both these interfaces can realize PV operation, respectively, by formation of Schottky barriers and type-II heterojunctions. Using conservative assumptions for the fill factor and internal quantum efficiency, we estimate that such bilayer solar cells can reach over 1 % PCE in just ∼10 Å thickness, thus packing a power density of up to 2.5 MW/kg, a value that is far superior to any known energy conversion or storage device. We believe that these calculations illustrate new avenues for nanoscale solar energy conversion using monolayer TMD and graphene. The full details of this work is reported in ref.[116], and the computational details are reported as an Appendix to this chapter.

Accurate computation of optical absorption in TMD monolayers (Figure 3.14a) is difficult due to a number of technical reasons. In this work, we combine density functional theory (DFT) calculations with the GW method[27] and the BSE[28] as subsequent levels of theory to obtain the macroscopic dielectric tensor including an accurate account of electron-electron and electron-hole interactions, as well as spin-orbit and semi-core state effects (see Appendix). Figure 3.14b compares the MoS_2 monolayer absorbance measured experimentally by Li *et al.*[114] with the one calculated in this work. The quantitative agreement observed between the computed and experimental absorbance highlights the accuracy of our approach. Figure 3.14c shows the absorbance calculated for the three TMD monolayers MoS_2, $MoSe_2$, and WS_2, compared to the absorbance of graphene (as computed here, in excellent agreement with the flat 2.3 % value measured by Nair *et al.*[110]) and to the incident AM1.5G solar spectrum[21]. We predict that TMD monolayers possess a high absorbance of 5−10 % in the visible, and can thus capture a significant fraction of incident sunlight. Table 1 compares the absorbed photon flux J_{abs} in graphene, the three TMD monolayers studied here, and 1 nm thick layers of materials commonly used in thin-film inorganic (Si, GaAs) and organic (P3HT polymer) solar cells, whose absorption spectrum was taken from experimental data in the literature.

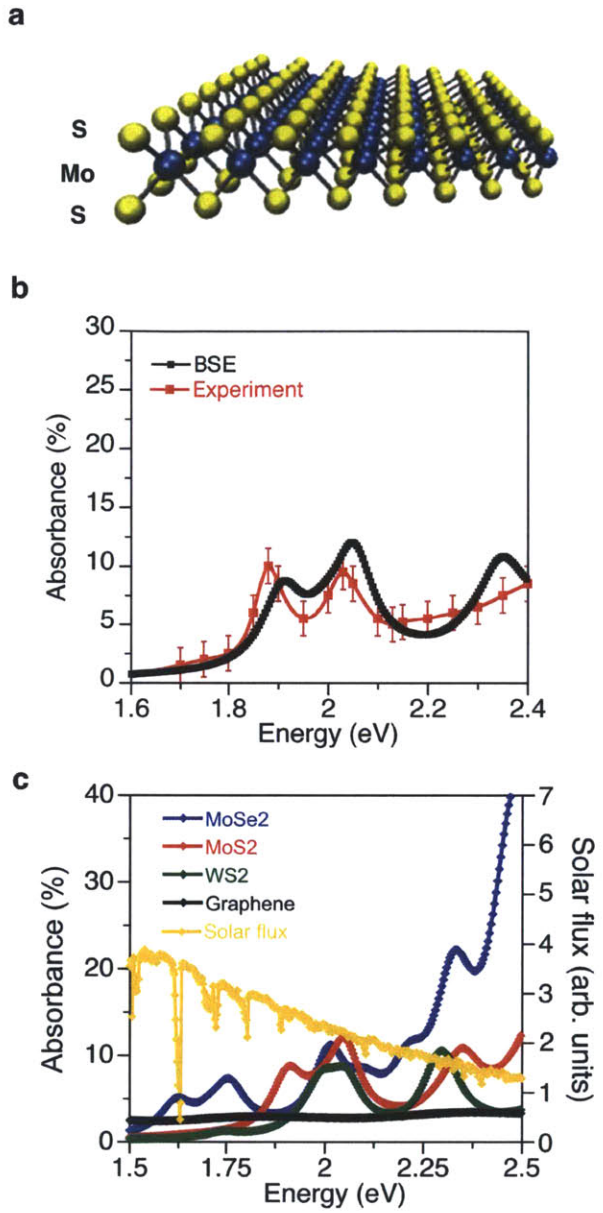

Figure 3.14: **Absorbance of TMD monolayers.** **a,** Schematic drawing of the MoS_2 monolayer structure used in this work. The yellow spheres represent S atoms and the blue spheres Mo atoms. **b,** Comparison of the computed and experimental absorbance of monolayer MoS_2. The error bars in the experimental curve were taken with an absolute value of ± 1.5 % due to the presence of a non-zero baseline in the spectrum in ref.[114] **c,** Absorbance of three TMD monolayers and graphene, overlapped to the incident AM1.5G incident solar flux.

For each material, J_{abs} is calculated using the absorbance $A(E)$ from the integral:

$$J_{abs} = e \int_{E_g}^{\infty} A(E) J_{ph}(E) dE \tag{3.3}$$

where E_g is the optical gap of the absorber, $J_{ph}(E)$ is the incident photon flux (units of photons/$m^2 \cdot s \cdot$ eV), and E is the photon energy. By multiplying through the elementary

charge e, the absorbed photon flux is expressed as the equivalent short-circuit electrical current in the ideal case when every photon is converted to a carrier extracted in a PV device, so that J_{abs} sets the upper limit for the contribution of the single material to the solar cell short-circuit current. We remark that this choice of units represents nothing more than a convenient way to quantify sunlight absorption, and is fully equivalent to expressing the results in terms of the absorbed photon flux.

We note the stunning result that graphene ($\sim$ 3 Å thickness) and TMD monolayers ($\sim$ 6 Å thickness) can absorb, respectively, photon fluxes equivalent to short-circuit currents of up to 2 mA/cm^2 and 2.5–4.5 mA/cm^2, while 1 nm thick Si, GaAs, and P3HT all generate currents in the 0.1–0.3 mA/cm^2 range. The very high absorbance of two-dimensional monolayer crystals in the visible can be understood by the presence of a continuum of available states for optical transitions, in contrast to monolayers of conjugated small molecules and polymers, as well as by a direct gap and strong excitonic effects for the case of TMD monolayers[117]. In addition, both TMD and graphene possess dipole allowed transitions between the orbitals dominating the valence band maximum (VBM) and conduction band minimum (CBM): p-p transitions in the case of graphene, and d-d transitions in the case of TMD, respectively. While Si is well-known to be a poor absorber in the visible due to its indirect band gap, GaAs has a direct gap and is one of the best known sunlight absorbers, and yet shows much lower potential to absorb sunlight in ultrathin films compared to graphene and TMD monolayers. The exceptional sunlight absorption of monolayer materials as shown in Table 1 suggests the possibility to design solar cells based on just two stacked monolayers, a topic we develop in the remainder of the paper.

The first Angstrom-thick device we examine is based on a bilayer of MoS_2/graphene as the

Table 2: Absorbed photon flux J_{abs} under AM1.5G solar illumination for graphene and TMD monolayers, computed using eq. 3.3 with the absorbance values in Figure 3.14c. J_{abs} quantifies the flux of absorbed photons, converted to units of equivalent electrical current. The optical gap of each material is also shown (taken from the literature, as referenced in the Table). The same quantities are shown for 1 nm thick representative bulk materials of relevance in ultrathin PV, whose absorption coefficient α was taken from the literature (see refs. in the Table) and converted to absorbance for a flat layer of thickness $L = 1$ nm using $A = 1 - e^{-\alpha L}$.

Material	E_g (eV) at 300K	J_{abs} (mA/cm^2)
Graphene	0.0	2.0
MoS_2	1.89[114]	3.9
$MoSe_2$	1.64[88]	4.6
WS_2	1.96[89]	2.3
Si	1.11[111]	0.1
GaAs	1.42[111]	0.3
P3HT	1.95[51]	0.2

active layer material; since graphene is a (semi)metal and MoS_2 is a semiconductor, the solar cell can operate through the formation of a Schottky barrier (SB). Given that in the MoS_2/graphene bilayer studied here the two monolayers are the only sunlight absorbers, the concept we propose is radically different from previously studied SB solar cells between graphene and Si, which have been shown to achieve efficiencies up to 9 %[118] stemming from the use of a thick Si layer as the main absorber.

Using DFT calculations, we compute a workfunction value of $\phi_{MoS_2} = 5.2$ eV for a MoS_2 monolayer, in agreement with the recent experimental observation of ohmic contact between n-type MoS_2 and Au[86]. The experimentally measured workfunction of graphene is commonly reported to be in the 4.3–4.6 eV range, close to the value of $\phi_G = 4.25$ eV computed here. On this basis, a solar cell can be formed using a bilayer of MoS_2/graphene interfaced to a high workfunction metal on the MoS_2 side and a low workfunction metal on the graphene side (Figure 3.15a). In order for such a device to work, electron-hole pairs generated in either material composing the interface should be separated through the formation of a SB. We employ DFT combined with the lineup method[119] to estimate the SB at an interface between graphene and a defect-free, undoped layer of MoS_2 (see Appendix). Our calculation suggests the formation of a SB of 1.2 eV for holes to diffuse from graphene to MoS_2, thus enabling the design of SB solar cells between p-type MoS_2 and graphene. Charge separation occurs by injecting photogenerated electrons from the conduction band of MoS_2 to graphene, while holes photogenerated in the valence band of MoS_2 cannot diffuse to graphene due to the large SB (see Figure 3.15b). Notably, electron injection from MoS_2 to graphene upon illumination as predicted here has been observed by recent experiments in MoS_2/graphene phototransistors[120]. Under these operating conditions, the maximum open circuit voltage $V_{oc,max}$ is set by the difference between the SB and the built-in potential, given that holes are extracted at the VBM in MoS_2 (namely, the maximum quasi-Fermi hole level that can be reached under illumination). We estimate a relatively small $V_{oc,max} \approx 0.3$ eV, computed as the difference between the SB and the built-in potential $\phi_{MoS_2} - \phi_G$ obtained from the DFT workfunctions of MoS_2 and graphene (ϕ_{MoS_2} and ϕ_G, respectively). We remark that this result is prone to variations in a real device depending on Fermi-level pinning at the MoS_2/metal interface and on device processing conditions, so that a quantitatively accurate limit of the open-circuit voltage can only be predicted when all such variables are defined. While our calculations suggest the requirement of p-type doping in MoS_2, some experiments have shown that MoS_2 deposited on SiO_2 shows n-type behavior[86]. However, recent calculations suggest that the doping type in MoS_2 may not be intrinsic but rather due to impurities or dangling bonds at the SiO_2 surface[121], as further supported by several experiments reporting p-type behavior in MoS_2[121]. Figures 3.15c–d show other important aspects of the MoS_2/graphene bilayer proposed here. Upon formation of the interface, our calculations suggest a significant ground state charge redistribution in the system, as also observed in a recent study by Ma *et al.*[122] Despite this effect, the projected density of states (PDOS) shows that the electronic states of graphene and MoS_2 do not hybridize near the Fermi energy (Figure 3.15c). In

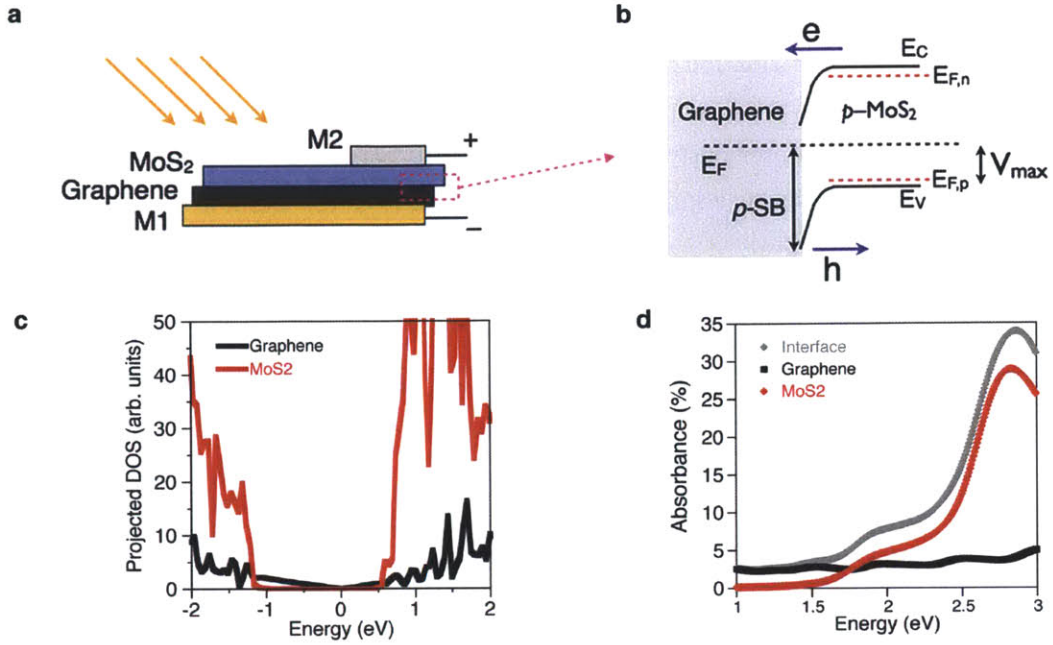

Figure 3.15: **MoS_2/graphene interface and Schottky barrier solar cell. a,** The MoS_2/graphene solar cell described in this work. M1 and M2 are, respectively, low and high workfunction metals. The contact exposed to sunlight should be transparent or cover only a small portion of the surface. **b,** Band alignment at a MoS_2/graphene interface, as predicted using DFT. p-SB is the hole Schottky barrier; also shown are the valence and conduction band edges (E_v and E_c, respectively) of MoS_2 as well as the quasi-Fermi levels for electrons and holes under illumination ($E_{F,n}$ and $E_{F,p}$, shown as red dashed lines), together with the direction of electron and hole diffusion. V_{max} is the maximum open-circuit voltage. **c,** PDOS of a MoS_2/graphene interface. The energy is referenced to the Fermi energy. **d,** Absorbance of the MoS_2/graphene interface and its composing monolayers, computed at the DFT-RPA level of theory.

addition, the absorbance at visible photon energies (computed here using DFT-RPA due to the large size of the simulation cell) is equal to the sum of the absorbances of isolated graphene and the MoS_2 monolayer (Figure 3.15d). Using the absorbance spectrum in Figure 3.15d and eq. 3.3, we estimate a maximum short-circuit current of $J_{abs} = 4.3$ mA/cm^2 for a MoS_2/graphene active layer. This value differs slightly from the sum of the monolayer currents in Table 1 (5.9 mA/cm^2) due to the use of different levels of theory (BSE in Table 1, and independent-particle in Figure 3.15d); for our purpose here it suffices to establish that a maximum short-circuit current of ~4.5 mA/cm^2 can be achieved. We estimate a range of PCE values for the MoS_2/graphene solar cell in Figure 3.15a by using $J_{abs} = 4.5$ mA/cm^2 combined with: 1) for the lower PCE limit, an open circuit voltage $V_{oc} = 0.1$V and a small fill factor (FF) of 0.3, namely a reasonable value for a "poor" solar cell device with high series and low shunt resistances, and 2) for the upper PCE limit, $V_{oc} = 0.5$V and FF=0.6 as a reasonable fill factor value in a device with decent carrier transport[17]. In all cases, a conservative value of 0.7 is assumed for the internal quantum efficiency (IQE, namely the fraction of absorbed photons extracted as carriers at the contacts), a value significantly lower than the best Si and GaAs solar cells achieving IQE close to unity.

This approach corresponds to assuming that only 70% of the absorbed photons contribute to the current, resulting in a short-circuit current $J_{sc} = 0.7 \cdot J_{abs}$ in the solar cell device. We compute the PCE under AM1.5G illumination by dividing the product $J_{sc} \cdot V_{oc} \cdot FF$ through the incident power of 100 mW/cm^2,[17] resulting in a PCE range of 0.1−1.0 % for a bilayer of MoS_2/graphene. Despite the relatively low efficiency compared to thicker active layers, the power generated by a unit volume or mass of active layer material (power density) achieved by a MoS_2/graphene solar cell is incredibly high. Table 3 compares the power density of a MoS_2/graphene solar cell

Table 3: Comparison between the performance of record ultrathin solar cells based on Si and GaAs and the MoS_2/graphene and bilayer TMD solar cells studied here. Thickness and weight refer solely to the device active layer. Efficiency is the PCE under AM1.5G illumination. P.D. is the power density.

Material	Thickness	Efficiency	Weight (g/m^2)	P. D. (kW/L)	P. D. (kW/kg)
GaAs	1 μm	~29%[123]	5.3	290	54
Si	35 μm	20.6%[124]	92.7	5.9	2.5
Graphene/MoS_2	9.4Å	0.1−1.0%	$3.9 \cdot 10^{-3}$	1,000−10,000	250−2,500
WS_2/MoS_2	12.5Å	0.4−1.5%	$7.9 \cdot 10^{-3}$	3,000−12,000	450−1,800

to the power density of ultrathin solar cells based on GaAs[123] and Si[124] with current records of thickness and efficiency. We estimate that a MoS_2/graphene bilayer with a thickness of ~ 9.5 Å, a weight of 3.9 mg/m^2, and an efficiency of 0.1−1.0 % as derived above would achieve a power density of 1.0−10.0 MW/L (or 0.25−2.5 MW/kg), higher by a factor of 100−1,000 than existing record solar cells, and higher than any known energy generation and conversion device[3,113]. We remark that although power density is not a conventional figure of merit in PV, it is an important metric to understand the ultimate power generation limits in solar cells achieving the smallest possible thickness, as well as to estimate the energy achievable from a unit volume or weight of active layer material. For example, Table 3 indicates that a 1 % efficient solar cell based on MoS_2/graphene is 30 times less efficient than the best 1 μm thick device based on GaAs, but using a thickness 1,000 times smaller; this corresponds to a generated power per unit volume (or equivalently, per unit thickness) higher by a factor of ~30 for MoS_2/graphene compared to GaAs.

We highlight the fact that the PCE (and thus power density) values estimated here for a MoS_2/graphene solar cell are by no means speculative: the absorbed photon flux J_{opt} is estimated from accurate calculations of the absorbance closely matching experimental results (Figure 3.14b), the chosen V_{oc} values are moderate (0.1 − 0.5 V) and within the range estimated above using DFT, and a realistic range of FF values[17] of 0.3−0.6 as well as a moderate IQE value of 0.7 were assumed in our calculations. Rather conservative values have been chosen for all the quantities composing the PCE, and the high power densities obtained are the sole consequence of the high absorbance for very small thickness in graphene and TMD monolayers.

We next estimate the feasibility and performance of another possibility for Angstrom-thick

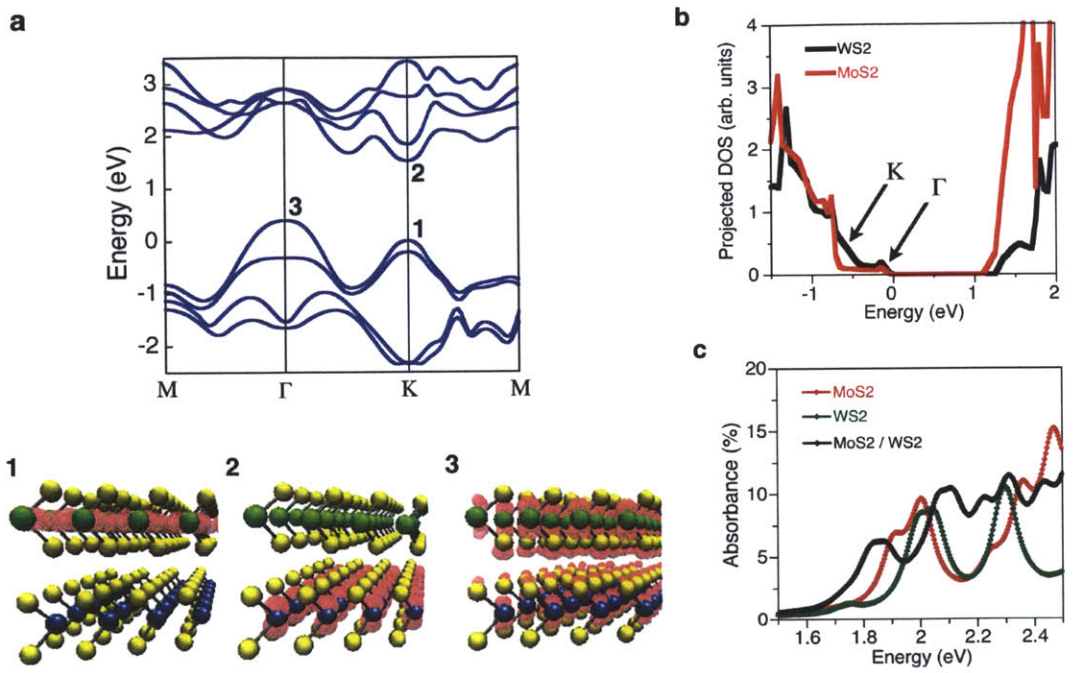

Figure 3.16: MoS_2/WS_2 interface and excitonic solar cell. **a,** DFT bandstructure of the MoS_2/WS_2 bilayer. Shown in red below the plot is the charge density associated with the wavefunctions for the $\vec{k}$-points and bands marked as 1–3. At the K point, the VBM stems from states in WS_2 and the CBM from states in MoS_2, while the VBM at Γ shows contributions from both layers. The atoms are shown as yellow (S), blue (Mo), and green (W) spheres. **b,** PDOS of the MoS_2/WS_2 bilayer, showing type-II alignment, consistent with the charge density plots shown in **a**. The energy is referenced to the Fermi energy, and the arrows indicate PDOS features in the VBM due, respectively, to electronic states at the K and Γ points of the Brillouin zone. **c,** Absorbance spectra of the MoS_2/WS_2 bilayer and of the individual composing layers, computed using BSE.

PV, this time constituted by an interface between the two semiconducting monolayers MoS_2 and WS_2, which would need to form a type-II heterojunction to enable exciton dissociation and charge separation[13]. Different from the MoS_2/graphene interface, the interaction between the antibonding orbitals in the two layers leads to significant changes in the bandstructure and absorption spectrum. The DFT bandstructure of the MoS_2/WS_2 interface shows an indirect gap due to the interaction of the antibonding orbitals in the two TMD monolayers lifting the energy of the VBM at Γ (Figure 3.16a). The VBM at K shows contributions only from in-plane d orbitals of WS_2, while the CBM at K is contributed only by d_{z^2} orbitals of MoS_2; this set of orbital contributions to the electronic states is common in TMD systems[125]. The band gap at the K point is typically responsible for the photoabsorption onset at visible energies in TMD systems. In the present case, the nature of the electronic states at the K point implies that the absorption of a photon with visible energy transfers an electron from a state localized on MoS_2 to a state localized on WS_2, thus achieving the formation of a charge-transfer exciton shared by the two layers. Consistent with this picture, a type-II alignment favorable for solar cell operation

is achieved at the MoS_2/WS_2 interface, with WS_2 as the donor and MoS_2 as the acceptor, as shown by the analysis of the PDOS in Figure 3.16b [1]. Although the VBM states near the Γ point are an exception as they stem from both monolayers and may act as recombination centers, we expect the key photoexcitation at visible photon energies to involve states at the K point and thus conclude that the observed band alignment would lead to effective PV operation. Owing to the interlayer interaction leading to the formation of an indirect gap, the optical absorption spectrum of the bilayer obtained from BSE shows significant differences from the sum of the spectra of the two composing layers (Figure 3.16c). Not only is the bilayer spectrum lower than the sum of the spectra of the individual layers, but it also shows the formation of a lower absorption edge compared to the composing layers, thus confirming the presence of charge-transfer excitons. Using eq. 3.3, we estimate a maximum short circuit current $J_{opt} \approx 3.5$ mA/cm^2 for the MoS_2/WS_2 bilayer (close to the value for isolated MoS_2), and we extract from the PDOS a maximum open circuit voltage of ~1 V, equal to the band gap of the type-II interface (see Figure 3.16b). Using an IQE value of 0.7, FF values in the 0.3–0.6 range as above, and a V_{oc} of 0.5–1 V, we estimate PCE values of 0.4–1.5 % for a bilayer of MoS_2/WS_2 with ~ 12 Å thickness and a weight of only 7.9 mg/cm^2, resulting in ultra-high power densities similar to the MoS_2/graphene case (see Table 3).

The PV efficiencies computed here could be increased using a number of strategies in a real device. For example, an increase by a factor of two in the efficiency compared to what is estimated here can be gained using a double pass of light in the active layer, as obtained by employing a back metallic contact. In addition, since the absorbance of graphene and MoS_2 has been measured to double and triple, respectively, for a bilayer and trilayer[110,114], a stacking of three graphene monolayers and three MoS_2 monolayers with a back metallic contact may afford maximum efficiencies close to 10 % in a 3 nm thick active layer. A similar configuration would require that a SB can be formed at a trilayer graphene/trilayer MoS_2 interface, a point worthy of additional investigation. We further suggest that given the variability of band gaps observed in TMD monolayers, usually in the 1.5–2.5 eV range and decreasing for increasing sizes of the chalcogen atom, significant band gap engineering is possible using stacked TMD bilayers and multilayers. This scenario entails novel possibilities to form broadband sunlight absorbers and enhance efficiency considerably beyond the values estimated here. Finally, since MoS_2 and other TMD can catalyze water splitting[126,127], the excellent sunlight absorption properties predicted here for TMD monolayers could also be employed in the photoelectrochemical generation of hydrogen. In conclusion, our calculations unveil and quantify the potential of graphene and TMD monolayers for solar energy absorption and conversion using Angstrom-thick PV active layers for application (among others) as high power density sources for aerospace, military, and

[1] We note that although the type-II alignment is inferred here from a DFT calculation, the BSE optical gaps are numerically close to the DFT gaps due to a compensation of errors at the DFT level. This situation is also found in other monolayer systems[99]. Hence, correcting the DFT gaps to the BSE optical gaps would not change the type-II alignment for the MoS_2/WS_2 interface.

nanoelectronics. Our work opens a search for monolayer materials with similar band gaps and monolayer absorbances to those reported here to be employed in next-generation solar energy conversion devices.

3.3 Appendix

We detail the methods employed to obtain the results in Section 3.2.2. We employed *ab initio* DFT, GW, and BSE calculations using the VASP code[36,38], as detailed below.

TMD, graphene, and bilayer structures. Monolayer TMD were modeled using experimental lattice constants as in ref.[128], and further relaxed within DFT. This approach is known to give accurate physical properties, such as direct DFT band gaps as well as accurate Raman shifts[128,129]. For monolayer graphene, a relaxed lattice constant of 2.48Å was used. The bilayer structures were relaxed using the van der Waals functional from Grimme[130] as implemented in the VASP code. For the MoS_2/graphene bilayer, a 4 x 4 hexagonal supercell of MoS_2 with experimental lattice constants was placed at a van der Waals distance of 3.3Å from a 5 x 5 hexagonal supercell of graphene, adopting the so-called TS stacking with C atoms on top of S atoms in MoS_2 (see ref.[122]). To achieve in-plane structural matching, a 1.3% strain was imposed in the graphene layer. We have verified that 1) this strain does not affect the bandstructure of graphene, and 2) the relaxed and unrelaxed bilayer structures yield the same bandstructures and Schottky barriers to within a few meV. The MoS_2/WS_2 bilayer unit cell consisted of stacked three-atom unit cells of the two monolayers. The experimental lattice parameters of MoS_2 were adopted, and the two layers were arranged with AB stacking (also called C7 stacking, see ref.[131]). Since the experimental lattice constants of MoS_2 and WS_2 are almost identical[128], this choice led to a negligible strain in the WS_2 layer. In both the monolayer and bilayer cases, spurious interactions with the image systems were avoided by using >18Å vacuum in the layer-normal direction, consistent with previous work[117,128,132] and leading to converged results at all levels of theory used in this work.

DFT calculations. Commonly employed *ab initio* calculations in the framework of DFT are limited to quantities related to the electronic ground state, whereas excited state phenomena – such as photoabsorption – need more accurate treatment of electron-electron and electron-hole correlation[26,28]. DFT is employed in this work within the GGA approximation as a starting point to compute the Kohn-Sham wavefunctions and eigenvalues in unit cells of monolayer MoS_2, $MoSe_2$, and WS_2, using a plane wave basis set and periodic boundary conditions. Similar calculations have been previously shown to yield qualitatively correct bandstructures for monolayer TMD, featuring a direct gap at the K point responsible for the optical absorption onset[133,115,117]. We employ the GW method[27] and the BSE[28] as two subsequent levels of theory to obtain the macroscopic dielectric tensor including an accurate account of electron-electron and electron-hole interactions. We apply the GW method perturbatively, using so-called G_0W_0 calculations to obtain first-order corrections to the DFT eigenvalues, suitable as a starting point for BSE. We employed the PBE exchange-correlation functional[59] in combination with projector augmented wave (PAW) type pseudopotentials as implemented in the VASP package[134,78]. The GW version

of the PAW pseudopotentials supplied by VASP was employed for all atoms, providing accurate scattering properties at high energies[38]. In the study of the TMD materials, the PAW pseudopotentials represented the nuclei plus core electrons up to the $3d$ shell for Mo (thus explicitly including the $4s$ and $4p$ semicore electrons in the calculation) and up to the $5s$ shell for W (thus including the $5p$ semicore electrons in the calculation), while for S and Se atoms only the s and p electrons of the outermost shell were included. We employed kinetic energy cutoffs of up to 450 eV, and obtained spin-orbit split bandstructures in a perturbative way (similar to what done in ref.[117]) by using the LSORBIT tag in VASP with quantization axis in the plane-normal direction. We first performed a self-consistent calculation using a 32 x 32 x 1 Γ-centered Monkhorst-Pack[101] $\vec{k}$-point grid and with a strict tolerance of 10^{-8} eV on the total energy to obtain an accurate ground state charge density. Subsequently, we performed non-selfconsistent calculations with Γ-centered $\vec{k}$-point grids of up to 24 x 24 x 1 and over 170 empty bands to obtain Kohn-Sham wavefunctions and eigenvalues as a starting point for optical absorption calculations using the GW-BSE method (see below).

For the calculation of workfunctions and Schottky barriers, we averaged the Hartree potential in the layer-normal direction and computed the Fermi energy for the monolayer or bilayer under study. The workfunction was obtained as the difference between the vacuum Hartree potential and the Fermi energy. The Schottky barrier at the MoS_2/graphene interface was computed as the difference between the Fermi energy of the bilayer and the VBM energy in an isolated MoS_2 monolayer, corrected by the interface dipole potential as detailed in the work by Shan *et al.*[119] This approach is analogous to obtaining the Schottky barrier from the PDOS, by taking the difference of the Fermi energy and the VBM in the bilayer calculation. For the MoS_2/WS_2 interface, the type-II alignment was determined from the nature of the VBM and CBM in the PDOS. This approach is reliable in this particular case since the DFT gaps are close to the optical (BSE) gaps in MoS_2 and WS_2 due to a compensation of DFT errors in the estimate of the band gap and exciton binding energy, a common situation in two-dimensional monolayer semiconductors[99].

GW-BSE calculations. GW quasiparticle calculations were carried out using the perturbative ("one-shot") G_0W_0 approximation, starting from PBE Kohn-Sham wavefunctions and eigenvalues as described above. The energy cutoff for the response function was set to 150 eV, and increasing it up to 400 eV did not change the results for a fixed number (184) of empty bands. Our convergence study for TMD monolayers within the VASP implementation of GW is consistent with previous work[117], and our computed GW bandstructures and energy gaps agree with the literature[117,132]. We have also verified the validity of our convergence by simultaneously increasing the number of empty bands to 512 and the size of the response cutoff to 400 eV, and did not observe significant changes in the GW bandstructure and BSE optical spectrum. An important aspect of the G_0W_0 calculation carried out here is the role of semicore states of the

transition metal. While the explicit inclusion of semicore electrons for the transition metals Mo and W does not affect the DFT bandstructure, it is crucial to obtain a correct treatment of the exchange part of the self-energy at the G_0W_0 level of theory. We have verified for the case of MoS_2 that neglecting to include such semicore electrons in the calculation leads to erroneous G_0W_0 corrections with strong k-dependence, and to indirect quasiparticle gaps due to inadequate treatment of the exchange energy (see Figure 3.17); while all the calculations shown here were performed using the VASP code, these test calculations without semicore electrons were carried out using the Yambo code[37] coupled to DFT calculations using QUANTUM ESPRESSO[35].

Calculations of the macroscopic dielectric tensor within the BSE framework were performed

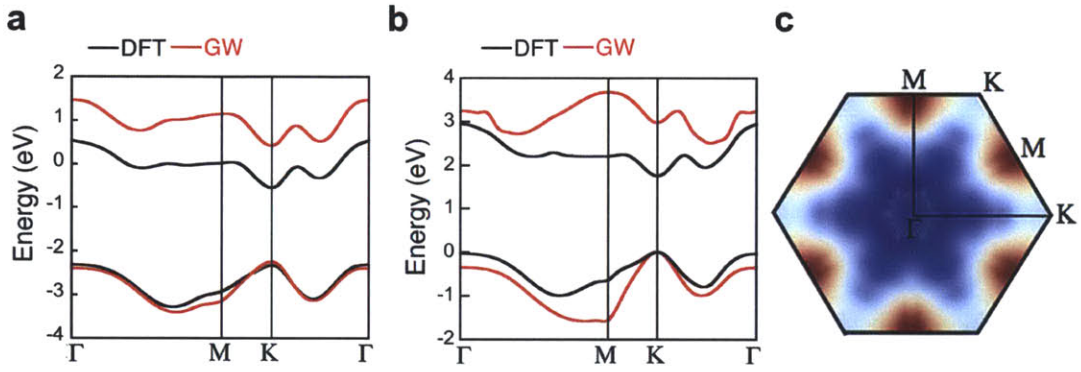

Figure 3.17: Role of semicore states in the G_0W_0 corrections. a, DFT and GW bandstructures of monolayer MoS_2 obtained including the $4s$ and $4p$ semicore states of Mo in the calculation. Shown are the highest valence and lowest conduction bands for each approximation. For comparison, **b** shows the DFT and GW bandstructures of monolayer MoS_2 obtained when the semicore states are not included, leading to the formation of an indirect GW gap and $\vec{k}$-dependent GW corrections to the gap, also shown in **c** with a color map ranging from red for the maximum value of the correction of 2.2 eV, to blue for the minimum correction to the gap of 0.6 eV. For comparison, a color map of the corrections when including semicore states as in panel **a** would show a homogeneous color deriving from the rigid shift of the GW lowest conduction band by $\sim$ 1 eV and almost no shift for the GW highest valence band.

starting from G_0W_0 eigenvalues and PBE Kohn-Sham wavefunctions (since the perturbative G_0W_0 scheme used here does not update the wavefunctions). A 16 x 16 x 1 Γ-centered Monkhorst-Pack[101] $\vec{k}$-point grid was used in the calculation of the BSE spectra in Figure 3.14, and spin-orbit effects were included perturbatively. We have verified carefully the convergence of the absorption spectrum with respect to the density of the $\vec{k}$-grid. We observed only slight variations between a 12 x 12 x 1 grid and the 16 x 16 x 1 grid employed for the spectra in Figure 3.14. Separate convergence tests of the BSE spectra were performed without spin-orbit employing $\vec{k}$-grids of up to 24 x 24 x 1, confirming that an adequate convergence can be achieved for $\vec{k}$-grids of 12 x 12 x 1 and denser. The BSE Hamiltonian was formed using the six highest valence bands and the eight lowest conduction bands using the Tamm-Dancoff approximation, and the dielectric tensor was output on a fine energy grid (2,000 points) up to 8 eV. Our methodology is similar to ref.[117],

but employs significantly denser k-grids in the Brillouin zone leading to full convergence of the dielectric matrix. For the three TMD monolayers, we observe optical gaps slightly exceeding the experimental value, likely due to finite temperature effects in the experiment, or to self-interaction errors in the Kohn-Sham orbitals[117]. To predict the correct absorption at room temperature, we limited ourselves to slightly red-shifting the optical spectrum by $\sim$100$-$200 meV to match the experimental absorption onset of each monolayer TMD studied here. This approach is sufficiently accurate for the scope of this work, as confirmed by the agreement with the experimental data (see Figure 3.14b).

Absorbance calculations. The procedure outlined above yields the imaginary part of the dielectric tensor $\epsilon_2(\omega)$ as a function of photon frequency ω, at energies relevant for interband optical transitions. Starting from $\epsilon_2(\omega)$, the monolayer absorbance $A(\omega)$ of monolayer TMD, defined as the fraction of photons of energy $E = \hbar\omega$ absorbed by the monolayer, is obtained using an approximation analogous to what used by Yang *et al.* for graphene[135]:

$$A(\omega) = \frac{\omega}{c}\epsilon_2 \, \Delta z \tag{3.4}$$

where c is the speed of light, and Δz is the size of the simulation cell in the layer-normal direction. This formula can be seen as a Taylor expansion for small thickness $\Delta z \to 0$ of the absorbance $A = 1 - e^{-\alpha \cdot \Delta z}$ for a flat layer of a bulk material with thickness Δz and absorption coefficient[23] $\alpha(\omega) = \frac{\epsilon_2 \omega}{cn}$, with refractive index $n = 1$ due to the presence of vacuum in the vast majority of the simulation cell. Equivalently, it can be seen as deriving from the polarizability per unit area[135], or from the optical conductivity of the monolayer. The absorbance defined with this approach is independent of the simulation cell size, since $\epsilon_2 \propto (\Delta z)^{-1}$. The ϵ_2 and absorbance for the MoS_2/graphene interface were computed within the independent-particle (RPA) approximation (rather than BSE), since the large size of the system (616 valence electrons) makes it impossible to apply BSE calculations in this case. Since RPA spectra usually underestimate the absorbance at low energies near the onset, our approach ensures a *conservative* estimate of J_{sc} and PCE for the MoS_2/graphene interface. This is confirmed by the fact that the sum of the BSE absorbances leads to a 30% higher J_{sc} current than the RPA result, as discussed in the main text.

4 Toward Multiscale Simulation of Excitonic Solar Cells

The work discussed so far in this thesis has focused on the study of donor-acceptor (D-A) interfaces with nanometer size. The models employed in this context are useful in predicting materials suitable for nanoscale solar cells, as well as estimating currents, voltages and efficiencies by computing a small number of spectroscopic quantities such as band gaps, band alignments, and exciton-related properties. It should be clear nevertheless that the study of D-A interfaces is a well crafted reductionist attempt to tackle the inherent complexity of XSC devices: however important it may be to capture the physics of photoinduced exciton generation and dissociation at D-A interfaces, the multi-scale nature of the processes taking place in a solar cell should always be kept in mind. In this chapter, we describe the key processes taking place in XSC and emphasize their different length and time scales, including exciton/carrier transport and sunlight management. We briefly outline models employed to study such processes across length and time scales, as well as possible pathways to combine these models and provide a true multi-scale framework to simulate XSC. We further discuss a case study from our own work on optimizing sunlight harvesting at the macroscopic length scale. In doing so, we hope to illustrate the vast array of processes involved in PV solar energy conversion, and complement the research examined in Chapter 3 centered on the nanometer length scale.

4.1 Modeling across Time and Length Scales in Nanoscale Photovoltaics

The D-A interface model described in Chapter 1 and used extensively throughout this thesis provides a *static picture* of the energetics of the quasiparticles (electrons, holes, and excitons) involved in the photoconversion process, and can suggest thermodynamically favored pathways for the ultrafast processes following photoabsorption. However, kinetic information regarding the rates of exciton formation, recombination, and dissociation through interface states is missing and would be valuable to extend our understanding of D-A interfaces into the time domain. Photoabsorption and exciton generation *per se* are remarkably fast processes: for a typical PV material with an energy gap of $E_g = 2$ eV, an order-of-magnitude estimate of the time τ_f for exciton formation yields $\tau_f \approx \hbar/E_g \approx 0.1$ fs. Such subfemtosecond time scales mark the beginning of an exciton's journey toward solar energy conversion. Sunlight absorption commonly results in moderate exciton densities of $\sim 10^{16}$ cm^{-3}, corresponding to the generation of one exciton per μs in a 1 nm^3 volume. Since a μs is a relatively long time scale compared to exciton dissociation and recombination times, solar radiation at the microscopic scale is diluted, and low excitation levels falling in the linear response regime are induced in the absorber material.

A number of competing processes follow exciton formation, as summarized in Figure 4.1. The first step consists in the diffusion of an exciton generated in the bulk of the donor or acceptor, or directly at the D-A interface; this process is often modeled as a random walk of a localized state, taking place within the exciton lifetime $\tau_r \approx 10-1{,}000$ ps and over length scales

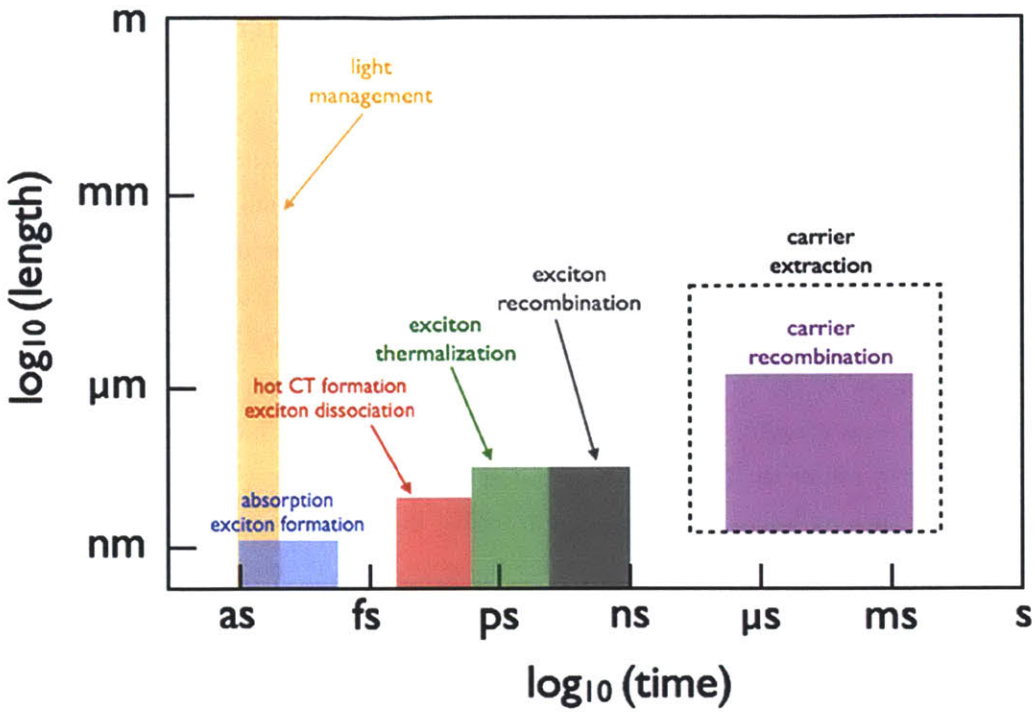

Figure 4.1: Time and length scales of physical processes in excitonic solar cells. Several processes involved from sunlight absorption to charge extraction in an excitonic solar cell. As the time scale increases, the length scales are also seen to increase, thus determining a speed for solar energy conversion. Different simulation techniques are employed to model processes at different length and time scales.

of 5−20 nm. If the exciton does not encounter a D-A interface during the diffusive process, it eventually recombines radiatively or non-radiatively. There is a wide variability in the exciton recombination lifetimes and diffusion lengths across molecular materials and nanostructures: for example, in P3HT/PCBM blends exciton lifetimes of ∼300−500 ps and diffusion lengths of 10 nm have been measured, while for SWCNT the lifetime depends on diameter and chirality and are generally in the 10−100 ps range for non-radiative decay rates, and up to 1 ns for radiative decay rates[136]. PbS and PbSe quantum dots (QD) employed in XSC defy the semiclassical picture of the exciton random walk due to large exciton radii of over 20 nm comparable with the spacing between heterointerfaces in the active layer, and generally show longer lifetimes of ∼1 μs[137]. We expect that long lifetimes may also hold for excitons in monolayer materials studied here due to their delocalized nature. In fact, Fermi's golden rule dictates the proportionality between inverse exciton lifetimes and the oscillator strength f: for more delocalized states, f becomes smaller, and longer exciton lifetimes are to be expected.

Provided an exciton can arrive at a heterojunction before decaying, several processes can occur at the interface, including the formation of hot CT excitons (CT_n) , trapped excitons in the CT_0 state (see Chapter 1), charge separated states leading to electron (hole) generation in the donor (acceptor), or recombination. These processes are the crux of charge carrier gener-

ation over very short (subpicosecond) time scales[14,15,16], and determine whether the absorbed solar energy is lost (in the case of recombination) or available in the form of mobile carriers with different electrochemical potentials (when charge separated states are formed). Subpicosecond dynamics at D-A interfaces has been the focus of recent time-resolved spectroscopic studies on polymer based solar cells, establishing that charge separation in some organic solar cells occurs within 100 fs of photoabsorption, while trapping into interface CT_0 states occurs over 1 ps and leads to exciton recombination[14,15,16]. The transient delocalization occurring in hot CT_n states, although short-lived (subpicosecond), allows for charges to decouple and move apart over longer time scales ($\sim$10 ps) leading to the formation of charge separated states and thus free charge carriers. Given the importance of these very short time scales for charge generation in nanoscale solar cells, we expect pump-probe time-resolved optical measurements to become a workhorse in the next decade in the study of nanoscale PV[138]. On the other hand, *ab initio* simulations in the time domain are lagging behind in the description of exciton dynamics at D-A interfaces. Although some calculations have appeared in the literature employing Ehrenfest nuclear dynamics coupled to constrained DFT[139], fundamental issues are yet to be solved and a reliable methodology is still lacking. We predict major efforts from the computational spectroscopy community to develop excited state dynamics simulations at the subpicosecond time scale in the next decade.

Following exciton dissociation at the D-A interface, the generated charge carriers migrate in a diffusive transport regime. The main driving force consists in concentration gradients (rather than electric fields as in conventional Si solar cells)[13], and is sufficient to transport carriers to the metallic contacts where they are extracted. When they are not extracted within their lifetime, carriers recombine radiatively or non-radiatively by phonon- or impurity-assisted processes. Active layers with dominant radiative recombination show strong fluorescence and are (somewhat counterintuitively) favorable for solar energy conversion due to smaller non-radiative losses yielding overall longer carrier lifetimes[123]. Mobilities of order $10^{-3}-10^{-6}$ cm^2/V·s and carrier lifetimes of 1$-$1,000 μs are typical in polymer and QD materials[9,140], leading to diffusion lengths in the 10 nm$-$1 μm range[†]. Monolayer materials and SWCNT proposed in this thesis possess much higher mobilities and are expected to significantly boost transport in XSC active layers.

While computing interface band alignments is a relatively well defined problem in XSC, different models and computational approaches exist to simulate transport. The ultimate goal of modeling transport in PV is to obtain current-voltage curves, from which the efficiency, fill factor, series and shunt resistances can be extracted. Transport models in principle complement the study of the D-A interface energetics, but are in practice limited by the need to assume simplified solar cell geometries, and the requirement of inputs such as lifetimes and mobilities often obtained from the experiment. The semiempirical character of semiclassical transport

[†]Assuming Fickian diffusion, the diffusion lengths L are estimated here as $L = \sqrt{D\tau}$, where τ is the lifetime and $D = \frac{\mu kT}{e}$ is the diffusion coefficient (μ is the mobility).

models limits their usefulness in several circumstances of interest, while the restricted length scales accessible with fully *ab initio* transport models makes realistic cases hardly tractable. Two common semiclassical schemes employed to study transport in PV are the so-called *drift-diffusion* and *kinetic Monte Carlo* methods, both able to describe diffusive transport (*i.e.* in the presence of scattering) over time scales up to carrier extraction at the electrodes. Drift-diffusion simulations are widespread in semiconductor device modeling, and employ a continuum description of carrier dynamics by solving self-consistent partial differential equations for the currents, carrier concentrations, potential, and Fermi energies in steady state[141]. In XSC, drift-diffusion models fall short in describing exciton dynamics, which is confined to a space-dependent carrier generation term within the formalism. On the other hand, a realistic description of light distribution within the active layer can be achieved, thus allowing one to couple the problem of light and carrier propagation. Standard software packages like COMSOL[†] provide finite element solvers for the partial differential equations involved, as well as graphic tools to prepare the device geometry. An alternative and often complementary picture is offered by kinetic Monte Carlo (KMC) models[142], providing a discrete dynamics for both excitons and charge carriers. In KMC simulations, a catalogue of possible processes and their rates are assumed for excitons and carriers. The PV active layer is spatially discretized, usually in the form of a lattice or network, and the Metropolis algorithm is employed to simulate the system's dynamics and the resulting transport[142]. KMC models have been used successfully to model exciton diffusion, dissociation, and recombination including CT states, and appear to be a flexible option when modeling XSC due to the possibility to couple exciton and carrier dynamics. Current-voltage curves can be obtained using appropriate boundary conditions, and have guided the interpretation of transport data in XSC[143].

Both drift-diffusion and KMC models describe charge carriers as localized wavepackets in a semiclassical picture where the position and momentum of the carriers describe their classical trajectory. However, for distances comparable to the carrier wavelength (1−10 nm) and much smaller than the carrier mean free path this picture breaks down, and quantum mechanical models are necessary to study transport in this regime. One important method employed to model coherent[‡] transport is the *non-equilibrium Green's function* (NEGF) formalism, which in principle can also account for carrier-carrier and carrier-phonon scattering but is more commonly used to model the coherent regime. In its essence, the NEGF aims at computing transmission coefficients of electrons through an open system under study coupled between two semi-infinite contacts/reservoirs with an applied bias, yielding current-voltage curves from *ab initio* atomistic simulations; an excellent review of the method can be found at ref.[144]. NEGF based on atomistic DFT calculations are only able to study transport at the nanometer scale due to high computational cost. At present, there are but a few ways to merge semiclassical dynamics occurring

[†]See www.comsol.com

[‡]In this context, *coherent* means that the electron's wavefunction preserves a precise phase relation with the initial state due to the absence of phase-shifting scattering events.

at the μm length scale typical of the device active layer with accurate atomistic simulations of transport. One possible approach to combine the accuracy of quantum mechanical methods with the achievement of longer length scales involves the use of *ab initio* methods to compute exciton/carrier lifetimes and mean free paths to be employed as parameters in KMC simulations. Several groups are working on similar approaches and we believe these efforts will result in accurate models of transport in XSC across multiple length scales.

Beside modeling excitons and carriers, photon propagation within the active layer is a key ingredient in nanoscale PV. Efforts to maximize sunlight absorption by engineering photon propagation generally fall under the name of *light management* (LM) in PV. Figure 4.1 shows that LM occurs at ultrashort time scales due to the large speed of light, but can encompass all the length scales involved in PV. LM aims at maximizing the number of photons trapped in an active layer of a given thickness, equivalent in classical terms to maximizing the strength of the electric field in the active layer. To this end, one important approach at the nano and mesoscale was introduced by the work in ref.[145] showing that corrugation of the active layer leads to an increase in the absorbance by up to a factor of $4n^2$ (n is the refractive index), the so-called ergodic limit whereby light is maximally trapped[145]. While corrugating the surface of solar cells is not a new idea, innovative nano-texturing methods are being applied resulting in enhanced efficiencies, often at the price of higher manufacturing costs. Another area of recent focus is the use of metallic nanostructures to enhance light scattering or create strong local fields by exciting surface plasmons[146]. In both cases, LM is implemented by introducing nm to μm features in the active layer or at the solar cell surface, and results in increased overall efficiency. Simulation methods available to study the distribution of electric fields within the active layer commonly solve Maxwell's equations in the time domain and employing real-space grids. Among different possible implementation schemes, a popular choice involves finite-difference time-domain (known as FDTD) simulations, as implemented for example in the MEEP code developed by the Joannopoulous group at MIT[147].

An interesting LM aspect has to do with comparing AM1.5G efficiencies with the real performance of solar cells, for example in terms of the yearly generated energy of a PV device installed outdoors. Two solar cells with the same nominal PCE measured in AM1.5G conditions in general perform differently in real conditions. This effect is largely due to different efficiencies when the incident sunlight angle is not normal to the cell as it is in standard AM1.5G tests. Interestingly, nanoscale solar cells commonly yield 20−30 % higher energy generation over a year than Si panels of identical AM1.5G efficiency, largely due to the fact that most nanoscale PV active layers normally possess transport-limited thicknesses not allowing for full above-gap sunlight absorption. This leads to increased sunlight paths within the material for higher incident angles, only partially offset by the lower incoming sunlight when the incident angle is increased. The different dependence of the efficiency on incident angle for conventional solar cells and nanoscale PV suggests that the AM1.5G efficiency is but a standard figure of merit in PV, and that solar panels arrangement with respect to incident sunlight crucially determines PV performance. Hence

another important LM aspect in PV is the study of how to arrange macroscopic solar panels to best couple with the Sun's apparent trajectory at a given location and maximize solar energy collection throughout the year for a solar cell with a given angle-dependent PCE. Optimization in this area entails engineering PV architectures at the macroscopic (meter) length scale, and is an important component to achieve best performance for solar panels of a given efficiency. We have studied this problem in detail using computer simulations employing Maxwell's equations within the simplified formalism of ray optics, and briefly discuss this work in the next section with the hope to provide a broader perspective on modeling PV across length scales.

The computational methods introduced in this section to simulate different length and time scales of exciton, charge, and photon dynamics constitute a framework to study, optimize, and design solar cells (and in particular, XSC) in multiple aspects of practical relevance. This includes the choice of active layer materials and contacts, as well as the optimization of cells thickness and geometry, and the macroscopic module arrangement. A multi-scale simulation scheme seems thus possible, whereby nanoscale and femtosecond processes are computed using *ab initio* atomistic simulations, while mesoscale transport is simulated using semiclassical models with *ab initio*-derived parameters to obtain current-voltage curves (and hence all of the solar cell relevant properties, including the efficiency). Macroscale PV simulations further enable to optimize solar energy collection taking as an input the location and the incident-angle-dependent efficiency of the solar panels under study. The procedure described here involves a sequence of steps in which parameters are extracted from smaller length and time scales and transferred to models designed to study progressively larger time and length scales. The possibility – even just in principle – to pursue a similar approach for PV design constitutes a remarkable achievement of computer simulation in mastering the complexity of real solar energy conversion devices. At present, it is under debate whether multi-scale simulation with parameter transfer across length scales can provide better scientific insight than studying in depth specific aspects of particular PV systems, and similar multi-scale studies are often regarded with skepticism. A significant amount of work will be necessary to seamlessly perform multi-scale simulations in a single framework without suffering from the fragmentation and parameter transfer across several models designed to study processes at different length and time scales. Future work in the field will determine the feasibility of multi-scale approaches as mainstream simulation methods in XSC and PV in general. In the remainder of this chapter, we focus on a case study from our recent work on simulating and optimizing solar energy conversion at the macroscopic length scale.

4.2 Sunlight Management at the Macroscopic Scale: the Case of Three-Dimensional Photovoltaics

We discuss in this section how managing sunlight at the macroscopic scale can lead to the creation of new paradigms for nanoscale solar cells and PV in general. While this topic represents somewhat a discontinuity compared to the research examined in Chapter 3 of this thesis, we believe it is an excellent opportunity to highlight novel design principles arising from simulating PV at different length scales. We open our discussion by noting that some of the most important barriers to widespread adoption of PV technology include large PV system costs (currently 2−5 \$/Watt-peak) of which over 50 % is due to installation costs[148], the limited number of peak insolation hours available in most locations (further reduced by weather), and the requirement of a minimum threshold power density for cheaper thin-film technologies to become feasible for residential or commercial rooftop installations. The main approach applied so far to alleviate these problems has been to search for lower-cost active layers with higher PCE. While PCE improvements are the focus of much research, they can only partially reduce installation costs and cannot change the pattern of solar energy generation, since these aspects are related to the macroscale PV system design. Excitonic and conventional solar cells are normally employed in flat form in rooftop installations and are commonly oriented using simple rules of thumb to optimize solar energy collection. This approach yields far-from-optimal sunlight collection and coupling with the Sun's trajectory, as discussed below. Sun-tracking systems employed in large-scale solar energy generation plants can extend the range of useful peak hours, but add significant costs and are not well suited for residential or commercial installations due to the use of expensive and bulky movable parts. The flat design of PV systems constitutes a radically different solution to macroscale LM compared to the three-dimensional (3D) sunlight collecting structures found in Nature. In our recent work[149,150], we studied the problem of how to best arrange solar panels in three dimensions to make macroscopically three-dimensional PV (3DPV) devices capable of optimizing the energy generated in a given base area (energy density) and in a given volume. 3DPV offers a fundamentally new approach to LM in both conventional and nanoscale PV, which we examine here concisely to close our discussion of multi-scale simulation of PV systems.

In what follows, we formulate, solve computationally and study experimentally the problem of collecting solar energy in three dimensions. We show that absorbers and reflectors can be combined in the absence of sun tracking to build 3DPV structures that can generate measured energy densities (energy per base area, kWh/m^2) higher by a factor of 2−20 than stationary flat PV panels for the structures considered here, compared to an increase by a factor of 1.3−1.8 for a flat panel with dual-axis sun tracking. The increased energy density is countered by a larger solar cell area per generated energy for 3DPV compared to flat panels (by a factor of 1.5−4 in our conditions), but accompanied by a vast range of improvements. 3DPV structures can mitigate some of the variability inherent to solar PV as they provide a more even source of solar

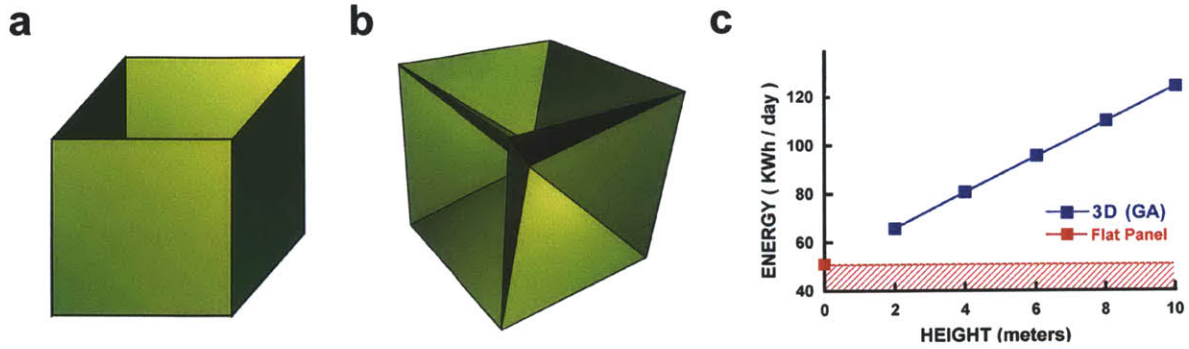

Figure 4.2: **3DPV shapes.** **a,** A cubic 3DPV box open at the top, and **b,** a cubic box with "funnel-shaped" sides. The solar panels composing the structures are shown in green. Both shapes can more than double the daily absorbed sunlight per unit base area compared to a flat panel, for a summer day in the San Francisco bay area. At higher latitudes and during the winter, the daily generated energy density can be as much as five times higher than a flat panel. **c,** Generated energy as a function of height for genetic algorithm (GA) derived shapes. The energy density of a flat panel (with zero height) is shown as a red square. The two shapes in **a** and **b** show a similar linear scaling with height (see ref.[149]).

energy generation at all latitudes: they can double the number of peak power generation hours and dramatically reduce the seasonal, latitude and weather variations of solar energy generation compared to a flat panel design. Furthermore, 3DPV can create new installation paradigms not possible in flat PV.

Two main physical reasons underlying the advantages of collecting sunlight in 3D are the presence of multiple orientations of the absorbers that allow for the effective capture of off-peak sunlight, and the re-absorption of light reflected within the 3D structure. Our first computer simulations on the topic[149] showed that 3DPV structures can increase the generated energy density (energy per footprint area, kWh/m^2) by a factor linear in the structure height, for a given day and location. Optimal shapes derived using a genetic algorithm approach include a cubic box open at the top and a cubic box with funnel-shaped faces, both capable in principle of doubling the daily energy density.

The higher area of PV material per unit of generated energy compared to flat panel designs is a main disadvantage of 3DPV, although this is alleviated by the fact that the module is not the main cost in PV installations at present, and the PV outlay will become increasingly dominated by non-module costs in the near future[148]. Additional practical challenges include inexpensive 3D fabrication routes and optimization of the electronics to avoid power losses. Despite the enormous potential of macroscopic 3DPV structures, the lack of a comprehensive optimization approach and systematic study of the benefits in different seasons, locations and weather conditions, combined with the fact that the module has until only recently dominated the total cost of PV, have thus far limited the advancement of 3DPV as a groundbreaking concept and technology. In our study[150], we establish and implement numerically a general formalism to calculate the energy generated over a period of time, at any location on Earth, by

a 3D assembly of N solar cells of arbitrary shape, orientation, power conversion efficiency (PCE) and optical properties (see Appendix for computational details). The calculations account for inter-cell shading, Air-Mass effects in the incident solar energy and angle-dependent reflection of unpolarized light. The Sun's trajectory is computed for the particular day and location using an algorithm developed by Reda et al.[151] Weather is not explicitly taken into account in the simulations and unless otherwise stated all the simulated energy values in this work assume clear weather. Once the 3DPV structure (for convenience broken down into triangles in our simulations) and the efficiency and reflectivity of the composing panels have been defined, the generated energy can be expressed as an objective function of the cell coordinates and can thus be maximized using standard Monte Carlo (MC) simulated annealing and genetic algorithm (GA) optimization techniques, both implemented in our code[149,150]. The two main forces operating during the maximization of energy generation in 3D are the avoidance of inter-cell shading and the optimization of the re-absorption of light reflected by other cells, with an intricate trade-off (dependent on the Sun's trajectory) typical of complex systems. While here the focus is on electricity generation, the general computational approach we have implemented could allow for the optimization of a wide range of human activities that rely on sunlight collection, including heating, photocatalysis, food crops, wine-making, and sustainable buildings. For now, our work has mainly considered conventional Si solar cells and modeled their angle-dependent PCE based on the different photon flux intercepted as a function of incident angle; nevertheless, we plan to extend our study to include nanoscale PV as well as accurate models of angle-dependent PCE.

In order to study 3DPV systems experimentally, our team has fabricated and tested simple 3DPV structures consisting of a cube open at the top covered by solar cells both on the interior and exterior surfaces (here referred to as an open cube structure), a similar open parallelepiped of the same base area but twice as high, and a tower with ridged faces (Figure 4.3a). The structures are made of, respectively, 9, 17 and 32 commercially available Si solar panels.

Next, we measured the performance of the 3DPV structures. A flat panel was tested indoors under simulated solar light for validation of our simulations at different tilt angles to the light source (Figure 4.3b), while measurements for all 3DPV shapes in Figure 4.3a were collected outdoors under direct sunlight illumination (Figure 4.3c–e). We validated the calculations from our computer code by comparing with experimental results for identical conditions (Figure 4.3b,c and ref.[150]) and found excellent agreement between the two, thus confirming the reliability of our code, further verified through a number of additional tests[150]. The measured performance of a design as simple as the open cube under direct sunlight illumination on a summer day (Jun 16^{th}) shows clearly the benefits of 3DPV compared to the conventional flat design (Figure 4.3c): a daily energy generation of 2.25 Wh (2.27 Wh in the simulation) was measured for the open cube[†] compared to 1.22 Wh (1.01 Wh in the simulation) for a flat solar cell of the same base

[†]The deviation between the experimental and the calculated curve seen during the early morning and late afternoon hours (Figure 4.3c) is likely due to the collection of diffuse light in the experiment. At the solar noon, the simulated power shows a marked dip for the open cube case, also present to a smaller extent in the experiment.

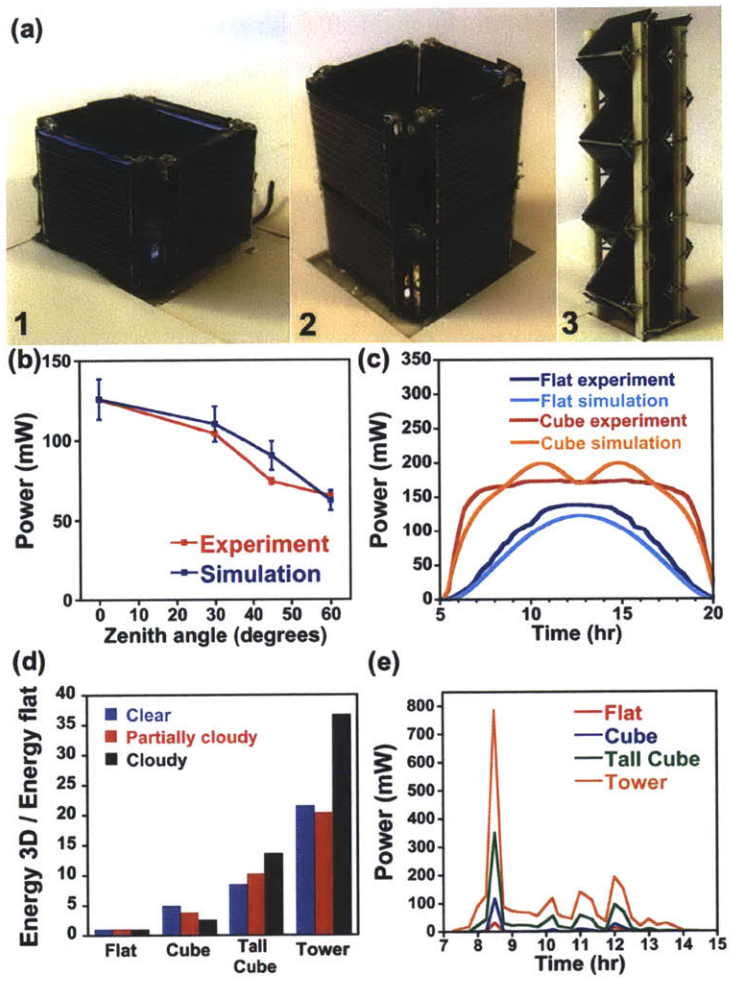

Figure 4.3: 3DPV experiments and simulations. **a,** 3DPV structures made using Si solar cells with area 3×3 cm^2. From left to right, an open cube (1), an open parallelepiped twice as tall (2), and a tower (3). The structures are made up, respectively, of 9, 17, and 32 solar cells. **b,** Power generated by a flat Si panel at various tilt angles measured under simulated solar light illumination, and comparison with computer simulation. The error bars in the simulation results derive from a range in the assumed efficiency of ±1 %. **c,** Both measured and simulated power during a single sunny day for the open cube and for a flat panel of the same base area, showing a maximal range of hours of constant power generation and nearly twice the energy density output for the 3DPV case compared to the flat panel. **d,** Energy generated by the structures shown in **a** under different weather conditions, expressed as a ratio to the energy generated by a flat panel under the same weather conditions. Comparison of the black and blue bars for the case of the parallelepiped and tower shows how structures of higher aspect ratio than the open cube can further outperform a flat panel on a cloudy day compared to a clear day. The parallelepiped in **a** is referred here as "tall cube". **e,** Power generated vs. time for the data of cloudy weather shown in **d**.

area under the same conditions. Such a near doubling in the energy generation resulted from an increase in both the number of hours of peak power generation and the power output throughout the day. The number of hours over which power generation was approximately constant is more than doubled for the 3DPV case compared to the flat panel, and extends between 1 h after sunrise and until 1 h before sunset. We remark that this improvement was achieved by mere macroscale LM in a static structure without solar tracking. Larger gains over a flat panel can be achieved using taller and more complex structures such as the open parallelepiped and ridged tower (Figure 4.3d), with increases during the winter season even further enhanced compared to the summer. For example, the daily energy generation measured in clear weather (Figure 4.3d) for a winter day (Nov. 18^{th}) expressed as a ratio to the energy generated by a flat panel of the same base area tested under the same conditions was 4.88 for the open cube, 8.49 for the parallelepiped and 21.5 for the tower. The excess solar cell area per unit generated energy used for the 3DPV structures compared to the flat panel case was in the range of 1.5–4 for the cases examined here, with a minimum value of 1.5 corresponding to the tower case in the winter and a maximum value of ~4 for the cube in the summer. Taller and more complex structures show an increasingly inhomogeneous cell illumination pattern with a higher number of partially shaded cells, an effect that can introduce power losses and ultimately reduce the overall energy gain. We found that such power losses are mainly determined by the presence of parasitic dark currents in the shaded cells, and we were able to successfully minimize these losses with the addition of blocking diodes in series with each panel in the structure[150].

We used the same outdoor testing apparatus to measure the performance of 3DPV systems under different weather conditions during the same week as the clear weather results in Figure 4.3d. Our data shows that the diffuse light induced by clouds, rain and mist can be captured much more efficiently in 3DPV systems compared to flat panels, leading to increased energy generation enhancement factors for cloudy weather compared to clear weather (Figure 4.3d,e). The relative decrease in generated energy due to clouds is thus less significant for a 3D structure than for a flat panel and hence 3DPV systems are a source of renewable electricity less impacted by weather conditions.

In order to assess the effects of season and latitude on 3DPV performance, we studied the annual energy generation of 3DPV systems – a quantity strongly dependent on the coupling to the Sun's trajectory throughout the year – at different locations on Earth. We performed computer simulations of the energy generated by 3DPV structures over a full year at latitudes between 35° South to 65° North (almost all inhabited land), with an approximate latitude in-

This difference can be attributed to the ideality of the simulated structure, where the infinitesimal cell thickness and the ideal due-South orientation completely cancel the contribution from side cells in the simulation at the solar noon, and also to electrical effects. For these reasons, the very small discrepancy (1 %) found for the energy generated by the cube is a result of error compensation, while a discrepancy between the simulated and experimental energy of the order of 5–15 % is not uncommon even when the key physical effects have been captured in the simulation, as in the flat panel case in Figure 4.3c.

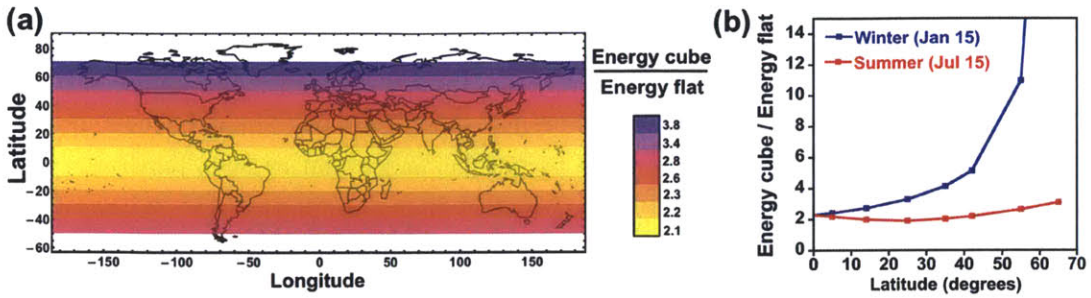

Figure 4.4: 3DPV performance as a function of latitude and season. **a,** Density plot of the variable Y, defined as the ratio of the annual energy density for an open cube 3DPV structure to that of a flat horizontal panel of same base area. Values of Y in the range 2.1−3.8 found here for static 3DPV structures largely exceed those predicted for dual-axis tracking. **b,** Ratio of energy generated by an open cube compared to a flat panel for different seasons. 3DPV outperforms a flat panel by a larger amount during the winter and at higher latitudes due to the increased ability to use sunlight from lower elevation angles in the sky. The winter and summer labels refer to the Northern hemisphere; the curves would look the same for the Southern hemisphere provided the difference in season is taken into account.

crease of 10° between locations and for over 20 cities in the world (see ref.[150] for further details). These results are compared with data for fixed horizontal panels (from our simulations) and for both fixed flat panels with optimal orientation and using dual-axis sun tracking (from the literature, see ref.[152]). Optimal static panel orientation can afford an increase in annual generated energy density (kWh/m^2· year) compared to a flat horizontal panel by a factor of 1.1−1.25. Dual-axis tracking provides at present the best way to dynamically couple a PV panel to the Sun's trajectory, and can yield an increase of annual generated energy by a factor of 1.35−1.8 compared to a flat horizontal panel, at the cost of using expensive movable parts to track the Sun's position[152]. For comparison, we calculated the same ratio (defined as Y here) of annual generated energy density for simple 3DPV structures to that of a flat horizontal panel of same base area, at several different latitudes (Figure 4.4a). Even with a simple open cube structure, a large increase in the annual energy generation compared to a flat horizontal panel is found for 3DPV, with values of Y in the range 2.1−3.8, increasing monotonically from the equator to the poles. This trend compensates the lower ground insolation at larger latitudes to give an overall density of generated energy with significantly lower variation between locations at different latitudes for the 3DPV case compared to a flat panel. When compared to flat panels with optimal orientation (ref.[152], or from our calculations with similar results), an increase in the generated energy density in the range of 1.8−3 is found, thus still superior to the dual-axis tracking case. For latitudes with maximal population density (between 50°N and 25°N) values of Y are in the range of 2.5−3, suggesting that 3DPV structures can be used to increase the energy density (and consequently enable cheaper PV technologies) in geographical areas where future PV installations will abound. The ratio of generated energy from a 3D structure to that of a flat panel increases from summer to winter (Figure 4.4b) by a larger factor at higher lati-

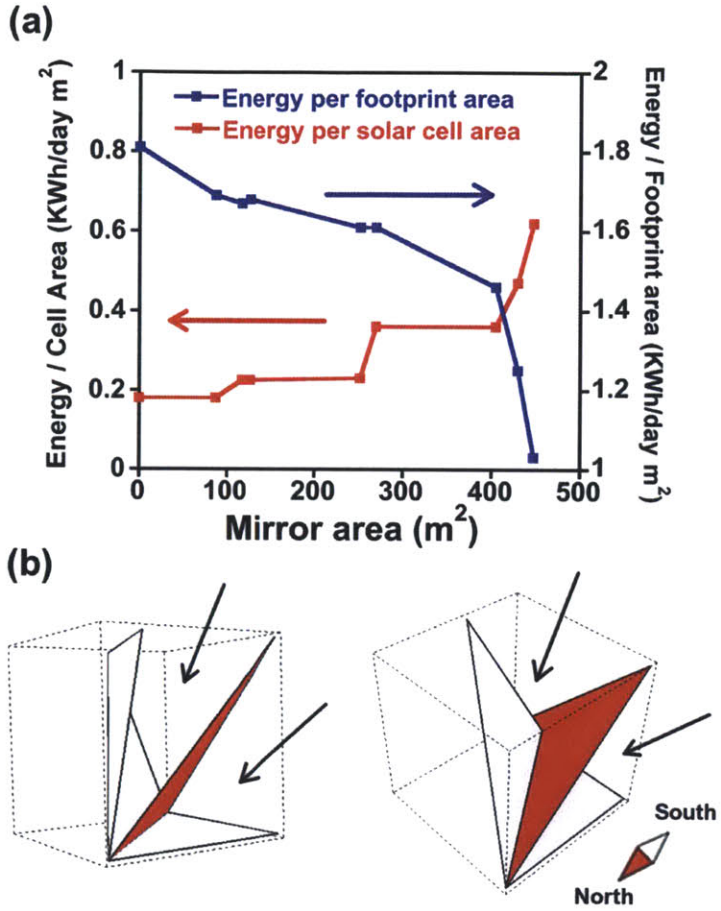

Figure 4.5: **Static 3D solar energy concentration.** **a,** Concentration of light by means of mirrors is quantified by the increase in the energy per unit solar cell area. For 3D solutions provided by the MC algorithm with a 10 m side cubic simulation box, the red curve describes the energy obtained in a day per unit area of solar cells. In the absence of mirrors, 3DPV optimizes the energy/footprint area (blue curve) rather than the energy per solar cell area. The latter can be optimized by sunlight concentration, as seen from the opposite trend of the two curves. A maximal concentration ratio of $\sim$3.5 is inferred by comparing the values at the two ends of the red curve. **b,** Best-concentrating configuration of mirrors (light gray) and solar cells (red) in a 10 m side cubic volume; a simplified structure extracted from the MC optimization is shown here. It consists of a solar panel arranged between two mirrors and resembles a flower open towards the sunlight direction (South in the figure). The black arrows show the direction of incident sunlight.

tudes, implying that 3DPV has lower variation in the energy generation due to season, for the same physical reason leading to reduced latitude variability – namely, a greater ability to collect sunlight when the sun is at low elevation angles compared to a flat panel.

Further possibilities to exploit solar energy generation in 3D include incorporating mirrors together with PV panels within the structure, with the aim of concentrating sunlight without sun-tracking systems, in contrast to existing concentrating technologies. Structures made of a combination of mirrors and solar panels were optimized using a MC simulated annealing optimization scheme. The concentration ratio (a figure of merit) is defined here as a ratio between the energy per unit area of active material generated with and without mirrors. A highest concentration ratio of ~3.5 was obtained for maximal mirror area within a fixed simulation volume (Figure 4.5a). The best concentrating structure consisted of a solar cell cutting the body diagonal of the simulation box and enclosed within two regions of mirrors in an "open flower" configuration facing the Sun (Figure 4.5b). In this high-concentration limit, the use of a given amount of PV material is optimal for the 3DPV case: the energy per unit of PV active material is almost as high as for the flat panel case, yet with an energy generation 25 % higher than the latter. On the other hand, a higher mirror area causes a decrease in the generated energy density, thus defining two opposite limits for volumetric solar energy generation (Figure 4.5a): maximal energy per footprint area (3DPV case) and maximal energy per active material area (flat panel case). This further elucidates the difference between sunlight collection in two and three dimensions, and illustrates the extra design flexibility inherent to the use of 3D structures.

In addition to intriguing fundamental aspects related to LM and macroscale PV simulation, 3D solar collecting structures show tremendous promise for practical applications. Potential 3DPV technologies could include structures that ship flat and expand to fill a volume in an origami-like manner, for ground or flat-roof installation, or chargers for electric-powered vehicles in urban areas, or in sustainable buildings using novel semitransparent flexible PV cells incorporated in walls and windows. Two such cases are examined in detail at ref.[150]: a 3D electric bike charger prototype and a 50 m tall building with the surface completely coated with solar panels. In closing, we observe that a comparative cost analysis between 3DPV and flat panel design is far from simple: apart from the higher number of panels used per unit energy in 3DPV, estimates of the installation costs and solar cell wiring costs are necessary, together with an estimate of the benefits of having a larger number of peak hours during the day. A detailed study should use the concept of levelized cost of energy, although this is beyond the scope of the present work. In summary, the striking range of improvements imparted by three-dimensionality to static solar collecting structures stems from their optimal coupling with the Sun's trajectory. 3DPV structures using simple shapes and electrical connections largely outperform flat panels of the same base area, and show promise for embedding PV systems in the urban environment beyond the flat panel form on rooftops. Computer design facilitates the prediction of generated energy and optimal shapes, and will be an indispensable tool for optimizing solar energy generation at the macroscale, thus complementing the multi-scale picture of PV simulation illustrated here.

4.3 Appendix

Energy calculations. The main routine of our code performs computation of the total energy absorbed during any given period of time and at any given location on Earth by a 3D assembly of panels of given reflectivity and power conversion efficiency. This routine incorporates key differences compared to the one used in our first work at ref.[149]. For example, the use of Air Mass (AM) correction for solar flux allows for simulations during different seasons and at different latitudes, with reliable calculation of power curves and total energy. The computation has been generalized to account for cells of different efficiency and reflectivity within the structure, thus expanding the design opportunities to systems such as solar energy concentrators, where the mirrors are added as cells with zero efficiency and 100 % reflectivity. The code has been extended to incorporate a start and an end date, so that simulations over any interval of time are possible. The Fresnel equations employed now assume unpolarized sunlight. All aspects of the code were carefully tested, and new optimization methods were added to find energy maxima as discussed below. Our algorithm considers a 3D assembly of N panels of arbitrary efficiency and optical properties, where the l^{th} panel has refractive index n_l and conversion efficiency η_l ($l = 1, 2, ..., N$, and $\eta_l = 0$ for mirrors). The energy E (kWh/day) generated in a given day and location can be computed as:

$$E = \sum_{k=1}^{24/\Delta t} P_k \cdot \Delta t$$

where Δt is a time-step (in hours) in the solar trajectory allowing for converged energy, and P_k is the total power generated at the k^{th} solar time-step. The total energy over a period of time is obtained by looping over the days composing the period, and summing the energies generated during each day. The key quantity P_k can be expanded perturbatively:

$$P_k = P_k^{(0)} + P_k^{(1)} + ... + P_k^{(m)} + ...$$

where the m^{th} term accounts for m reflections of a light ray that initially hit the structure – and is thus of order R^m, where R is the average reflectivity of the absorbers – so that for most cases of practical interest, an expansion up to $m = 1$ suffices. Explicitly, $P_k(0)$ and $P_k(1)$ can be written as:

$$P_k^{(0)} = \sum_{l=1}^{N} I_k \cdot \eta_l \cdot A_{l,\text{eff}}[1 - R_l(\theta_{l,k})] \cos(\theta_{l,k}) \tag{4.1}$$

$$P_k^{(1)} = \sum_{l=1}^{N} \{[I_k \cdot \eta_l \cdot A_{l,\text{eff}} R_l(\theta_{l,k}) \cos(\theta_{l,k})] \cdot \eta_s[1 - R_s(\alpha_{ls,k})]\} \tag{4.2}$$

where I_k is the incident energy flux from the Sun at the k^{th} time-step (and includes a correction for Air-Mass effects), $A_{l,\text{eff}}$ is the unshaded area of the l_{th} cell, and $R_l(\theta_{l,k})$ is the reflectivity of the l_{th} cell for an incidence angle (from the local normal) $\theta_{l,k}$ at the k^{th} time-step, that is calculated through the Fresnel equations for unpolarized incident light. In eq. 4.2 the residual power after the absorption of direct sunlight (first square bracket) is transmitted from the l^{th} cell

and redirected with specular reflection to the s^{th} cell that gets first hit by the reflected ray. The s^{th} cell absorbs it according to its efficiency η_s and to its reflectivity calculated using the angle of incidence $\alpha_{ls,k}$ with the reflected ray. In practice, both formulas are computed by setting up a fine converged grid for each cell (normally $g = 10,000$ grid-points) so that all quantities are computed by looping over sub-cells of area equal to A/g (A is the area of a given triangular cell area), which also removes the need to summing s over the subset of cells hit by the reflected light coming out of a given cell. The empirical expression used to calculate the intensity of incident light on the Earth surface I_k (W/m^2) with AM correction for the Sun's position at the k^{th} time-step is:

$$I_k \equiv I(\beta_k) = 1.1 \cdot 1353 \cdot 0.7^{\left[\frac{1}{\cos(\beta_k)}\right]^{0.678}} \tag{4.3}$$

where β_k is the Zenith angle of the sun ray with the Earth's local normal at the k^{th} solar time-step, 1353 W/m^2 is the solar constant, the factor 1.1 takes into account (though in an elementary way) diffuse radiation, and the third factor contains the absorption from the atmosphere and an empirical AM correction. The angle β_k is calculated at each step of the Sun's trajectory for the particular day and location using a solar vector obtained from the solar position algorithm developed by Reda et al.[151] and incorporated into our code. Dispersion effects (dependence of optical properties on radiation wavelength) and weather conditions are not taken into account and are the main approximations of our model. Dispersion effects are fairly difficult to include, and would increase the computation time by a factor of 10−100. Weather effects require reliable weather information (e.g. from satellites), and seem interesting to explore in future work.

Optimization algorithms. Our code uses genetic algorithm (GA)[153] and simulated-annealing Monte Carlo (MC)[154] methods to maximize the energy E generated in a given day in the phase space constituted by the panels' coordinates. The GA algorithm was used as described in ref.[149]. Briefly, candidate 3D structures are combined using operations based on three principles of natural selection (selection, recombination, and mutation). The "tournament without replacement" selection scheme was used, in which s structures from the current population are chosen randomly and the one of highest fitness proceeds to the mating pool, until a desired pool size is reached[153]. In our simulations $s = 2$, and the fitness function corresponds to the energy E produced in one day by the given structure[149]. The recombination step randomly combines 3D structures in the mating pool and with some probability (here 80 %) crosses their triangle coordinates, causing the swapping of whole triangles. A two-point crossover recombination method was employed, wherein two indices are selected at random in the list of coordinates composing the chromosomes, and then the entire string of coordinates in between is traded between the pair of solutions. Finally, the mutation operator slightly perturbs each coordinate, for the purpose of searching more efficiently the coordinates space. These three operations are performed until convergence is reached (usually 10,000−50,000 simulation steps), and a 3DPV structure with maximal energy production is achieved. The number of grid-points per triangular cell was fixed to 100 during most optimizations to limit computation time, and following the optimization

optimal structures were re-examined using 10,000 grid-points as in all other simulations.

The MC algorithm was used to optimize structures of mixed optical properties, where we chose trial moves that preserve the optical properties of the single cells to favor the convergence of the optimization process. Our MC algorithm uses a standard Metropolis scheme[154] for acceptance/rejection of trial moves, and a fictitious temperature T that is decreased during the simulation according to a specified cooling schedule[150]. Trial moves consisted in the change of a randomly chosen set of coordinates of the candidate structure. A number of coordinates varying between 1 and $9N$ (N is the number of triangles) were translated randomly within a cubic box of side $1-100$ % the simulation box side (with periodic boundary conditions), thus determining a change ΔE in the total energy. When $\Delta E > 0$ the move is accepted, whereas when $\Delta E < 0$ the move is accepted with probability $P = \mathrm{e}^{-|\Delta E|/T}$. When a move is accepted, the structure is updated and a new random move is performed. Most MC simulations consisted of 100,000 steps with a converged value of the final energy. The code implements both power law and inverse-log cooling schedules[154]; in most simulations we used the inverse-log cooling schedule. Average ΔE values for the given trial move were determined prior to running the optimization with a short simulation (1,000 steps). Parameters for the cooling schedule were determined by imposing a temperature value such that the initial acceptance rate is $P = 0.99$ and the final acceptance is $P = 10^{-5}$, with a method detailed in ref.[154]. The GA and MC algorithms gave consistent results for optimization of 1, 2, 3, 4, 10, 20, 50 cells in a $10\times10\times10$ m^3 cubic simulation box (not shown here), suggesting that both algorithms are capable of finding energy values near the global maximum using less than 100,000 steps. Since the main cost of the simulation is the energy computation routine, the cost is comparable for both algorithms. For example, a 100,000 steps long simulation with 20 cells is completed in $1-2$ days on a single processor. Parallelization of the code using standard MPI library is in the agenda, and could cut the computation time by a factor linear in the number of processors.

5 Conclusions

Over a century of technological innovation has followed the preparation of the first solid-state solar cell by Charles Fritts, who in 1883 coated selenium with a thin layer of gold to achieve a rudimentary Schottky-barrier solar cell with less than 1 % efficiency. In the modern era of materials design, technological innovation takes advantage of the synergistic role of experiments and computational theory to speed up the development of materials with desired functionality. Computer simulations as applied in this thesis further enable deeper understanding of the energy conversion mechanisms in complex materials and interfaces with atomistic detail.

The approach employed in this thesis combines accurate calculations of specific parts of nanoscale PV systems (in particular, the D-A interface) with experiments capturing the multi-scale complexity of real devices. Our work develops a methodological framework to study D-A interfaces using *ab initio* calculations. We demonstrate that DFT calculations can be employed to compute the valence band offsets at interfaces between nanostructures with similar chemistries, as well as to predict work functions and Schottky barriers at such interfaces. Since these properties are largely determined by the ground-state charge density of the system, DFT can accurately capture qualitative trends in these quantities across different systems, and in some cases predict quantitative values with good accuracy. The GW method can extend the scope of DFT to determine quantitatively accurate band alignments, ionization potentials, and electron affinities, while the BSE method can be employed to compute accurate absorption spectra including excitonic effects of crucial importance in nanoscale PV. Our work thus shows that DFT in combination with the GW-BSE approach enable the determination of the spectroscopic properties of interest in nanoscale PV, such as the D-A interface gap and thus the maximum open-circuit voltage, the absorbance of the active layer and thus the maximum short-circuit current under solar illumination, and the maximum power conversion efficiency for given fill-factor values. Taken together, the computational framework introduced in this thesis constitutes a substantial advancement in the simulation of nanoscale PV systems and the quantitative determination of their efficiency. Extensions to the static picture employed here to determine the D-A interface energetics and infer exciton dissociation include the study of processes occurring across different time and length scales, as described in Chapter 3. We believe that two key areas of future investigation in the field will be the determination of the subpicosecond time domain dynamics following photoexcitation, as well as the study of charge and exciton transport employing quantum and/or semiclassical models suitable for the μm to mm length scale. Advances in these areas constitute an important part of the agenda for the next decade of computer simulation in nanoscale PV.

The methodology described in this thesis is used to study and develop a number of systems of keen scientific and technological interest in nanoscale PV. The key material-related achievement shown in this work is the possibility to prepare excitonic solar cells based on materials alternative to conjugated polymers and small molecules, with enhanced optical absorption, carrier mobility,

and photostability. Our work focuses on the investigation of two new families of materials for nanoscale PV, namely nanocarbon and monolayer materials, displaying a host of novel physical properties. Our initial work on s-SWCNT/polymer solar cells established the role of delocalization in the donor's LUMO state to increase the charge injection rate into the acceptor, as well as the importance of carrier recombination in limiting the performance of polymer based active layers with large s-SWCNT weight fractions. The presence of an open-circuit voltage even at large s-SWCNT content in polymer based solar cells led us to consider solar cells based entirely on carbon. DFT calculations allowed us to find trends in the band offsets for nanotubes of different chirality and diameter interfaced with PCBM fullerene. We established the key role of the diameter of s-SWCNT in determining the band alignment and power conversion efficiency, and identified small-diameter s-SWCNT/PCBM as a suitable D-A interface for efficient solar cells. Our calculations have guided the preparation of carbon based active layers with over 5 % efficiency rivaling quantum dot based and polymer based nanoscale PV. Further work is ongoing on nanocarbon solar cells, especially to understand the role of buffer layers and metallic nanotube impurities.

The possibility to investigate materials defined with atomistic detail using computer simulation further enabled us to compute several spectroscopic properties of amorphous carbon (a-C) as a function of density and hydrogen content. We established the key role of the sp^2/sp^3 ratio in the carbon atom network in determining the optical and electronic properties of a-C. Future work will employ such spectroscopic information for a-C to enable the use of coal as a PV material. Despite the fact that coal samples possess inherent multi-scale complexity due to the presence of multiple phases, we believe that with enough research efforts coal could be engineered for application to PV similar to other materials. Coal based PV has the potential for a paradigm shift in the role of coal from polluting combustible to key material for clean renewable energy.

Our interest to explore PV active layers reaching the ultimate limit for small thickness prompted us to study 1 nm thick solar cells based on two-dimensional monolayer materials. Graphene is the thinnest form of carbon, and is the first discovered member of a large family of monolayers with yet untapped technological potential. The calculations shown in this thesis suggest that solar cells with a thickness of just $\sim$1 nm can be realized using graphene and transition metal dichalcogenide (TMD) monolayers, and can achieve an order of magnitude higher sunlight absorption than GaAs and Si as well as unprecedented generated power densities. We attribute the high optical absorption of monolayer materials to the presence of strong excitonic transitions as well as a continuum of states due to the two-dimensional periodicity. The calculation of TMD monolayers' absorbance with quantitative accuracy shown here involves a high level of sophistication due to the presence of d electrons and strong spin-orbit and excitonic effects, and shows the importance of semi-core states in the calculations of the exchange interaction in TMD and similar compounds. Our calculations further show the possibility to tune the band gap and optical absorption in monolayer materials by lateral confinement of excitons

in two-dimensional domains for the case of hybrid graphene-BN monolayers. Such confinement mechanism in two dimensions is analogous to exciton confinement in nanocrystal quantum dots, and leads to tunable efficiencies as well as a greater flexibility in fabricating nanoscale solar cells. Future work will expand our study to hybrid multilayers combining materials with different optical and electronic properties; these systems are expected to exhibit a range of novel optical effects enabling further control of exciton formation and dissociation in ultrathin solar cells.

This thesis closes with a discussion of multiscale simulation in nanoscale PV, highlighting the complexity of real PV systems as well as the challenges associated with their simulation across length and time scales. We analyze a case study from our work combining classical electromagnetism calculations with optimization algorithms to study optimal sunlight collection at the macroscale. We demonstrate the simulation and fabrication of three-dimensional PV devices with a striking range of benefits for solar energy conversion deriving from the optimal coupling of three-dimensional PV structures to the Sun's trajectory.

In conclusion, the future development of accurate multiscale computer simulations methods together with the availability of ever-improving experimental techniques suggests that the future of nanoscale solar cells is bright and limited only by human ingenuity.

References

[1] Securing Materials for Emerging Technologies (2011). A report by the APS panel on public affairs & the Materials Research Society.
Available on-line at http://www.aps.org/publications/apsnews/201103/energycritical.cfm.

[2] Ginley, D., Green, M. A. & Collins, R. Solar energy conversion towards 1 Terawatt. *MRS Bull.* **33**, 355–364 (2008).

[3] Ginley, D. S. & Cahen, D. *Fundamentals of materials for energy and environmental sustainability* (Cambridge University Press, 2011).

[4] SunShot vision study, Chapter 1 (2012).
See: http://www1.eere.energy.gov/solar/sunshot/vision_study.html.

[5] Li, G., Zhu, R. & Yang, Y. Polymer solar cells. *Nat. Photonics* **6**, 153–161 (2012).

[6] Mishra, A. & Bäuerle, P. Small molecule organic semiconductors on the move: promises for future solar energy technology. *Angew. Chem. Int. Ed.* **51**, 2020–2067 (2012).

[7] Mayer, A. C., Scully, S. R., Hardin, B. E., Rowell, M. W. & McGehee, M. D. Polymer-based solar cells. *Mater. Today* **10**, 28–33 (2007).

[8] Nelson, J. Polymer:fullerene bulk heterojunction solar cells. *Mater. Today* **14**, 462–470 (2011).

[9] Sargent, E. H. Colloidal quantum dot solar cells. *Nat. Photonics* **6**, 133–135 (2012).

[10] Gratzel, M., Janssen, R. J., Mitzi, D. B. & Sargent, E. H. Materials interface engineering for solution-processed photovoltaics. *Nature* **488**, 304–312 (2012).

[11] The NREL efficiency plot can be found at the website: http://www.nrel.gov/ncpv/.

[12] Wurfel, P. *Physics of Solar Cells* (Wiley-VCH, Weinheim, 2009).

[13] Gregg, B. A. The photoconversion mechanism of excitonic solar cells. *MRS Bull.* **30**, 20–22 (2005).

[14] Jailaubekov, A. E. *et al.* Hot charge-transfer excitons set the time limit for charge separation at donor/acceptor interfaces in organic photovoltaics. *Nat. Mater.* **12**, 66–73 (2012).

[15] Grancini, G. *et al.* Hot exciton dissociation in polymer solar cells. *Nat. Mater.* (2012).

[16] Bakulin, A. A. *et al.* The role of driving energy and delocalized states for charge separation in organic semiconductors. *Science* **335**, 1340–1344 (2012).

[17] Lunt, R. R., Osedach, T. P., Brown, P. R., Rowehl, J. A. & Bulović, V. Practical roadmap and limits to nanostructured photovoltaics. *Adv. Mater.* **23**, 5712–5727 (2011).

[18] Riede, M., Mueller, T., Tress, W., Schueppel, R. & Leo, K. Small-molecule solar cells: status and perspectives. *Nanotechnology* **19**, 424001 (2008).

[19] Peters, C. H. *et al.* The mechanism of burn-in loss in a high efficiency polymer solar cell. *Adv. Mater.* **24**, 663–668 (2012).

[20] Grätzel, C. & Zakeeruddin, S. M. Recent trends in mesoscopic solar cells based on molecular and nanopigment light harvesters. *Mater. Today* **16**, 11–18 (2013).

[21] The AM1.5G spectrum was taken from the NREL website: http://rredc.nrel.gov/solar/spectra/am1.5 and integrated with the trapezoid rule.

[22] Shockley, W. & Queisser, H. J. Detailed balance limit of efficiency of p-n junction solar cells. *J. Appl. Phys.* **32**, 510–519 (1961).

[23] Fox, M. *Optical properties of solids* (Oxford University Press, New York, 2001).

[24] Polman, A. & Atwater, H. A. Photonic design principles for ultrahigh-efficiency photovoltaics. *Nat. Mater.* **11**, 174–177 (2012).

[25] Scharber, M. C. *et al.* Design rules for donors in bulk-heterojunction solar cells – towards 10% energy-conversion efficiency. *Adv. Mater.* **18**, 789–794 (2006).

[26] Martin, R. M. *Electronic Structrure: Basic Theory and Practical Methods* (Cambridge University Press, 2008).

[27] Hybertsen, M. S. & Louie, S. G. Electron correlation in semiconductors and insulators: Band gaps and quasiparticle energies. *Phys. Rev. B* **34**, 5390–5413 (1986).

[28] Onida, G., Reining, L. & Rubio, A. Electronic excitations: density-functional versus many-body Green function approaches. *Rev. Mod. Phys.* **74**, 601–659 (2002).

[29] Hohenberg, P. & Kohn, W. Inhomogeneous electron gas. *Physical Review* **136**, B864 (1964).

[30] Kronik, L., Stein, T., Refaely-Abramson, S. & Baer, R. Excitation gaps of finite-sized systems from optimally tuned range-separated hybrid functionals. *J. Chem. Theory Comput.* **8**, 1515–1531 (2012).

[31] Giantomassi, M. *et al.* Electronic properties of interfaces and defects from many-body perturbation theory: Recent developments and applications. *Phys. Status Solidi B* **248**, 275 (2011).

[32] Wu, Z., Kanai, Y. & Grossman, J. C. Quantum monte carlo calculations of the energy-level alignment at hybrid interfaces: Role of many-body effects. *Phys. Rev. B* **79**, 201309 (2009).

[33] Noffsinger, J., Kioupakis, E., Van de Walle, C. G., Louie, S. G. & Cohen, M. L. Phonon-assisted optical absorption in silicon from first principles. *Phys. Rev. Lett.* **108**, 167402 (2012).

[34] Aulbur, W. G., Jonsson, L. & Wilkins, J. W. Quasiparticle calculations in solids-III. GWA calculations: Numerical considerations. *Solid State Physics-Advances in Research and Applications* **2000**, 89–132 (1999).

[35] Giannozzi, P. *et al. et al.* QUANTUM ESPRESSO: a modular and open-source software project for quantum simulations of materials. *J. Phys.: Condens. Matter* **21**, 395502 (19pp) (2009). URL `http://www.quantum-espresso.org`.

[36] Kresse, G. & Furthmüller, J. Efficient iterative schemes for *ab initio* total-energy calculations using a plane-wave basis set. *Phys. Rev. B* **54**, 11169 (1996).

[37] Marini, A., Hogan, C., Gruning, M. & Varsano, D. Yambo: an *Ab Initio* tool for excited state calculation. *Comp. Phys. Comm.* **180**, 1392–1403 (2009).

[38] Shishkin, M. & Kresse, G. Implementation and performance of the frequency-dependent GW method within the PAW framework. *Phys. Rev. B* **74**, 035101 (2006).

[39] Bernardi, M. & Grossman, J. C. Error analysis for large-scale searches of efficient materials for nanoscale photovoltaics. *Submitted for Publication* (2013).

[40] Hachmann, J. *et al.* The harvard clean energy project: Large-scale computational screening and design of organic photovoltaics on the world community grid. *J. Phys. Chem. Lett.* **2**, 2241–2251 (2011).

[41] Kymakis, E. & Amaratunga, G. Single-wall carbon nanotube/conjugated polymer photovoltaic devices. *Appl. Phys. Lett.* **80**, 112–114 (2002).

[42] Holt, J. M. *et al.* Prolonging charge separation in P3HT:SWNT composites using highly enriched semiconducting nanotubes. *Nano Lett.* **10**, 4627–4633 (2010).

[43] Kanai, Y. & Grossman, J. C. Role of semiconducting and metallic tubes in P3HT/carbon-nanotube photovoltaic heterojunctions: Density functional theory calculations. *Nano Lett.* **8**, 908–912 (2008).

[44] Bindl, D. J., Safron, N. S. & Arnold, M. S. Dissociating excitons photogenerated in semiconducting carbon nanotubes at polymeric photovoltaic heterojunction interfaces. *ACS Nano* **4**, 5657–5664 (2010).

[45] Bernardi, M., Giulianini, M. & Grossman, J. C. Self-assembly and its impact on interfacial charge transfer in carbon nanotube/P3HT solar cells. *ACS Nano* **4**, 6599 (2010).

[46] Yang, C., Hu, J. G. & Heeger, A. J. Molecular structure and dynamics at the interfaces within bulk heterojunction materials for solar cells. *J. Am. Chem. Soc.* **128**, 12007–12013 (2006).

[47] Frenkel, D. & Smit, B. *Understanding molecular simulation: from algorithms to applications* (Academic press, 2001).

[48] Plimpton, S. *et al.* Fast parallel algorithms for short-range molecular dynamics. *J. Comp. Phys.* **117**, 1–19 (1995). URL `http://lammps.sandia.gov`.

[49] Giulianini, M. *et al.* Regioregular poly(3-hexyl-thiophene) helical self-organization on carbon nanotubes. *Appl. Phys. Lett.* **95**, 013304–013304 (2009).

[50] Giulianini, M. *et al.* Evidence of multiwall carbon nanotube deformation caused by poly(3-hexylthiophene) adhesion. *J. Phys. Chem. C* **115**, 6324–6330 (2011).

[51] Brown, P. J. *et al.* Effect of interchain interactions on the absorption and emission of poly (3-hexylthiophene). *Phys. Rev. B* **67**, 064203 (2003).

[52] Ren, S. *et al.* Toward efficient carbon nanotube/P3HT solar cells: active layer morphology, electrical, and optical properties. *Nano Lett.* **11**, 5316–5321 (2011).

[53] Kataura, H. *et al.* Optical properties of single-wall carbon nanotubes. *Synth. Met.* **103**, 2555–2558 (1999).

[54] Zhu, H., Wei, J., Wang, K. & Wu, D. Applications of carbon materials in photovoltaic solar cells. *Sol. Energy Mater. Sol. Cells* **93**, 1461–1470 (2009).

[55] Cox, P. A. *The elements. Their origin, abundance, and distribution.* (Oxford University Press, 1989).

[56] Avouris, P. & Martel, R. Progress in carbon nanotube electronics and photonics. *MRS Bull.* **35**, 306–313 (2010).

[57] Bernardi, M. *et al.* Nanocarbon–based photovoltaics. *ACS Nano* **6**, 8896–8903 (2012).

[58] Bindl, D. J., Wu, M.-Y., Prehn, F. C. & Arnold, M. S. Efficiently harvesting excitons from electronic type-controlled semiconducting carbon nanotube films. *Nano Lett.* **11**, 455–460 (2010).

[59] Perdew, J., Burke, K. & Ernzerhof, M. Generalized gradient approximation made simple. *Phys. Rev. Lett.* **77**, 3865 (1996).

[60] Vanderbilt, D. Soft self-consistent pseudopotentials in a generalized eigenvalue formalism. *Phys. Rev. B* **41**, 7892 (1990).

[61] Loh, K. P., Bao, Q., Eda, G. & Chhowalla, M. Graphene oxide as a chemically tunable platform for optical applications. *Nat. Chem.* **2**, 1015–1024 (2010).

[62] Reese, M. O. *et al.* Photoinduced degradation of polymer and polymer–fullerene active layers: experiment and theory. *Adv. Funct. Mater.* **20**, 3476–3483 (2010).

[63] Kumar, P. V., Bernardi, M. & Grossman, J. C. The impact of functionalization on the stability, work function, and photoluminescence of reduced graphene oxide. *ACS Nano* **7**, 1638–1645 (2013).

[64] Xie, Y. *et al.* Air-stable 5% efficient nanocarbon-based solar cells with tunable morphology and infrared absorption. *In preparation* (2013).

[65] Jain, R. M. *et al.* Polymer-free near-infrared photovoltaics with single chirality (6,5) semiconducting carbon nanotube active layers. *Adv. Mater.* **24**, 4436–4439 (2012).

[66] Tung, V. C. *et al.* Surfactant-free water-processable photoconductive all-carbon composite. *J. Am. Chem. Soc.* **133**, 4940–4947 (2011).

[67] Tung, V. C. *et al.* Towards solution processed all-carbon solar cells: A perspective. *Energy Environ. Sci.* **5**, 7810–7818 (2012).

[68] Ramuz, M. P. *et al.* Evaluation of solution-processable carbon-based electrodes for all-carbon solar cells. *ACS Nano* **6**, 10384–10395 (2012).

[69] Street, R. A. *Technology and Applications of Amorphous Silicon* (Springer, 2000).

[70] Fanchini, G., Ray, S. C. & Tagliaferro, A. Optical properties of disordered carbon-based materials. *Surface and Coatings Technology* **151-152**, 233–241 (2002).

[71] Demichelis, F. *et al.* Mechanical and thermophysical properties of diamond-like carbon (dlc) films with different sp^3/sp^2 ratios. *Diam. Relat. Mater.* **2**, 890–892 (1993).

[72] Han, J. *et al.* Photovoltaic characteristics of amorphous silicon solar cells using boron doped tetrahedral amorphous carbon films as p-type window materials. *Appl. Phys. Lett.* **90**, 083508–083508 (2007).

[73] Yu, H., Kaneko, Y., Yoshimura, S. & Otani, S. Photovoltaic cell of carbonaceous film/n-type silicon. *Appl. Phys. Lett.* **68**, 547–549 (1996).

[74] Zhoua, Z. *et al.* Schottky solar cells with amorphous carbon nitride thin films prepared by ion beam sputtering. *Sol. Energ. Mat. Sol. C.* **70**, 487–493 (2002).

[75] Galli, G., Martin, R., Car, R. & Parrinello, M. Structural and electronic properties of amorphous carbon. *Phys. Rev. Lett.* **62**, 555–558 (1989).

[76] Marks, N. A., McKenzie, D. R., Pailthorpe, B. A., Bernasconi, M. & Parrinello, M. Microscopic structure of tetrahedral amorphous carbon. *Phys. Rev. Lett.* **76**, 768–771 (1996).

[77] Tritsaris, G., Mathioudakis, C., Kelires, P. & Kaxiras, E. Optical and elastic properties of diamond-like carbon with metallic inclusions: A theoretical study. *J. Appl. Phys.* **112**, 103503 (2012).

[78] Kresse, G. & Joubert, D. From ultrasoft pseudopotentials to the projector augmented-wave method. *Phys. Rev. B* **59**, 1758 (1999).

[79] Wooten, F., Winer, K. & Weaire, D. Computer generation of structural models of amorphous si and ge. *Phys. Rev. Lett.* **54**, 1392–1395 (1985).

[80] Risplendi, F., Bernardi, M., Cicero, G. & Grossman, J. C. Structure-property relations in amorphous carbon for thin-film photovoltaics. *In preparation* (2013).

[81] Tauc, J., Grigorovici, R. & Vancu, A. Optical properties and electronic structure of amorphous germanium. *Phys. Status Solidi B* **15**, 627–637 (1966).

[82] Powell, C. A. & Morreale, B. D. Materials challenges in advanced coal conversion technologies. *MRS Bull.* **33**, 309–315 (2008).

[83] Novoselov, K. *et al.* Electric field effect in atomically thin carbon films. *Science* **306**, 666–669 (2004).

[84] Kim, K. K. *et al.* Synthesis of monolayer hexagonal boron nitride on Cu foil using chemical vapor deposition. *Nano Lett.* **12**, 161–166 (2012).

[85] Ci, L. *et al.* Atomic layers of hybridized boron nitride and graphene domains. *Nat. Mater.* **9**, 430–435 (2010).

[86] Radisavljevic, B., Radenovic, A., Brivio, J., Giacometti, V. & Kis, A. Single-layer MoS_2 transistors. *Nat. Nanotech.* **6**, 147–150 (2011).

[87] Lee, Y.-H. *et al.* Synthesis of large-area MoS_2 atomic layers with chemical vapor deposition. *Adv. Mater.* **24**, 2320–2325 (2012).

[88] Tongay, S. *et al.* Thermally driven crossover from indirect toward direct bandgap in 2D semiconductors: $MoSe_2$ versus MoS_2. *Nano Lett.* **12**, 5576–5580 (2012).

[89] Gutierrez, H. R. *et al.* Extraordinary room-temperature photoluminescence in WS_2 triangular monolayers. *Nano Lett.* (2012). DOI: 10.1021/nl3026357.

[90] Coleman, J. N. *et al.* Two-dimensional nanosheets produced by liquid exfoliation of layered materials. *Science* **331**, 568–571 (2011).

[91] Geim, A. K. Graphene: Status and prospects. *Science* **324**, 1530–1534 (2009).

[92] Seol, G. & Guo, J. Bandgap opening in boron nitride confined armchair graphene nanoribbon. *Appl. Phys. Lett.* **98**, 143107–143107 (2011).

[93] Lam, K.-T., Lu, Y., Feng, Y. P. & Liang, G. Stability and electronic structure of two dimensional C_xBN_y compound. *Appl. Phys. Lett.* **98**, 022101–022101 (2011).

[94] Manna, A. K. & Pati, S. K. Tunable electronic and magnetic properties in $B_xN_yC_z$ nanohybrids: Effect of domain segregation. *J. Phys. Chem. C* **115**, 10842–10850 (2011).

[95] Li, J. & Shenoy, V. B. Graphene quantum dots embedded in hexagonal boron nitride sheets. *Appl. Phys. Lett.* **98**, 013105–013105 (2011).

[96] Liu, A. Y., Wentzcovitch, R. M. & Cohen, M. L. Atomic arrangement and electronic structure of BC_2N. *Phys. Rev. B* **39**, 1760 (1989).

[97] da Rocha Martins, J. & Chacham, H. Disorder and segregation in B-C-N graphene-type layers and nanotubes: Tuning the band gap. *ACS Nano* **5**, 385–393 (2010).

[98] Blase, X., Charlier, J.-C., De Vita, A. & Car, R. Structural and electronic properties of composite $B_xC_yN_z$ nanotubes and heterojunctions. *Appl. Phys. A* **68**, 293–300 (1999).

[99] Bernardi, M., Palummo, M. & Grossman, J. C. Optoelectronic properties in monolayers of hybridized graphene and hexagonal boron nitride. *Phys. Rev. Lett.* **108**, 226805 (2012).

[100] Jaros, M. Electronic properties of semiconductor alloy systems. *Rep. Prog. Phys.* **48**, 1091 (1985).

[101] Monkhorst, H. J. & Pack, J. D. Special points for Brillouin-zone integrations. *Phys. Rev. B* **13**, 5188–5192 (1976).

[102] Zhu, X. & Su, H. Excitons of edge and surface functionalized graphene nanoribbons. *J. Phys. Chem. C* **114**, 17257–17262 (2010).

[103] Bernardi, M., Palummo, M. & Grossman, J. C. Semiconducting monolayer materials as a tunable platform for excitonic solar cells. *ACS Nano* **6**, 10082–10089 (2012).

[104] Sutter, P. Growth and characterization of graphene-boron nitride heterostructures. March meeting of the American Physical Society of 2012. Abstract available at http://meetings.aps.org/link/BAPS.2012.MAR.X12.5.

[105] Levendorf, M. P. *et al.* Graphene and boron nitride lateral heterostructures for atomically thin circuitry. *Nature* **488**, 627–632 (2012).

[106] Ross, R. T. & Nozik, A. J. Efficiency of hot-carrier solar energy converters. *J. Appl. Phys.* **53**, 3813–3818 (1982).

[107] Castro Neto, A. H., Guinea, F., Peres, N. M. R., Novoselov, K. S. & Geim, A. K. The electronic properties of graphene. *Rev. Mod. Phys.* **81**, 109–162 (2009).

[108] Novoselov, K. S. *et al.* Two-dimensional atomic crystals. *Proc. Natl. Acad. Sci. USA* **102**, 10451–10453 (2005).

[109] Wang, H. *et al.* Integrated circuits based on bilayer MoS_2 transistors. *Nano Lett.* **81**, 109–162 (2012).

[110] Nair, R. R. *et al.* Fine structure constant defines visual transparency of graphene. *Science* **320**, 1308 (2008).

[111] Palik, E. D. *Handbook of Optical Constants of Solids*, vol. 3 (Academic press, 1998).

[112] Ataca, C., Sahin, H. & Ciraci, S. Stable, single-layer MX_2 transition-metal oxides and dichalcogenides in a honeycomb-like structure. *J. Phys. Chem. C* **116**, 8983–8999 (2012).

[113] Smil, V. *Energy* (Oneworld, 2001).

[114] Li, C. H., Mak, K. F., Shan, J., Shan, J. & Heinz, T. Atomically thin MoS_2: A new direct-gap semiconductor. *Phys. Rev. Lett.* **105**, 136805 (2010).

[115] Splendiani, A. *et al.* Emerging photoluminescence in monolayer MoS_2. *Nano Lett.* **10**, 1271–1275 (2010).

[116] Bernardi, M., Palummo, M. & Grossman, J. C. Angstrom-thick solar cells using two-dimensional monolayer materials. *Submitted for Publication* (2013).

[117] Ramasubramaniam, A. Large excitonic effects in monolayers of molybdenum and tungsten dichalcogenides. *Phys. Rev. B* **86**, 115409 (2012).

[118] Miao, X. *et al.* High efficiency graphene solar cells by chemical doping. *Nano Lett.* **12**, 2745–2750 (2012).

[119] Shan, B. & Cho, K. *Ab initio* study of schottky barriers at metal-nanotube contacts. *Phys. Rev. B* **70**, 233405 (2004).

[120] Zhang, W. *et al.* Ultrahigh-gain phototransistors based on graphene-MoS_2 heterostructures. *ArXiv e-prints* (2013). `arXiv:1302.1230`.

[121] Dolui, K., Rungger, I. & Sanvito, S. Origin of the n-type and p-type conductivity of MoS_2 monolayers on a SiO_2 substrate. *ArXiv e-prints* (2013). `arXiv:1301.2491`.

[122] Ma, Y., Dai, Y., Guo, M., Niu, C. & Huang, B. Graphene adhesion on MoS_2 monolayer: An *ab initio* study. *Nanoscale* **3**, 3883–3887 (2011).

[123] Miller, O. D., Yablonovitch, E. & Kurtz, S. R. Intense internal and external fluorescence as solar cells approach the Shockley-Queisser efficiency limit. *ArXiv e-prints* (2011). `arXiv:1106.1603`.

[124] See http://www.appliednanotech.net/news/130103_Solexel_Achievement.php.

[125] Coehoorn, R., Haas, C. & De Groot, R. Electronic structure of $MoSe_2$, MoS_2, and WSe_2. II. The nature of the optical band gaps. *Phys. Rev. B* **35**, 6203 (1987).

[126] Jaramillo, T. F. *et al.* Identification of active edge sites for electrochemical H_2 evolution from MoS_2 nanocatalysts. *Science* **317**, 100–102 (2007).

[127] Kibsgaard, J., Chen, Z., Reinecke, B. N. & Jaramillo, T. F. Engineering the surface structure of MoS_2 to preferentially expose active edge sites for electrocatalysis. *Nat. Mater.* **11**, 963–969 (2012).

[128] Ramasubramaniam, A., Naveh, D. & Towe, E. Tunable band gaps in bilayer transition-metal dichalcogenides. *Phys. Rev. B* **84**, 205325 (2011).

[129] Ataca, C., Topsakal, M., Akturk, E. & Ciraci, S. A comparative study of lattice dynamics of three- and two-dimensional MoS_2. *J. Phys. Chem. C* **115**, 16354–16361 (2011).

[130] Grimme, S. Semiempirical GGA-type density functional constructed with a long-range dispersion correction. *J. Comp. Chem.* **27**, 1787–1799 (2006).

[131] Kośmider, K. & Fernández-Rossier, J. Electronic properties of the MoS_2-WS_2 heterojunction. *ArXiv e-prints* (2012). `arXiv:1212.0111`.

[132] Cheiwchanchamnangij, T. & Lambrecht, W. R. L. Quasiparticle band structure calculation of monolayer, bilayer, and bulk MoS_2. *Phys. Rev. B* **85**, 205302 (2012).

[133] Li, T. & Galli, G. Electronic properties of MoS_2 nanoparticles. *J. Phys. Chem. C* **111**, 16192–16196 (2007).

[134] Blöchl, P. E. Projector augmented-wave method. *Phys. Rev. B* **50**, 17953 (1994).

[135] Yang, L., Deslippe, J., Park, C.-H., Cohen, M. L. & Louie, S. G. Excitonic effects on the optical response of graphene and bilayer graphene. *Phys. Rev. Lett.* **103**, 186802 (2009).

[136] Wang, F., Dukovic, G., Brus, L. E. & Heinz, T. F. Time-resolved fluorescence of carbon nanotubes and its implication for radiative lifetimes. *Phys. Rev. Lett.* **92**, 177401 (2004).

[137] Moreels, I. *et al.* Size-dependent optical properties of colloidal PbS quantum dots. *ACS Nano* **3**, 3023–3030 (2009).

[138] Cabanillas-Gonzalez, J., Grancini, G. & Lanzani, G. Pump-probe spectroscopy in organic semiconductors: Monitoring fundamental processes of relevance in optoelectronics. *Adv. Mater.* **23**, 5468–5485 (2011).

[139] Meng, S. & Kaxiras, E. Electron and hole dynamics in dye-sensitized solar cells: Influencing factors and systematic trends. *Nano Lett.* **10**, 1238–1247 (2010).

[140] Garcia-Belmonte, G., Boix, P. P., Bisquert, J., Sessolo, M. & Bolink, H. J. Simultaneous determination of carrier lifetime and electron density of states in P3HT:PCBM organic solar cells under illumination by impedance spectroscopy. *Sol. En. Mat. Sol. Cells* **94**, 366–375 (2010).

[141] Selberherr, S. *Analysis and Simulation of Semiconductor Devices.* (Springer-Verlag, Wien, 1984).

[142] Voter, A. F. Introduction to the kinetic monte carlo method. In *Radiation Effects in Solids*, 1–23 (Springer, 2007).

[143] Frost, J. M., Cheynis, F., Tuladhar, S. M. & Nelson, J. Influence of polymer-blend morphology on charge transport and photocurrent generation in donor-acceptor polymer blends. *Nano Lett.* **6**, 1674–1681 (2006).

[144] Datta, S. *Electronic transport in mesoscopic systems* (Cambridge university press, 1997).

[145] Yablonovitch, E. & Cody, G. Intensity enhancement in textured optical sheets for solar cells. *Electron Devices, IEEE Transactions on* **29**, 300–305 (1982).

[146] Atwater, H. A. & Polman, A. Plasmonics for improved photovoltaic devices. *Nat. Mater.* **9**, 205–213 (2010).

[147] Oskooi, A. F. *et al.* MEEP: A flexible free-software package for electromagnetic simulations by the FDTD method. *Comp. Phys. Comm.* **181**, 687–702 (2010).

[148] Barbose, G., Darghouth, N. & Wiser, R. (2010). Report LBNL-4121E. See http://eetd.lbl.gov/ea/emp/re-pubs.html.

[149] Myers, B., Bernardi, M. & Grossman, J. C. Three-dimensional photovoltaics. *Appl. Phys. Lett.* **96**, 071902–071902 (2010).

[150] Bernardi, M., Ferralis, N., Wan, J. H., Villalon, R. & Grossman, J. C. Solar energy generation in three dimensions. *Energy Environ. Sci.* **5**, 6880–6884 (2012).

[151] Reda, I. & Andreas, A. Solar position algorithm for solar radiation applications. *Sol. Energy* **76**, 577–589 (2004).

[152] Lave, M. & Kleissl, J. Optimum fixed orientations and benefits of tracking for capturing solar radiation in the continental united states. *Renew. Energ.* **36**, 1145–1152 (2011).

[153] Melanie, M. *An introduction to genetic algorithms* (MIT Press, Boston, USA., 1998).

[154] Shonkwiler, R. W. & Mendivil, F. *Explorations in Monte Carlo Methods* (Springer Verlag, 2009).